

# **Development and Validation of Numerical Methods for Predicting Gyro-TWA Performance**

Jamie Thomson  
(MSci University of Strathclyde)

Department of Physics and Applied Physics  
University of Strathclyde

Thesis Submitted for the Degree of Ph.D.  
September 2006

This thesis is the result of the author's original research. It has been composed by the author and has not been previously submitted for examination which has led to the award of a degree.

The copyright of this thesis belongs to the author under the terms of the United Kingdom Copyright Acts as qualified by University of Strathclyde Regulation 3.50. Due acknowledgement must always be made of the use of any material contained in, or derived from, this thesis.

Signed:

Date:

I would like to dedicate this work to my partner Louise

# Contents

Acknowledgements.....	VIII
Abstract.....	IX
<b>Chapter 1. Introduction.....</b>	<b>10</b>
1.1 History of the Electron Cyclotron Maser (ECM) Instability .....	11
1.2 Development of Gyro-Devices .....	13
1.3 Gyro-Oscillators.....	14
1.4 Amplifiers .....	15
1.4.1 Resonant Amplifiers.....	15
1.4.2 Non-resonant Amplifiers.....	15
1.5 The Gyro-TWA.....	16
1.6 New Work .....	16
<b>Chapter 2. Theory .....</b>	<b>18</b>
2.1 Electromagnetic Theory .....	19
2.1.1 Maxwells Equations.....	19
2.1.2 Electromagnetic Wave Propagation in Free Space .....	20
2.1.3 Plane Waves .....	22
2.1.4 Polarization .....	23
2.1.5 Poynting Vector .....	25
2.1.6 Wave Impedance.....	25
2.1.7 The Skin Effect .....	26
2.1.8 Waveguide Theory.....	27
2.1.9 Reasons for Using Coaxial Lines & Waveguides.....	27
2.1.10 Waveguide Operation.....	29
2.2 Waveguide Theory.....	31
2.2.1 Constraining of an Electromagnetic Wave in a Tube-Like Structure.....	31
2.2.2 Guide Wavelength.....	32

2.2.3 Relationship Between Guide Wavelength and Free Space Wavelength...	33
2.2.4 Boundary Conditions .....	35
2.2.5 Classification of Modes .....	37
2.2.6 Rectangular Waveguides and the Dominant TE Mode.....	37
2.2.7 Transverse Electric Modes.....	40
2.2.8 Transverse Magnetic Modes .....	42
2.2.9 Transverse electric and Magnetic Modes.....	42
2.3 Circular Waveguides.....	43
2.3.1 Introduction.....	43
2.3.2 Circular Waveguide Theory.....	43
2.3.3 TE Modes in Circular Waveguide.....	46
2.3.4 TM Modes in Circular Waveguide .....	47
2.3.5 Circular Waveguide Notation .....	50
<b>Chapter 3. Gyro-Device Theory.....</b>	<b>51</b>
Introduction.....	52
3.1 Physical Principles of the Gyro-TWA.....	54
3.2 Estimated Operating Efficiency of Gyro-TWA.....	55
3.2.1 Saturation due to Free Energy Depletion.....	55
3.2.2 Saturation due to Phase Trapping.....	56
3.2.3 Factors Influencing Practical Efficiency.....	57
3.3 Ideal Dispersion Characteristics for the Gyro-TWA.....	58
3.4 Theory of the Helically Corrugated Waveguide - An Overview.....	59
3.5 General Electron Beam Theory.....	60
3.5.1 Introduction.....	60
3.5.2 Beam Geometries.....	60
3.5.2.1 Axis Encircling ‘Pencil’ Beam.....	60
3.5.2.2 Non-Axis Encircling Thin Annulus Beam.....	60
3.5.2.3 Axis Encircling Annular Beam.....	61
3.5.2.4 Operating Regime.....	62

<b>Chapter 4. Methods and Apparatus</b> .....	63
4.1 Introduction.....	64
4.2 Perturbation Theory.....	64
4.3 Linear Theory.....	67
4.4 Overview of MAGIC PIC code.....	70
4.5 MAGIC Simulation for Determining Dispersion of Helix.....	70
4.6 MAGIC Simulation for Modelling of Gyro-TWA.....	72
4.7 Design of the Helically Corrugated Waveguide for use in the Gyro-TWA.....	76
4.8 Experimental Apparatus.....	78
4.8.1 Elliptical Convertors.....	80
4.8.2 Vector Network Analyser.....	81
4.8.3 Method for Analysis of Helically Corrugated Waveguide Dispersion.....	82
4.8.4 Summary of Design Software.....	85
<b>Chapter 5. Results</b> .....	88
5.1 Introduction.....	89
5.2 Measurement of Helically Corrugated Waveguide.....	89
5.3 Numerical Models.....	90
5.3.1 Modelling of Helically Corrugated Waveguide.....	90
5.3.2 Perturbation Theory.....	90
5.3.3 MAGIC Simulation of the Helical Waveguide.....	92
5.3.4 MAGIC Simulation of the Amplifier.....	100
5.3.5 Comments on the Output of the Code.....	111
5.4 Modelling of Linear Gain.....	111
5.4.1 Results.....	111
<b>Chapter 6. Comparison of Results</b> .....	115
6.1 Waveguide Dispersion Theory.....	116
6.1.1 Modelling.....	116
6.1.2 Measurement.....	116
6.2 Measurement of Microwave Output from Amplifier.....	117
6.2.1 Gain.....	118

6.2.2 Efficiency.....	120
6.3 Gain, Efficiency and Bandwidth Results Compared.....	121
6.4 Frequency Measurements.....	125
<b>Chapter 7. Conclusions and Future Work.....</b>	<b>126</b>
7.1 Introduction.....	127
7.2 Conclusions.....	127
7.2.1 Approximate prediction of dispersion by perturbation theory.....	128
7.2.2 MAGIC code for prediction of dispersion.....	128
7.2.3 MAGIC code for simulation of electron beam.....	129
7.2.4 MAPLE code for prediction of linear gain behaviour.....	129
7.2.5 MAGIC code for gyro-TWA simulation.....	130
7.2.6 Measurement of dispersion characteristics using VNA method.....	131
7.3 Discussion on Application of New Code.....	131
7.4 Future Work.....	133
7.5 Summary.....	133
<b>Appendix A - Computer Codes (MAGIC).....</b>	<b>135</b>
<b>Appendix B - MAPLE Script for Linear Gain Prediction.....</b>	<b>157</b>
<b>References.....</b>	<b>164</b>

## **Acknowledgements**

I would like to thank my supervisors Professor A.D.R Phelps and Dr Kevin Ronald for their guidance and assistance during this work.

I would also like to thank TMD Technologies Limited and PPARC for providing personal funding by way of a PPARC/CASE studentship.

The author is also indebted to Strathclydes skilled technicians and in particular technician Mr I Dunwoodie for his assistance throughout this work.

Also, I would like to thank my colleagues Dr. A.W. Cross, Dr. A. R. Young, Dr W. He, Dr C. Whyte, Dr G. Burt and Mr Euan Rafferty for their support and help along the way. Finally, I would like to thank my parents Samuel and Rosemary and my partner Louise who have supported and encouraged the completion of this work.



## Abstract

A novel experimental method has been devised to measure the dispersion of a waveguide having a helical corrugation on the outer wall. This waveguide type has been used to synthesise eigenmodes with useful and complex dispersive behaviour. Two techniques exist to predict the dispersion, but both are approximations. Hitherto experimental confirmation depended entirely on a scalar polarisation measurement which required the fabrication of a  $\sim 1\text{m}$  (many tens of periods) of waveguide to yield good results. The new technique based around a vector network analyser can measure the dispersion with reduced systematic uncertainty on a section no more than a few periods length. The new method facilitates the corroboration of the predicted dispersion prior to expensive large-scale fabrication by measurement of the wave group velocity as a function of frequency, derived in turn from the measurement of phase change of radiation transiting a section of waveguide as a function of frequency. Good agreement was obtained between the new and previous experimental methods, and with numerical predictions.

An application of these waveguides is as the gain section of a CRM based broadband radiation amplifier, known as a gyro-TWA. A suite of codes has been developed to predict the operating behaviour of these amplifiers. A script in the MAPLE package is used to solve the beam-wave coupled dispersion problem to predict the potential linear gain of the amplifier as a function of the beam and waveguide parameters. Using these approximate predictions for the experimental configuration, the PIC (Particle in Cell) code MAGIC was used to study the amplifier behaviour in the non-linear limit. These codes were applied to a previous experimental configuration and predicted amplifier linear gain of 55 dB, saturated gain of 39.5 dB, efficiency of 21 % and a -3 dB gain bandwidth (saturated) of 1.5 GHz (from 8.6-10.1 GHz). These were found to be in good agreement with the experimental measurements.

# **Chapter 1. Introduction**

## **1.1 History of the Electron Cyclotron Maser (ECM) Instability**

To satisfy applications where there exists a requirement for high power levels at micro to millimetre-wave frequencies, gyrodevice amplifiers and oscillators have attracted much recent research. Gyrodevice amplifiers are being developed for use in such applications as linear accelerators (LINACs) and millimetre-wave RADAR. Gyrodevice oscillators are developed mainly for use in magnetic fusion research applications but have found use in industrial applications such as metal joining and ceramic sintering. The mechanism responsible for the operation of such devices is known as the Electron Cyclotron Maser (ECM) instability. In the following sections the history and discovery of the ECM instability will be discussed, and devices which utilise it will be outlined. Particular emphasis of the research presented in the present thesis is the traveling wave interaction concept and therefore the Gyro Travelling Wave Tube (Gyro-TWT) will be dealt with in greatest detail.

Practical development of the electron cyclotron maser has taken sustained effort over twenty years. Also known as “electron cyclotron maser”<sup>1</sup> and “gyrotrons”<sup>2</sup>, these fast-wave gyrodevices utilise the cyclotron resonant maser condition to transfer energy from an electron beam to an electromagnetic wave.<sup>3</sup> The discovery of the ECM condition (or ‘instability’ as it is sometimes referred to) can be traced back to the work of the astrophysicist R. Q. Twiss who is credited as being the first to recognise an amplifying mechanism for free-electron gyroradiation<sup>4</sup> His approach utilised quantum mechanics, as did the work of Schneider who had no knowledge of Twiss's contribution. Around the same time, the work of Kleinwächter (1951), Müller (1956), and Tetel’baum (1957) on the use of periodicity of the electron beam rather than the circuit (thus negating the need for a slow wave structure) was furthered by Gaponov (1959), Pantell<sup>5</sup> (1959) and Beck and Mayo (1960). Around this time the Weibel interaction – where phase bunching occurs due to the axial forces – was predicted. In 1959, Schneider published a paper describing the ECM mechanism<sup>6</sup>. In this work, he noted the significance of the relativistic change in effective mass with energy of electrons in a static magnetic field. This improved upon the observations of Twiss by describing the process by which the electron beam

could gain energy from the electromagnetic wave. Also in 1959 Gaponov and Zheleznyakov of the USSR, who had been researching the interaction of charged particles with fast electromagnetic waves published a paper on the subject, but this time using a classical approach<sup>7</sup>.

Experimental verification of the ECM instability came in the early 1960's. This work was carried out by Pantell<sup>8</sup>, Chow and Pantell<sup>9</sup> Bott<sup>10,11</sup> and Feinstein<sup>12</sup>. Although successful, the experimental results were far from impressive in comparison to those for conventional microwave tubes and hence the research efforts diminished by 1965. This was owing to the fact that although they did in fact demonstrate experimentally the expected effects due to the ECM instability, they were unable to decisively prove that this was the only possible instability to explain the experimental measurements. Hirshfield and Watchel<sup>13</sup> were to carry out the work that would ensure that the ECM interaction existed within the system by imposing conditions ensuring both operation below the start oscillation condition and the absence of any axial synchronism. The research in Russia carried on, and in 1974 some significant results were obtained for gyro-oscillators<sup>14</sup>. Since the mid 1970's progress in this area has been steady<sup>15</sup>, with ever-increasing power levels and operating frequencies in gyro-oscillators. It is notable though that improvement in gyro-amplifiers has been much less dramatic – this is due to their complex amplification circuits (further information concerning the history of the ECM instability is also widely available).

Much research has been done on conventional (or smooth-bore) gyrotron travelling wave tube (gyro-TWT)<sup>16,17</sup>. These devices produce amplification of an electromagnetic wave by utilizing the CRM instability, with a non-resonant RF structure to obtain the traveling wave interaction. Their advantage lay in the fact that they were able to amplify fast waves with no delicate slow wave structure and used instead a smooth-bore waveguide. Interest in research waned however when it was realized that performance was susceptible to oscillations and velocity spread.

Recently interest in the area of broadband gyro-amplifiers has been renewed with a focus on newer devices such as the gyro-travelling wave amplifier (Gyro-TWA). Such devices were clearly attractive due to their ability to amplify high power, broadband radiation at the micro-millimetre wavelengths with good phase stability. The device was first described theoretically in 1998<sup>18,19</sup> Experimental work also carried out in 1998<sup>20</sup> confirmed the device's potential to produce high efficiency and gain with a good stability to oscillations. In most recent times, focus has been centred mainly on experimental work to develop this new breed of amplifiers and to measure bandwidth and other important parameters for Gyro-TWAs<sup>21</sup>.

Further work has improved the mode selectivity of gyro-devices by the incorporation of large-orbit axis-encircling beams driving a demand for high-quality, stable axis-encircling beam sources. One attractive way to produce such an axis-encircling beam is achieved by the use of a non-adiabatic magnetic field reversal or cusp field as it is also known and this has therefore attracted recent research interest<sup>22,23,24,25,26,27</sup>. The axis-encircling beams are particularly valuable to ensure good mode selectivity given the complex mode spectrum generated in waveguides with corrugated walls<sup>28,29</sup>.

## **1.2 Development of Gyro-Devices**

In many applications where there is the need for high-power, broad-band microwave radiation, the fast-wave gyrodevice family are employed<sup>30</sup>. A relatively recent development in the area of microwave tubes, these may also be known as “electron cyclotron masers,” or more usually as “gyrotrons”. These devices utilise the cyclotron resonance maser instability in order to allow net energy transfer between the electron beam and the electromagnetic wave<sup>31</sup>. Another characteristic of gyro-devices is that the electromagnetic wave phase velocity is typically greater than the speed of light. Gyrodevices which meet this condition are known as fast-wave devices. The converse group of devices – with the phase velocity less than the speed of light - are known as slow-wave devices. Here, interaction circuits are designed so as to cause a reduction in the phase velocity of the electromagnetic wave below the speed of light, and thus the wave-electron beam synchronism may be satisfied for

linear electron beams. The advantage of the fast-wave devices over their slow-wave counterparts is the greater flexibility in positioning of the electron beam. In slow-wave devices the electron beam must be situated in close proximity to the circuit structure to permit strong energy exchange. This is due to the fact that the axial electric field strength induced by the structure's EM wave is high at this point and hence optimum coupling occurs. For the case of the fast-wave device the transverse electric fields of a hollow tube are used to modulate the transverse velocity of a gyrating beam giving strong resonance without delicate structures. This leads to the potential of higher peak and average powers.

Since the late 1970's, much work has been carried out by University of Strathclyde on high power RF devices. In particular, in the year 2000 a paper was published by the institution detailing a bench-mark experiment using a novel interaction structure which yielded exceptional performance. This device operated at a power of 1.1MW with an efficiency of 30%, peak gain of 37dB and a 21% band of interaction whilst also avoiding the onset of absolute instabilities (parasitic oscillations). More recent work<sup>32</sup> has centred on the development of this first gyro-TWA with its novel helically corrugated waveguide and the modelling of this system.

### **1.3 Gyro-Oscillators**

In general terms, an oscillator is a device which produces a periodic fluctuation. For such devices to work, it is sometimes necessary to use some kind of feedback mechanism which causes re-injection of part of the output signal back into the input in phase. This mechanism is known as positive feedback and allows the signal to be sustainable. Such an oscillator can be thought of as a sensitive amplifier with a feedback configuration. Alternatively, instabilities exist which exhibit complex solutions to frequency in their dispersion relations. These tend to be absolute instabilities and will exhibit growth in time often without external feedback. Gyro-oscillator devices<sup>33,34,35</sup> make use of the cyclotron resonance maser instability but as with other oscillators have a major inherent problem which limits their application

despite their high power performance, namely their phase output is not a controlled parameter.

## **1.4 Amplifiers**

An amplifier utilizes the situation where there exists a convective instability (or a growth of signal in space) to take a small amplitude input signal and produce a higher amplitude signal at the output through some mechanism of energy transfer. In this section we consider two types of amplifier – the resonant and the non-resonant amplifier.

### **1.4.1 Resonant Amplifiers**

An amplification device which includes some resonant cavity or interaction structure is termed a ‘resonant’ amplifier. Examples of such devices are klystrons and gyro-klystrons (the latter are so named usually because they are based on cavities in CRM resonance with a gyrating electron beam). These devices have bandwidth limited by the resonator ‘Q’s. In practice,  $\sim 1\%$  of centre frequency is typical for a Gyro-Klystron. They offer very high peak output at moderate average powers for any given frequency.

### **1.4.2 Non-resonant Amplifiers**

In the absence of any resonant circuit or interaction structure, an amplifier is known as ‘non-resonant’. An example of this is the gyro-TWT<sup>36,37,38,39</sup> and indeed the gyro-TWA<sup>40,41</sup> (as this is paramount to the work documented here it is presented in a separate section – Section 1.5) which belong to the family known as the gyro-amplifiers<sup>42,43,44</sup>. These devices have one important advantage over their resonant counterparts – the exclusion of any resonant cavity means that a gyro-TWT and/or gyro-TWA has much greater bandwidth capabilities than the gyro-klystron. The conventional gyro-TWT however has always struggled to realize this theoretical potential due to velocity spread issues and an unfortunate propensity to oscillate.

## **1.5 The Gyro-TWA**

A member of the non-resonant family of amplifiers, the gyro-TWA is a relatively new device which permits operation at high powers and over large bandwidths but with good phase control and so avoids the inherent problems of the gyro-oscillator. Research into non-resonant cyclotron amplifiers (Section 1.4) showed problems associated with velocity spread using smooth-bore interaction regions however and interest declined in gyro-TWT type devices, until the realisation of the novel dispersion characteristics using a small helical corrugation on the waveguide inner wall<sup>45,46,47</sup>. This in turn reduced the system's sensitivity to velocity spread. Using a large-orbit electron beam with this new interaction structure was found to increase mode selectivity and further enhance performance.

## **1.6 New Work**

The present work is aimed at delivering a step forward in the knowledge and understanding in gyro-TWA research by making use of novel modelling methods which serve to reduce experimental design time and cost. By the development of a complete software suite for simulation of the gyro-TWA experiment, it was intended to provide accurate predictions of all of the important experimental parameters and of experimental performance. Modern advancements in computer-based codes make it possible to simulate complex electromagnetic systems and are valuable for the simulation of the gyro-TWA experiment and the helically corrugated waveguide used as its interaction structure. It was proposed that the software suite would be benchmarked against existing experimental data. Modern vector network analysers offer the ability to directly measure the electrical/optical length of the waveguides. A new technique was developed based on this approach to allow the dispersion of short sections of helically corrugated waveguide to be measured for the first time at the University of Strathclyde.



## **Chapter 2. Theory**

## 2.1 Electromagnetic Theory

### Introduction

Microwave circuits differ from their low frequency analogues in that the wavelength is comparable to the circuit component size and one may no longer use simple lumped element circuit theory when describing such systems. It should be noted here that it would be entirely possible to treat low frequency analogue circuits in terms of electromagnetic fields as opposed to the standard technique of using currents, voltages etc. as circuit theory. In practice the simpler analysis offered by lumped element circuit theory is often preferred. Alternative approaches may use distributed circuit models or full electromagnetic theory, when dealing with high frequencies.

### 2.1.1 Maxwells Equations

The relationship between the charge and current distributions and electromagnetic field can be described by Maxwell's equations:

$$\nabla \cdot \mathbf{E} = \frac{\rho}{\epsilon_0} \quad (2.1) \quad \text{Gauss' Equation}$$

$$\nabla \cdot \mathbf{B} = 0 \quad (2.2) \quad \text{Gauss' Law for magnetism}$$

$$\nabla \times \mathbf{E} + \frac{\partial \mathbf{B}}{\partial t} = 0 \quad (2.3) \quad \text{Faraday's Law}$$

$$\nabla \times \mathbf{B} - \frac{1}{c^2} \frac{\partial \mathbf{E}}{\partial t} = \mu_0 \mathbf{J} \quad (2.4) \quad \text{Ampères Law}$$

Where,

$\mathbf{E}$  is the electric field strength ( $\text{Vm}^{-1}$ ),

$\rho = \rho_f + \rho_b$  is the total charge density ( $\text{Cm}^{-3}$ ) where  $\rho_f$  is the free charge density and

$\rho_b = -\nabla \cdot \mathbf{P}$  is the bound charge density,

$\mathbf{P}$  is the electric polarization ( $\text{Cm}^{-2}$ ),

$\mathbf{B}$  is the magnetic flux density (T),

$\mathbf{J} = \mathbf{J}_f + \frac{\partial \mathbf{P}}{\partial t} + \nabla \times \mathbf{M}$  is the total current density ( $\text{Am}^{-2}$ ),

$\mathbf{J}_f$  is the current density resulting from the motion of free charge,

$\frac{\partial \mathbf{P}}{\partial t}$  is the polarization current density in a dielectric,

$\nabla \times \mathbf{M}$  is the equivalent current density in magnetized matter,

$\mathbf{M}$  is the magnetization ( $\text{Am}^{-1}$ ),

$c$  is the speed of light ( $3 \times 10^8 \text{ms}^{-1}$  approximately),

$\epsilon_0$  is the permittivity of free space ( $8.85 \times 10^{-12}$  farad/meter).

$\mu_0$  is the permeability in vacuum.

These equations form the foundation of electromagnetism. They can be applied to media which is nonlinear, inhomogeneous and nonisotropic although their application assumes that the media are stationary with respect to the coordinate axes and also that the coordinate axes do not rotate or accelerate<sup>48</sup>.

### **2.1.2 Electromagnetic Wave Propagation in Free Space**

Electromagnetic fields are able to propagate in free space, in dielectrics and, subject to certain conditions, in conductors, magnetic materials and plasmas. In order to study the basic properties of electromagnetic waves, we must study their propagation in free space.

As there can be no currents or electric charges in free space, Maxwell's equations (equations 1-4) become:

$$\nabla \cdot \mathbf{E} = 0 \quad (2.5)$$

$$\nabla \cdot \mathbf{B} = 0 \quad (2.6)$$

$$\nabla \times \mathbf{E} = -\frac{\partial \mathbf{B}}{\partial t} \quad (2.7)$$

$$\nabla \times \mathbf{B} = \mu_0 \varepsilon_0 \frac{\partial \mathbf{E}}{\partial t} \quad (2.8)$$

where the variables are the same as previously described. We can then uncouple the curl equations using the vector identity for the curl of  $(\nabla \times \mathbf{E})$  to obtain,

$$\nabla \times (\nabla \times \mathbf{E}) = \nabla(\nabla \cdot \mathbf{E}) - \nabla^2 \mathbf{E} = -\mu_0 \varepsilon_0 \frac{\partial^2 \mathbf{E}}{\partial t^2} \quad (2.9)$$

and hence we obtain the homogeneous wave equation,

$$\nabla^2 \mathbf{E} = \mu_0 \varepsilon_0 \frac{\partial^2 \mathbf{E}}{\partial t^2} \quad (2.10)$$

and similarly,

$$\nabla^2 \mathbf{B} = \mu_0 \varepsilon_0 \frac{\partial^2 \mathbf{B}}{\partial t^2} \quad (2.11)$$

These are wave equations, having the form:

$$\nabla^2 \Psi = \frac{1}{c^2} \frac{\partial^2 \Psi}{\partial t^2} \quad (2.12)$$

where  $c = \frac{1}{\sqrt{\epsilon_0 \mu_0}} = 3 \times 10^8 \text{ ms}^{-1}$ .

In free space, the electric field  $\mathbf{E}(\mathbf{r}, t)$ , the magnetic field  $\mathbf{B}(\mathbf{r}, t)$ , the scalar potential  $\phi(\mathbf{r}, t)$  and the vector potential  $\mathbf{A}(\mathbf{r}, t)$  all satisfy the above four-dimensional equation. The general solution of this equation is a superposition of an infinite set of one-dimensional waves travelling in all possible directions<sup>49</sup>.

### 2.1.3 Plane Waves

The simplest electromagnetic waves are plane waves. These are characterised by their phase being constant in a plane at any given instant in time for a wave propagating along an axis normal to the plane. A uniform plane wave would also have a fixed amplitude in the plane. We can reduce equations (2.10) and (2.11) to six identical, uncoupled scalar equations which have the form

$$\nabla^2 \psi(\mathbf{r}, t) = \mu_0 \epsilon_0 \frac{\partial^2 \psi(\mathbf{r}, t)}{\partial t^2} \quad (2.13)$$

where  $\psi$  represents  $E_x, E_y, E_z, B_x, B_y$  or  $B_z$ .

Now, by solving equation (2.13) for plane waves we obtain solutions of the form

$$\psi(\mathbf{r}, t) = \psi_0 e^{i(\mathbf{k} \cdot \mathbf{r} - \omega t)} \quad (2.14)$$

where  $\mathbf{k}$  is the propagation vector,  $\mathbf{r}$  represents the position vector,  $\omega$  is the angular frequency and  $t$  is time.

By back substitution of  $\psi$  into the wave equation (2.13) and using the relationships

$$\nabla^2 \psi = -k^2 \psi \text{ and } \frac{\partial^2 \psi}{\partial t^2} = -\omega^2 \psi, \text{ we find that } k^2 \psi = \omega^2 \mu_0 \epsilon_0 \psi. \text{ From this result, it can}$$

be concluded that that

$$v_p = \frac{\omega}{k} = v_g = \frac{\partial\omega}{\partial k} = c = \frac{1}{\sqrt{\epsilon_0\mu_0}} \quad (2.15)$$

where  $v_p$  is the phase velocity,  $v_g$  is the group velocity and  $\omega$  is the angular frequency.

The relative orientations of  $\mathbf{E}$ ,  $\mathbf{B}$ , and the propagation vector  $\mathbf{k}$  are shown in Figure 2.1.

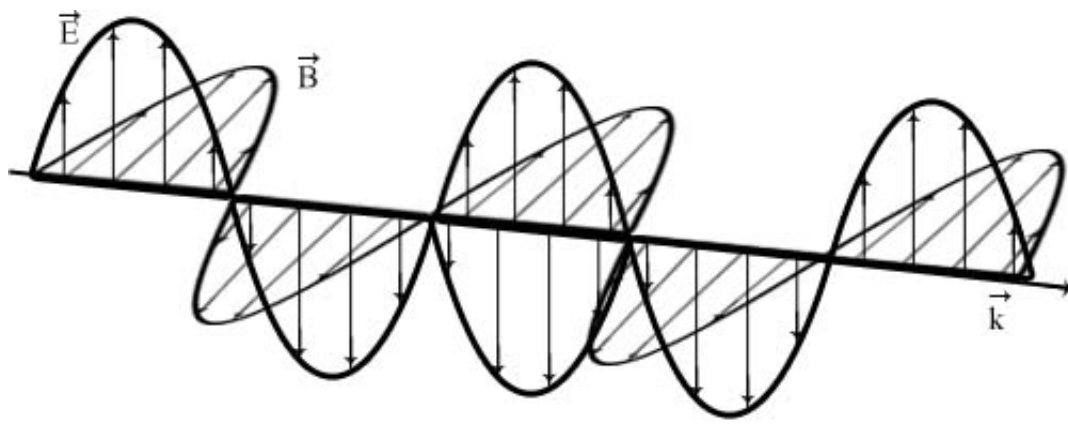


**Figure 2.1 Plane wave field variations.**

These orientations are implied by insisting that the fields  $\mathbf{E}$  and  $\mathbf{B}$  satisfy Maxwell's equations and equation (2.13). This is necessary as when solving equations (2.10) and (2.11), the coupling between  $\mathbf{E}$  and  $\mathbf{B}$  was removed – because these fields are not independent of each other the coupling must be restored. Notice that  $\mathbf{E}$  and  $\mathbf{B}$  are perpendicular to each other and to  $\mathbf{k}$ . Also, the alignment of the  $\mathbf{E}$  field is termed the *polarization* of the wave. It should be noted here that these results pertain only to infinite plane waves and do not hold for bounded or spherical waves.

#### **2.1.4 Polarization**

As mentioned in the previous section, *polarization* is the term used to denote the orientation of the  $\mathbf{E}$  field. Where the field of the plane wave  $\mathbf{E}$  only exists in one

transverse orientation as it propagates, we say that it is *linearly* polarized (Refer to Figure 2.2).

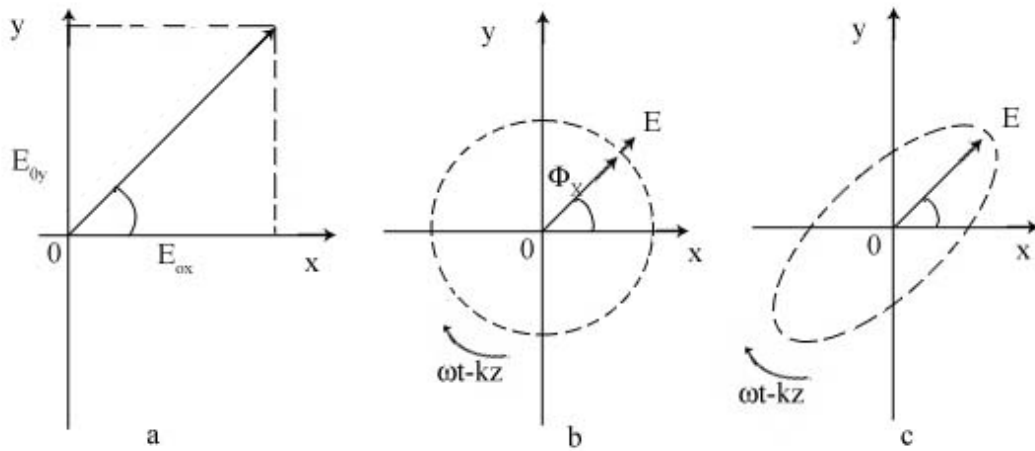


**Figure 2.2. The electric vector in a plane wave that is (a) linearly polarized, (b) circularly polarized, and (c) elliptically polarized.**

Taking a plane wave described by the equation (a solution of equation 2.15)

$$\mathbf{E}_0 = E_{0x} \hat{\mathbf{i}} + E_{0y} \hat{\mathbf{j}} \quad (2.16)$$

where  $E_{0x}$  and  $E_{0y}$  are constant and  $\hat{\mathbf{i}}$  and  $\hat{\mathbf{j}}$  are unit vectors, the direction of polarisation will be given by

$$\tan \theta = \frac{E_{0y}}{E_{0x}} \quad (2.17)$$

Now, because  $E_{0x}$  and  $E_{0y}$  are always in phase,  $\theta$  must be constant. However the actual magnitudes of both components of  $E_0$  can vary.

If we consider a plane wave where  $E_{0x}$  and  $E_{0y}$  have a constant phase difference ( $\pi/2$ )

and with differing amplitudes, then the wave is said to be *elliptically* polarized (Refer to Figure 2.2(c)).

If we then make the amplitudes the same we have a *circularly* polarized wave (Figure 4 part (b)).

The term *right-handed* polarisation refers to the electric vector rotating counter-clockwise as we look along the direction of propagation of the wave and *left-handed* obviously describes the opposite situation.

### **2.1.5 Poynting Vector**

In 1884, Poynting used Maxwell's equations to obtain an expression for the energy flow in electromagnetic waves in free space.

$$\mathcal{P} = \mathbf{E} \times \frac{\mathbf{B}}{\mu_0} \equiv \mathbf{E} \times \mathbf{H} \quad (2.18)$$

This is referred to as *Poynting's Vector* and is the energy per second passing through a unit surface area normal to the direction of propagation. By solving this equation for an electromagnetic wave it is possible to find the energy flow due to the wave.

### **2.1.6 Wave Impedance**

An important parameter in determining the transmission power and reflection when dealing with electromagnetic energy flow between two media is the *wave impedance*,  $Z$ . For free space, this is defined as

$$Z_0 = \frac{E_{0x}}{H_{0y}} = \frac{\mu E_{0x}}{B_{0y}} \quad (2.19)$$

By using plane wave solutions of the form of equation (2.14), it can be shown that



$$Z_0 = \mu_0 c \quad (2.20)$$

Now, by dimensional analysis of E (V m<sup>-1</sup>) and H (A m<sup>-1</sup>), it is apparent that the wave impedance, Z, has the same dimensions as an electrical circuit impedance i.e. the ohm. The usual value for Z in free space is

$$Z_0 = 377\Omega$$

It should also be remembered here that the speed of light, c, in free space is determined by the following relation

$$c = \sqrt{\frac{1}{\mu_0 \epsilon_0}} = 3 \times 10^8 \text{ ms}^{-1} \quad (2.21)$$

where  $\mu_0$  is the magnetic permeability ( $4\pi \times 10^{-7} \text{ Henrysm}^{-1}$ ) and  $\epsilon_0$  is the dielectric constant ( $\frac{1}{36\pi} \times 10^{-9} \text{ F m}^{-1}$ ). Thus it can be observed that for materials with  $\mu_0$  and  $\epsilon_0$  differing from free space, the impedance and speed of propagation will alter accordingly.

### 2.1.7 The Skin Effect

Consider the situation when an electromagnetic wave is propagating through air and impinges on a good conductor. Now, because there is an *impedance mismatch* between the surface of the conductor and the air, most of the wave's energy is reflected. Currents are induced in the surface of the conductor by the impinging electromagnetic wave. The current density is a maximum at the surface of the material and decreases exponentially with depth into the conductor. The *skin depth*,  $\delta$ , is the term used to describe the point at which the current density is reduced to 1/e of its value at the surface and is given by

$$\delta = \sqrt{\frac{2}{\omega\mu_r\sigma_s}} \quad (2.22)$$

where  $\omega$  is the frequency of the electromagnetic wave in radians ( $= 2\pi f$  Hz),  $\mu_r$  is the relative permeability (relative to the permeability of free space) of the conductor, and  $\sigma_s$  is the conductivity of the material.

The skin depth is very small at microwave frequencies<sup>50</sup>. This factor is beneficial in situations where a conductor is being used to shield a region from electromagnetic waves; it also means however those high frequency wall currents on transmission lines are strongly confined to the surface.

### **2.1.8 Waveguide Theory**

#### **Introduction**

It has already been established that electromagnetic waves can propagate freely in free space, but in microwave systems we must somehow efficiently transmit microwave energy from one point to another. This is achieved by using a waveguide consisting of conducting metallic tube which can contain the electromagnetic waves. It is now necessary to examine the theoretical and physical aspects of such a device in order to understand their operation.

### **2.1.9 Reasons for Using Coaxial Lines & Waveguides**

In microwave applications, microwave energy is transported to and from microwave devices via waveguides or coaxial lines. A waveguide is simply a metallic pipe made from a non-magnetic metal and is of rectangular or circular cross-section. A coaxial line can be thought of as a circular waveguide with a conductor positioned at its centre.

Prior to explanations of how waveguides actually operate, it is probably necessary to outline why such devices are actually needed. At lower frequencies i.e. in most dc electrical circuits the use of simple open-wire conductors is common providing all the circuit dimensions are much smaller than the wavelengths of the radiation. However, as the frequency of operation increases three main problems arise:

1. From elementary electrostatics, when two wires are placed side by side their electric and magnetic fields couple signals from one wire to the other which then leads to the phenomena known as 'crosstalk' and power loss to any nearby conductors. This can be combatted at low and medium frequencies by introducing a 'twist-pair' wire configuration which assists in confining the fields and also by the shielding (using metals) of individual 'twist-pairs'.
2. At higher frequencies, the connecting wires can actually begin to radiate signals i.e. they can act as antennae. To reduce this problem the introduction of metallic shielding around the wires is necessary.
3. If we have a high enough frequency and the wavelength of the signal is sufficiently short so that the lengths of conductors are a reasonable fraction of a wavelength then complex, distributive, capacitive and inductive effects become apparent. This can be understood by considering that as each wire possesses an inductance, and there is a capacitance between wires, then each wire pairing must also have an impedance which is relative to the dimensions of the wires and their relative locations relative. It should be noted then that, if this impedance varies in any way, then the signal propagating through the wire may be partially reflected at each change in impedance.

Thus the need for waveguides is clear; these problems can actually be managed by the proper use of waveguide structures.

### 2.1.10 Waveguide Operation

Waveguides are hollow metallic pipes usually constructed from aluminium, copper or other such high-conductivity non-magnetic metals. They are available in several different cross-sections, the most common being the rectangular, circular and coaxial waveguides. However, other geometries are used in certain applications – such as the helical waveguide investigated in this thesis. Although the fundamental theoretical treatment of wave propagation in all waveguides is identical, the differing geometries of each waveguide type must be taken into account when applying the boundary conditions and can result in some rather complex analysis. In this section, the theory behind the simplest type of waveguide – the rectangular cross-section – will be developed. It is important to note that for the other geometries, this theory is simply extended.

Consider a high frequency oscillator with its output connected to a rectangular waveguide. At a given time, there exists a surplus of electrons on the top wall of the waveguide and a deficiency on the bottom wall. This gives rise to an electric field, and an associated potential difference exists between opposing faces of the waveguide (Refer to Figure 2.3).

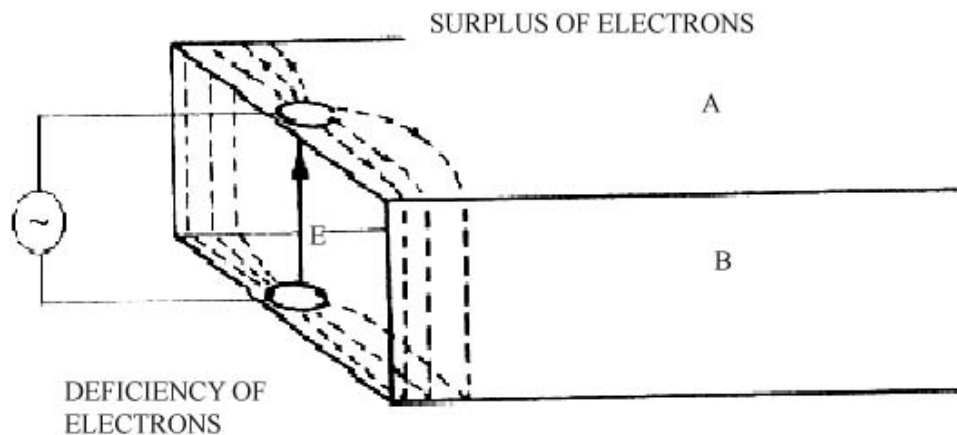


**Figure 2.3 Illustration of potential difference between opposing faces a planar waveguide.**

Currents are induced and so we also have a magnetic field which is unable to completely encircle the current due to the wall of the waveguide as shown in Figure 2.4 by the vector  $\mathbf{H}$ .

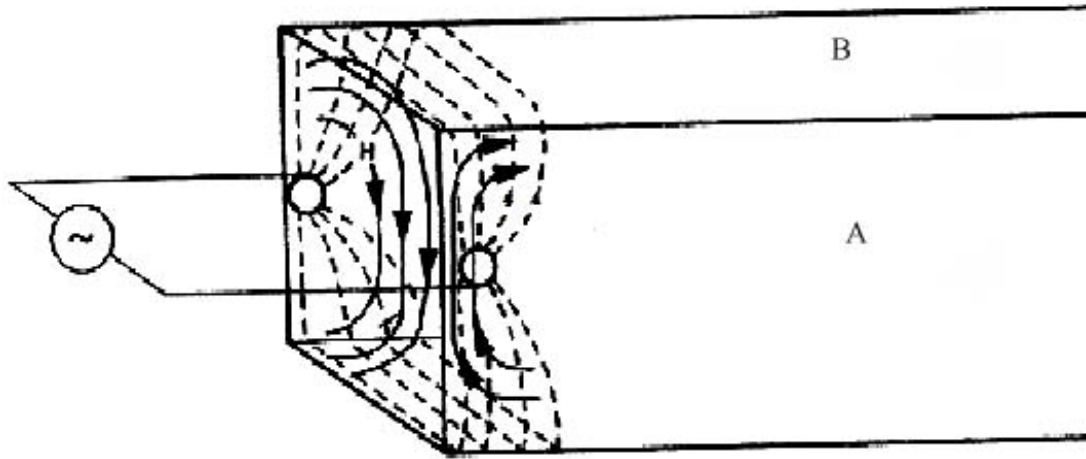


**Figure 2.4 Magnetic fields in opposing faces of planar waveguide.**

As the polarity of the oscillator is reversed the existing fields induce further currents along the waveguide which results in additional  $\mathbf{E}$  and  $\mathbf{B}$  fields and so this process continues along the length of the waveguide. In the inside of the waveguide, we can visualise the electrons in a region first rushing to the top of the structure and then to the bottom. These charge distributions propagate along the wavelength.

Refer to Figure 2.5 showing three such states each separated by half of one cycle of the oscillator.

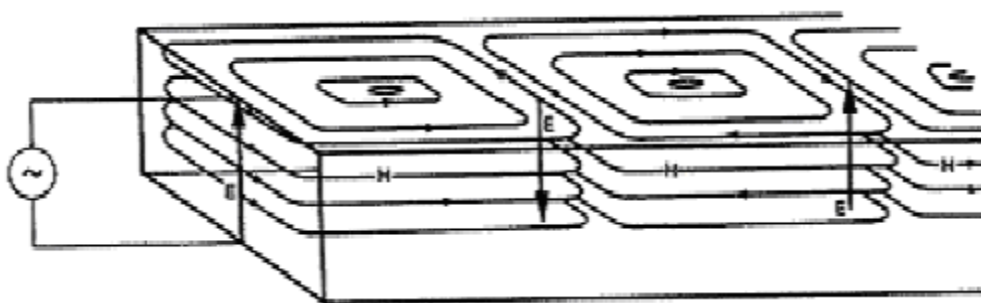


**Figure 2.5 Charge distributions propagating along wavelength.**

From this diagram, it can be clearly seen that the  $\mathbf{E}$  vector appears to be moving along the length of the waveguide; its orientation changing after each half-cycle. In

other words we have in effect an electromagnetic wave propagating along the length of the waveguide.

## 2.2 Waveguide Theory

### 2.2.1 Constraining of an Electromagnetic Wave in a Tube-Like Structure

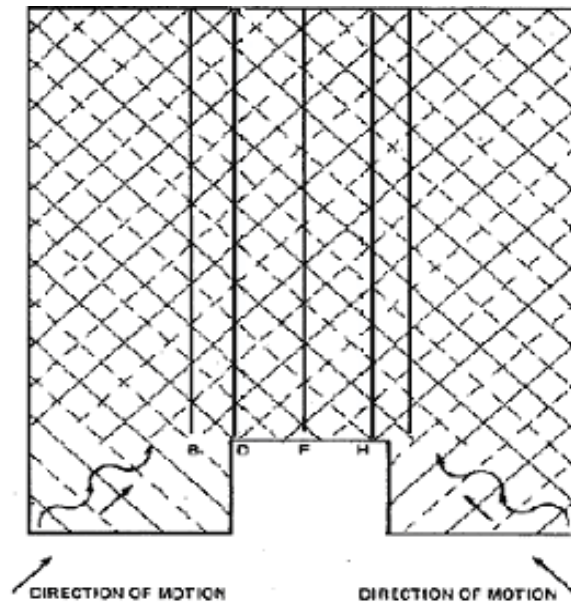


**Figure 2.6 Diagram showing the propagation of two electromagnetic waves.**

In analysing the theory behind waveguide operation, it is necessary to first establish why electromagnetic waves can be confined in such a way.

Consider the situation depicted in Figure 2.6 where two electromagnetic waves of equal wavelengths and amplitudes propagate across each other with their electric fields at right angles to the paper and magnetic fields in the plane of the paper. The solid lines represent wave crests (with electric field above the plane of the paper) and the dotted lines wave troughs (with magnetic field below the plane of the paper). Now it can be seen that along the lines AB, CD, EF and GH we have the crests of one wave superimposed on the trough of another wave. Due to the fact that the waves are of equal amplitude, each 'crossing' point along these lines corresponds to zero electric field. This suggests that, by insertion of sheets of metal along any of these lines, no change to the picture occurs whatsoever since no current would be

induced in the walls. Thus it may be assumed that because insertion of these metal sheets along lines of zero electric field have no influence on the system, it is possible for a wave to propagate between such sheets.

### 2.2.2 Guide Wavelength

The wavelength of the electromagnetic wave inside the waveguide is different to that of the free space wavelength of the wave. This can be explained by following on from the example in the preceding section (2.2.1). If we consider a region between two parallel metal plates (with each plate placed along a line of zero electric field) as in Figure 2.7, it is apparent that the electric vectors on the outside lines subtract as before due to the superimposition of a wave crest with a wave trough.

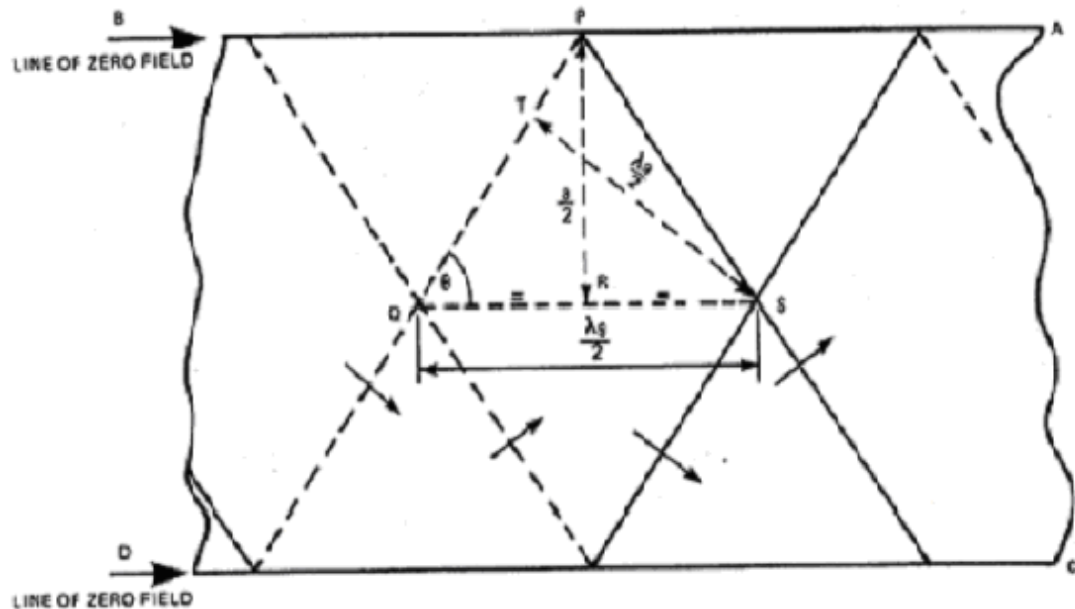


**Figure 2.7 Guide wavelength in a parallel plate waveguide.**

However, intersections of two wave crests (one from each wave) and two wave troughs along the centre line result in a composite wave with double the amplitude of the original wave. Bearing in mind that the picture without the sheets of metal would extend out as before with the same pattern, it can be concluded that the separation of any pair of parallel full lines corresponds to the separation distance between two crests of the electric field when in free space. This separation is equivalent to one

free space wavelength and will be referred to here as  $\lambda_a$ . Thus the separation between any parallel full line and a dotted line is equal to one half of a free space wavelength so  $TS = \frac{\lambda_a}{2}$ .

Now, the wavelength of the composite wave inside the waveguide is obviously equivalent to the distance between two intersections of solid lines (maxima) and will be referred to as  $\lambda_g$ . Considering this, the distance QS between a maxima intersection and a minima intersection is equal to one half a guide wavelength ( $QS = \frac{\lambda_g}{2}$ ).

This illustrates, as discussed earlier, that the guide wavelength differs from the free space wavelength and, furthermore, that the guide wavelength is always greater than the free space wavelength.

### **2.2.3 Relationship Between Guide Wavelength and Free Space Wavelength**

Utilising Figure 2.7 from the preceding section, it is possible to use elementary mathematics to obtain a relationship between the guide wavelength,  $\lambda_g$ , and the free space wavelength,  $\lambda_a$ .

Referring to Figure 2.7 and using 'a' as the separation between the waveguide walls,

$$PR = \frac{a}{2}$$

$$ST = \frac{\lambda_a}{2}$$

$$QS = \frac{\lambda_g}{2}$$



Letting the angle  $\text{PQR} = \theta$  and considering the triangle PRQ,

$$\tan \theta = \frac{\text{PR}}{\text{RQ}} = \frac{a/2}{\lambda_g/4} = \frac{2a}{\lambda_g} \quad (2.23)$$

Now, for the triangle STQ

$$\sin \theta = \frac{\text{ST}}{\text{SQ}} = \frac{\lambda_a/2}{\lambda_g/2} = \frac{\lambda_a}{\lambda_g} \quad (2.24)$$

Using the relationship

$$\tan^2 \theta = \frac{\sin^2 \theta}{\cos^2 \theta} = \frac{\sin^2 \theta}{1 - \sin^2 \theta} \quad (2.25)$$

By substitution of (2.23) and (2.24) into (2.25) we have

$$\left( \frac{2a}{\lambda_g} \right)^2 = \frac{(\lambda_a/\lambda_g)^2}{1 - (\lambda_a/\lambda_g)^2} \quad (2.26)$$

which then reduces to

$$\left( \frac{1}{\lambda_g} \right)^2 = \left( \frac{1}{\lambda_a} \right)^2 - \left( \frac{1}{2a} \right)^2 \quad (2.27)$$

This formula (2.27) relates the guide wavelength to the free space wavelength and also has important implications for the dimensions of the waveguide. It can clearly be seen that if the free space wavelength  $\lambda_a$  was to be equal to  $2a$  then the guide wavelength  $\lambda_g$  is infinite and hence no wave propagation can occur. Thus, we require

that the free space wavelength be less than  $2a$  in order to obtain real values for  $\lambda_g$ .

In conclusion, propagation of electromagnetic waves can only take place through the waveguide if the free space wavelength is less than twice the width of the waveguide. The point at which  $\lambda_a = 2a$  is termed 'cut-off'. Hence a waveguide can also be thought of as a type of high pass filter which will only allow propagation of radiation above a certain frequency  $f_c$ .

Considering the boundary conditions, it is apparent that the model described in Section 2.2.1 can be extended to include two more walls perpendicular to both the propagation and polarisation – resulting a rectangular cross-section waveguide. The addition of such walls does not affect in any way the field pattern of the simpler parallel planes model; in fact it only serves to contain the radiation propagating through the waveguide.

With the model of the rectangular waveguide complete, it is now possible to examine the field pattern within such a device. It is now necessary to apply the boundary conditions to this rectangular cross-sectioned, hollow conducting pipe. By applying these aforementioned boundary conditions to the wave equations, a large number of possible solutions can be found. These solutions are referred to as *waveguide modes*.

#### **2.2.4 Boundary Conditions**

When dealing with an electromagnetic wave incident on a metal sheet of perfect conductor, certain boundary conditions must be imposed to prevent any discontinuity of the wave occurring at the interface. This is due to the fact that  $\epsilon$  and  $\mu$  change within a fraction of a wavelength of an electromagnetic wave, causing a sharp discontinuity. In this section, the rectangular waveguide in question is assumed to have perfectly conducting walls and therefore these boundary conditions must be adhered to. These boundary conditions are critical in determining the allowed field configuration.

It has already been established that electromagnetic waves can propagate in free space. The propagation of these waves through a waveguide is similar, but with one critical difference – the energy being transported is subject to the physical limits of the waveguide. These limits correspond to three *boundary conditions* which are applied to the wave equations (2.10) and (2.11):

1. For an electric field to exist at the surface of the conductor it must be perpendicular to the surface i.e.  $\mathbf{E}_{//} = 0$ .

In the case of electromagnetic waves the electric vector  $\mathbf{E}$  vanishes inside a perfect conductor. As it is necessary to maintain continuity of the  $\mathbf{E}_{//}$  component at an interface, it must be zero at the walls of the waveguide; if  $\mathbf{E}_{//}$  is non-zero there would be a voltage difference across that particular wall. However, such voltage differences cannot exist as the surface electrons flow in such a way as to negate the voltage difference.

2. The perpendicular component of the magnetic field near a perfect conductor must be zero i.e.  $\mathbf{H}_{\perp} = 0$  (where  $\mathbf{H}$  is the magnetic field strength, given by  $\mathbf{H} = \frac{\mathbf{B}}{\mu}$ ).

As before, continuity must be maintained so this is why the  $\mathbf{H}_{\perp}$  component must be zero at the waveguide walls. Currents would circulate in the conducting walls to eliminate any normal  $\mathbf{H}$ .

3. For TE waves (waves with electric field purely in the transverse direction), the transverse gradient of the propagation direction oriented component at the wall must be zero i.e.  $\partial \mathbf{H}_{mz} / \partial z = 0$ .

This particular condition exists because  $H_{mz}$  having a gradient along the direction of propagation would induce a gradient in the peak value of the electric field along the

axis of propagation. It is not possible for this situation to physically occur as the surface currents in the structure act so as to oppose this.

### 2.2.5 Classification of Modes

In waveguides, although there are an infinite number of possible solutions to the wave equations i.e. an infinite number of possible modes, it is normal practice to assign modes to one of three categories:

1. Transverse Electric (or TE) Modes
2. Transverse Magnetic (or TM) Modes
3. Transverse Electric and Magnetic (or TEM) Modes

### 2.2.6 Rectangular Waveguides and the Dominant TE Mode

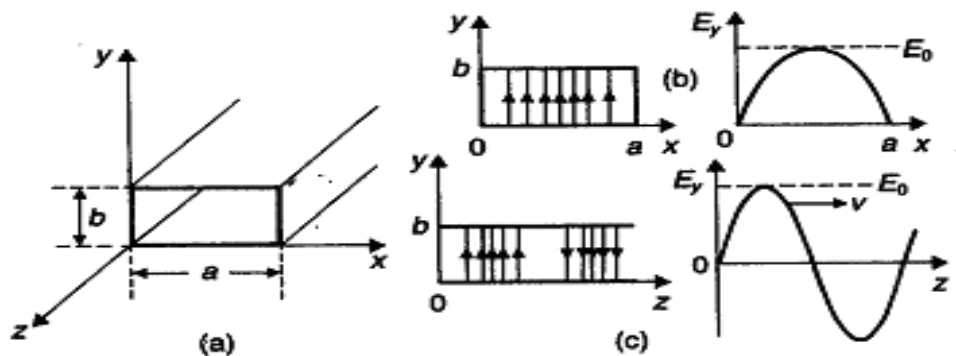


**Figure 2.8. Rectangular waveguide,  $x = a$ ,  $y = b$ . (b) Simple transverse electric (TE) mode. (c) Wave travels with phase velocity  $v$  along the waveguide (at  $t = 2\pi/4\omega$ ).**

In the rectangular waveguide, shown in Figure 2.8 (where the dimensions are  $x = a$ ,  $y = b$ , with  $a \approx 2b$  and propagation is along the  $z$  axis), the simplest mode of propagation is the **TE mode** where the electric field is transverse to the direction of propagation. As there is no tangential component of  $\mathbf{E}$  at the surface of the conductor, the E-field must be zero at  $x = 0$  and  $x = a$  order. Also, in the lowest order there must be a single maximum in the centre, so

$$E_y = E_0 \sin k_x x \quad (2.28)$$

where  $k_x = 2\pi/2a$ . If we assume that the wave propagates with a velocity  $v = \omega/k_g$  with  $k_g = 2\pi/\lambda_g$ , then we have the situation depicted in Fig. 2.8 part (c)

$$E_y = E_0 \sin k_x x \exp i(\omega t - k_g z) \quad (2.29)$$

where  $k_g$  has to satisfy Maxwell's equations.

Now, as  $\frac{\partial E_y}{\partial y} = 0$ ,  $E_y$  must satisfy equation 2.5 ( $\nabla \cdot \mathbf{E} = 0$ ). From the remaining Maxwell equation we again obtain equation,

$$\nabla^2 \mathbf{E} = \mu\epsilon \frac{\partial^2 \mathbf{E}}{\partial t^2} = \frac{1}{c^2} \frac{\partial^2 \mathbf{E}}{\partial t^2} \quad (2.30)$$

Considering that here we have  $\mathbf{E} = 0\hat{\mathbf{i}} + E_y\hat{\mathbf{j}} + 0\hat{\mathbf{k}}$ , we can now obtain the following result from equations (2.28) and (2.29):

$$\nabla^2 \mathbf{E} = -k_x^2 E_y + 0 - k_g^2 E_y$$

and

$$\frac{\partial^2 E_y}{\partial t^2} = -\omega^2 E_y$$

so we now have

$$k_x^2 + k_g^2 = \omega^2 / c^2 \quad (2.31)$$

As this is the fundamental or *dominant* mode,  $k_x = 2\pi / 2a$ , it is possible to rearrange equation (2.27) as

$$\frac{1}{(2a)^2} + \frac{1}{\lambda_g^2} = \frac{1}{\lambda_0^2}$$

which matches the result found earlier in Section 2.1.14.

It is also necessary to obtain an expression for the magnetic field in this dominant TE mode. From equation (2.7), we have

$$\nabla \times \mathbf{E} = \frac{-\partial \mathbf{B}}{\partial t}$$

As  $\mathbf{E} = E_y \hat{\mathbf{j}}$ , the curl has only two finite components, so

$$\frac{-\partial E_y}{\partial z} \hat{\mathbf{i}} = \frac{-\partial B_x}{\partial t} \hat{\mathbf{i}}$$

$$\frac{+\partial E_y}{\partial z} \hat{\mathbf{k}} = \frac{-\partial B_z}{\partial t} \hat{\mathbf{k}}$$

and  $B_y = 0$ . Then by substitution of equation (2.29) for  $E_y$  and by setting  $k_x = \frac{\pi}{a}$ ,

$$B_x = -\frac{k_g}{\omega} E_0 \sin \frac{\pi x}{a} \exp i(\omega t - k_g z) = -\frac{k_g}{\omega} E_y \quad (2.32)$$

$$B_z = \frac{i\pi}{a\omega} E_0 \cos \frac{\pi x}{a} \exp i(\omega t - k_g z) \quad (2.33)$$

and so we obtain a relationship between the x and z components of the magnetic field

$$\frac{B_x}{B_z} = + \frac{ik_g a \sin(\pi x/a)}{\pi \cos(\pi x/a)} \quad (2.34)$$

Figure 11 shows the electric and magnetic fields for the TE mode described by the above magnetic field distribution.

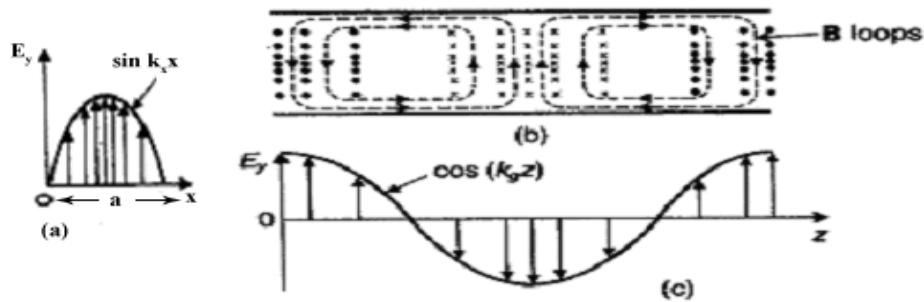


**Figure 2.9. Electric and magnetic fields of a propagating wave in the fundamental TE mode: (a) end view; (b) central section; (c) side view.**

### 2.2.7 Transverse Electric Modes

It has already been established that the dominant TE mode in a rectangular waveguide has only one component of electric field  $\mathbf{E}$  ( $E_y$ ) but two components of magnetic field  $\mathbf{B}$  ( $B_x$  and  $B_z$ ). When dealing with higher order TE modes however, we must take into account solutions satisfying the boundary conditions at harmonics of the wavenumbers:

$$k_x = m \frac{\pi}{a}, \text{ and } k_y = n \frac{\pi}{b} \quad (2.35)$$

The mode is then described in the nomenclature  $TE_{mn}$  where  $m$  is the number of half wave variations of the electric field across the width of the waveguide,  $a$ , and  $n$  is the number of half wave variations of the electric field across the narrow dimension,  $b$ .

Note that the fields for such higher order TE modes must also satisfy the Maxwell equations as before using  $(t, z) \equiv (\omega t - k_g z)$ :

$$\begin{aligned}
 E_x &= E_{0x} \cos k_x x \sin k_y y \exp i(t, z) \\
 E_y &= E_{0y} \sin k_x x \cos k_y y \exp i(t, z) \\
 E_z &= 0 \\
 B_x &= B_{0x} \sin k_x x \cos k_y y \exp i(t, z) \\
 B_y &= B_{0y} \cos k_x x \sin k_y y \exp i(t, z) \\
 B_z &= B_{0z} \sin k_x x \cos k_y y \exp i(t, z)
 \end{aligned} \tag{2.36}$$

where it should be noted that the components  $E_{0x}$ ,  $E_{0y}$ ,  $B_{0y}$ ,  $B_{0z}$  are all independent of  $x$ ,  $y$  and  $z$ . It is also possible to obtain a dispersion relation between the propagation wave vector and the frequency

$$k_x^2 + k_y^2 + k_g^2 = \omega^2/c^2 \tag{2.37}$$

which also leads to a relation for the *cut-off wave number*,

$$k_c^2 = \frac{m^2 \pi^2}{a^2} + \frac{n^2 \pi^2}{b^2} \tag{2.38}$$

It is now possible to write the expression for the cut-off frequency as

$$(v_c)_{m,n} = \frac{c}{2} \left( \frac{m^2}{a^2} + \frac{n^2}{b^2} \right)^{1/2} \tag{2.39}$$

This clearly shows that as well as the dominant cut-off frequencies determining the possibility of radiation propagation along the waveguide, there are cut-off frequencies which can determine which *modes* are able to propagate. It is important to take this fact into consideration if a waveguide is to be designed for use with a



single mode (fixed frequency). Usually in the design of such devices, the width (a) of the waveguide is carefully selected to allow radiation to propagate but to prevent the excitation of higher modes (discussed later in Section 2.5.2).

### **2.2.8 Transverse Magnetic Modes**

In the case of Transverse Magnetic Modes (TM modes), the magnetic fields are always transverse to the direction of propagation (notated here by z). For this particular type of mode it is necessary to use the boundary conditions  $E_z = 0$  at  $x = 0$  and  $y = 0$ ,

$$E_z = E_{0z} \sin k_x x \sin k_y y \exp i(\omega t - k_g z) \quad (2.40)$$

It is then possible to derive the other terms by applying the boundary conditions to Maxwell's equations remembering that  $B_z = 0$  by definition. Equation (2.38) gives the cut-off frequencies for the  $TM_{mn}$  modes but it should be noted that the lowest mode is  $TM_{11}$ . This can be determined by referring to equation (2.39); it is quite clear that no  $TM_{m0}$  or  $TM_{0n}$  modes can exist. This can be extremely useful as it allows the selection of a waveguide which will only propagate one mode (the  $TE_{10}$  mode) for a particular frequency.

### **2.2.9 Transverse Electric and Magnetic Modes**

A problem arises here as transverse electric and magnetic modes (or TEM modes) cannot satisfy the boundary conditions used previously for a closed, conducting waveguide. This is due to the fact that they possess no longitudinal electric or magnetic fields.

In a TEM guided wave it can be shown that the electric field in a plane perpendicular to the direction of propagation is derivable from a potential in the same way as an electrostatic field. In doing this, the electric field is shown to depend on the gradient of potential  $V$  in the waveguide. The potential around the waveguide is constant, so

$E_{\perp} = 0$  at the walls and, due to the fact that there is no voltage gradient across the walls of the waveguide, there is zero electric field inside the waveguide. Also, since  $\nabla \times \mathbf{E} = -\frac{\partial \mathbf{B}}{\partial t}$  and  $\mathbf{E} = 0$ , there is zero magnetic field. Thus it is apparent that because no  $\mathbf{E}$  or  $\mathbf{H}$  field exists here, TEM waves cannot propagate in a hollow conducting tube.

Thus in order for TEM waves to propagate there must be two distinct conductors which can then be at differing potentials. In such structures, the TEM can exist at any frequency and it can be shown<sup>49</sup> that it will travel with the velocity of the plane waves associated with the medium between the conductors. An important example of such a system is the coaxial cable.

## **2.3 Circular Waveguides**

### **2.3.1 Introduction**

With the basic theory behind the rectangular cross-section waveguide already established, it is now possible to extend this to a waveguide of circular cross-section. In cylindrical waveguides, the field structure geometry is rather more complex than in that of the rectangular guide. As with the rectangular waveguide, TEM waves cannot propagate in cylindrical waveguides, only the TE, TM waves are possible.

### **2.3.2 Circular Waveguide Theory**

As we are dealing with a circular geometry, it is necessary to work in polar coordinates (refer to Figure 2.10). In establishing relations for the fields in a cylindrical waveguide, we are concerned with the solution of the equation

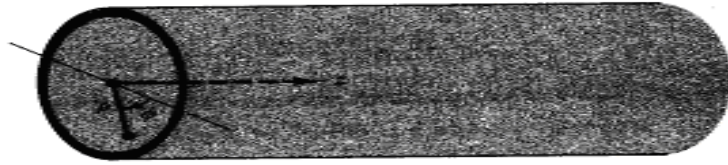


**Figure 2.10 Co-ordinates for circular waveguide.**

$$\left[ \frac{1}{\rho} \frac{\partial}{\partial \rho} \left( \rho \frac{\partial \psi}{\partial \rho} \right) + \frac{1}{\rho^2} \frac{\partial^2 \psi}{\partial \phi^2} + k_T^2 \gamma_c \right] = 0 \quad (2.41)$$

where  $k_T$  is the wavenumber transverse to the direction of propagation with  $k_T^2 = \gamma^2 + \omega^2 \mu \epsilon$  and  $\psi$  represents either  $E_z$  or  $H_z$ . It can be shown that a solution to this equation is of the form

$$\psi = [AJ_m(k_T \rho) + BY_m(k_T \rho)] [C \cos m\phi + D \sin m\phi] \quad (2.42)$$

where  $J_m(u)$  and  $Y_m(u)$  are Bessel functions of the first and second kind respectively.

As there must be continuity of field components away from the conducting surface for the circular waveguide, it is necessary to make  $B = 0$ . It should also be noted that due to the circular geometry here the constant  $m$  must be an integer since an increase in angle of  $2\pi$  must result in the same value for the field component. In the case of coaxial lines (see Section 2.6) it is not necessary to make  $B = 0$  since the axis would not then be in a physically relevant region.

On closer inspection of equation (2.42), it is apparent that we can replace the second bracket term by  $A e^{\pm im\phi}$ . Therefore the solution is of the form

$$\psi = AJ_m(k_T \rho) e^{\pm im\phi} \quad (2.43)$$

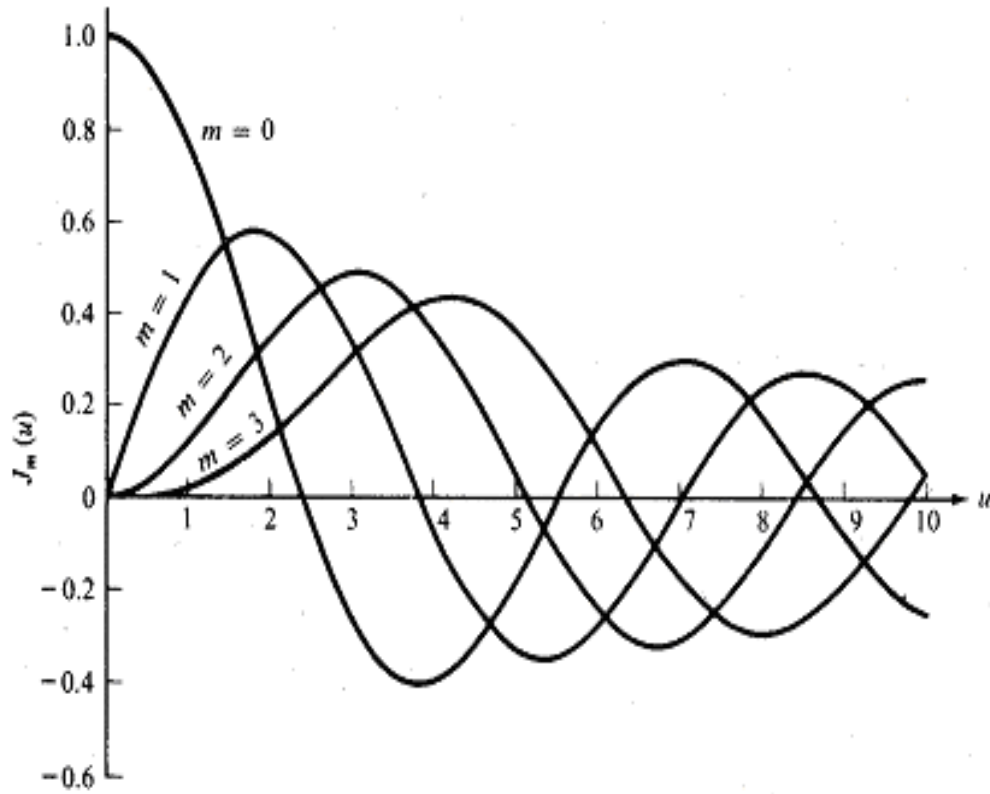


**Figure 2.11 The oscillating nature of Bessel functions.**

Figure 2.11 shows the form of  $J_m(u)$  for some values of  $m$ . Note that it is also necessary to apply boundary conditions, namely that  $\psi$  (for TM modes) or  $\frac{\partial \psi}{\partial \rho}$  (for TE modes) must equal zero at  $\rho = a$  i.e. at the waveguide radius. By application of one of these conditions, the possible values of  $k_r$  are limited.

It can be shown that the oscillating nature of the Bessel function shown in Figure 2.11 carries on indefinitely, with  $J_m(u)$  equal to 0 at a sequence of points

$$J'_m(u) = 0, \text{ with } u = t_{mn} \text{ where } m = 0, 1, 2, \dots \text{ and } n = 1, 2, \dots$$

Now, it is obvious that the sequence of maxima and minima of  $J_m(u)$  each correspond to a point where the derivative  $J'_m(u)$  vanishes and therefore this gives rise to another sequence

$$J'_m(u) = 0, \text{ with } u = s_{mn} \text{ where } m = 0, 1, 2, \dots \text{ and } n = 1, 2, \dots$$

It follows then that for the TM mode (where the variable  $\psi$  represents  $E_z$  which must vanish at  $\rho = a$  to satisfy boundary conditions),  $k_T$  must satisfy the condition

$$k_T a = t_{mn} \quad (2.44)$$

In the case of the TE mode,  $\psi$  represents  $H_z$  hence with  $\frac{\partial H_z}{\partial \rho} = 0$  at  $\rho = a$  we have

$$k_T a = s_{mn} \quad (2.45)$$

Thus there is a sequence of discrete values of  $k_T$  for each azimuthal order of wave mode.

### **2.3.3 TE Modes in Circular Waveguide**

Here, we have

$$H_z = A J_m(k_T \rho) \cos m \phi \exp(-\gamma z) \quad (2.46)$$

As mentioned previously, by application of the boundary condition (that the radial derivative of  $H_z$  must be zero at the surface of the waveguide) it is found that  $k_T$  must take on the discrete values described by equation (2.45). The propagation constant  $\gamma$  is given by

$$\gamma^2 = -\omega^2 \mu \epsilon + (s_{mn} / a)^2 \quad (2.47)$$

In common with the rectangular waveguide,  $\omega$  must exceed a certain value (for any given  $m$  and  $n$ ) before  $\gamma$  becomes imaginary and hence propagation becomes possible. In the case of the  $TE_{mn}$  mode,  $\omega$  must exceed  $\omega_{mn}$  so we have a series of *cut-off* frequencies defined by

$$f_{mn} = \omega_{mn} / 2\pi = s_{mn} / [2\pi a \sqrt{(\mu\epsilon)}] = s_{mn} v / 2\pi a \quad (2.48)$$

If  $\omega < \omega_{mn}$ , then we have  $\gamma = i\beta = i[\mu\epsilon(\omega^2 - \omega_{mn}^2)]^{1/2}$  and

$$\text{if } \omega > \omega_{mn}, \text{ then we have } \gamma = \alpha = [\mu\epsilon(\omega_{mn}^2 - \omega^2)]^{1/2} \quad (2.49)$$

In broad terms, it can be approximated that the wavelength corresponding to cut-off frequency is one-half of the circumference of the waveguide.

It can be shown that the components of the electric and magnetic fields in the TE<sub>mn</sub> mode are:

$$\begin{aligned} H_\rho &= -A(i\beta / k_T) J'_m(k_T \rho) \cos m\phi \\ H_\phi &= A(i\beta / k_T) (m / k_T \rho) J_m(k_T \rho) \sin m\phi \\ E_\rho &= \omega\mu H_\phi / \beta \\ E_\phi &= -\omega\mu H_\rho / \beta \end{aligned} \quad (2.50)$$

where  $\beta$  can be calculated from (2.48) for the mode in question.

### **2.3.4 TM Modes in Circular Waveguide**

For the TM mode

$$E_z = A J_m(k_T \rho) \cos m\phi \quad (2.51)$$

Then, by application of the condition that  $E_z=0$  at the walls of the waveguide ( $\rho = a$ ) and remembering that the possible values of  $k_T$  are given by equation (2.44), the propagation constant is given by

$$\gamma^2 = -\omega^2 \mu \varepsilon + (t_{mn} / a)^2$$

Thus the cut-off frequencies are defined by

$$f_{mn} = \omega_{mn} / 2\pi = t_{mn} v / 2\pi a \quad (2.52)$$

Then the components are found as before:

$$\begin{aligned} E_\rho &= -A(i\beta / k_T) J'_m(k_T \rho) \cos m\phi \\ E_\phi &= A(i\beta / k_T) (m / k_T \rho) J_m(k_T \rho) \sin m\phi \\ H_\rho &= -\omega \varepsilon E_\phi / \beta \\ H_\phi &= \omega \varepsilon E_\rho / \beta \end{aligned} \quad (2.53)$$

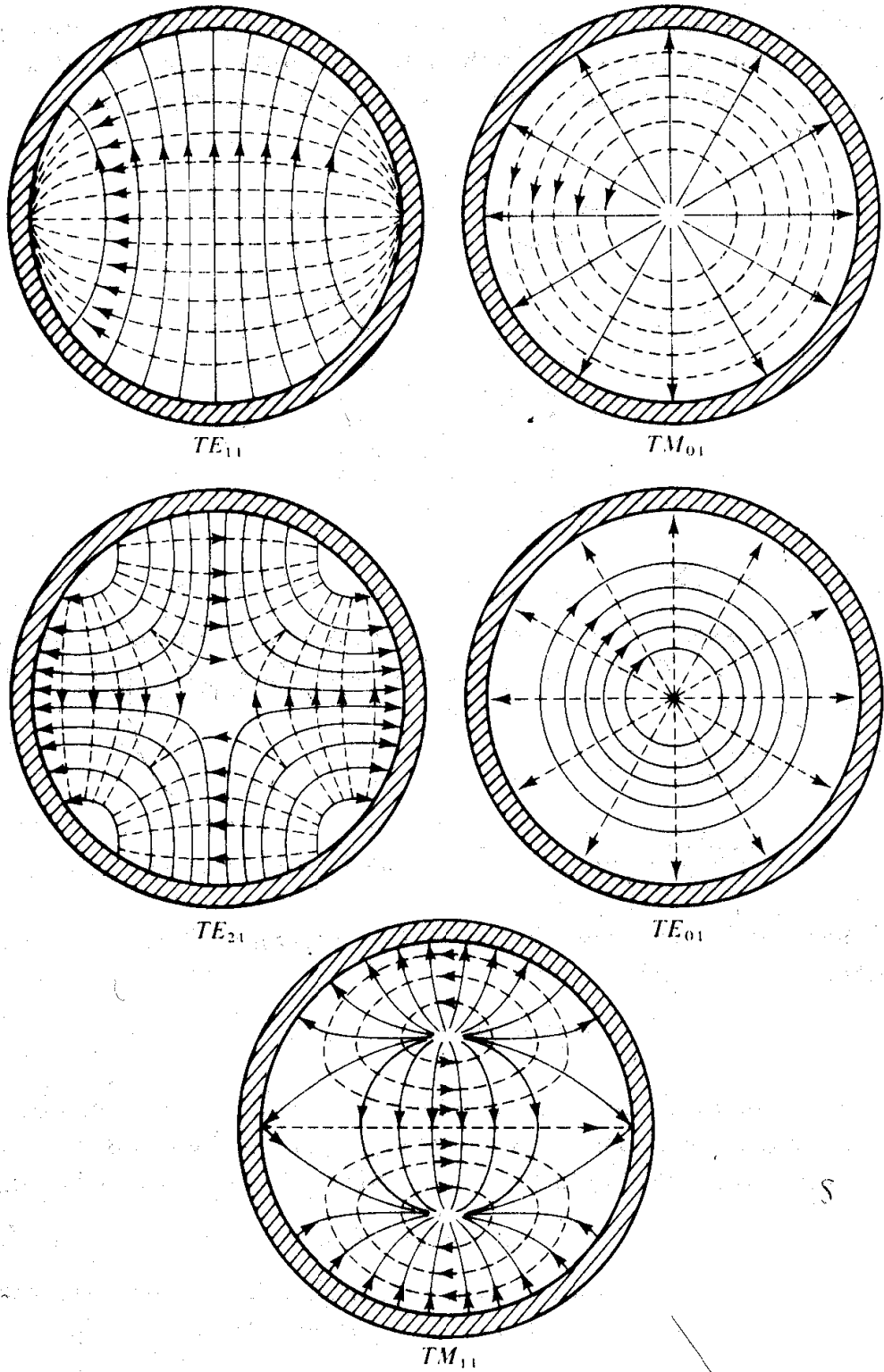


Figure 2.14. Modes in circular waveguide.



### **2.3.5 Circular Waveguide Mode Notation**

Figure 2.14 shows various field configurations for TE and TM modes in a circular waveguide. On the matter of notation, the indices for modes in the circular waveguide are as follows: the first indice ( $m$ ) is used to represent the total number of full-period variations of the radial component of the field along a circular path i.e. the number of times the wave goes through 0 to a maximum to 0 again, through a maximum and then returning to 0. The other indice ( $n$ ) represents the number of half-period variations of the azimuthal component along a radial path.

## **Chapter 3. Gyro-Device Theory**

## **Introduction**

The gyro-TWA (Gyrotron Travelling Wave Amplifier) is an untuned amplifier belonging to the gyrotron family, being based on the Cyclotron Resonance Maser (CRM) instability. In recent times, a breakthrough has been achieved in experiments exploiting helically corrugated interaction structures. Such structures give better interaction efficiency and thus make the devices desirable as broadband amplifiers with applications ranging from medical research (the LINear ACcelerator or LINAC), RADAR, and communications to plasma physics and industrial heating.

The following chapters contain details of the preliminary work undertaken with a view to designing, building, and experimentally testing the helically corrugated interaction structure for use with a cusp-type electron gun (also being designed at University of Strathclyde) in a novel gyro-TWA device. The device itself will operate with an electron beam of 150kV and 80A. Final power output from the gyro-TWA is planned to be approximately 3MW at around 10GHz (X-band). New numerical models were developed in order to study the linear and non-linear dynamics of the gain process were developed as a core objective of this thesis and are benchmarked against existing experimental results. It is therefore appropriate to review the background of the CRM instability.

In gyrodevices, the wavelength of operation is determined by the electron cyclotron maser condition, which in turn is set by the applied magnetic field. This requirement means that in order to have operation at higher frequencies, it is necessary to have a correspondingly high magnetic field strength. To ensure efficient coupling in a gyrodevice, it is necessary to have a high electron velocity component transverse to the direction of propagation to match the electric field of the electromagnetic wave. The transverse velocity component of the electrons spiralling due to the applied magnetic field interacts with the transverse electric or TE modes of a plain waveguide or interaction structure.

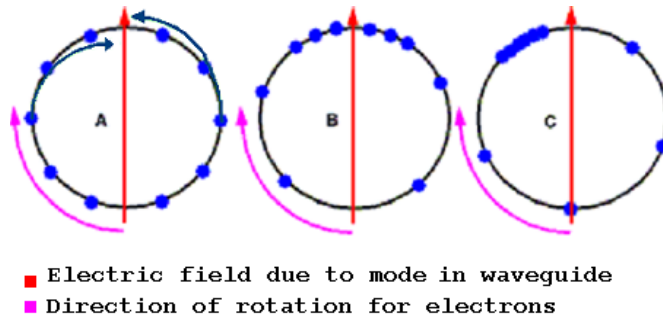


**Figure 3.1 CRM condition**

The operation of the gyrodevice family of microwave tubes is dependent on satisfying the cyclotron resonance condition. This can be explained briefly by referring to the diagram in Figure 3.1.

There are three main stages to be considered when understanding the CRM condition. Initially, electrons in the spiralling beam are distributed uniformly. Upon interaction with the TE modes within the interaction structure, the electrons velocities are modulated and a net exchange of energy may occur if we satisfy the resonance condition:

$$\omega' = n\omega_c \pm k_z v_z = n \frac{eB_0}{m\gamma} \pm k_z v_z \quad (3.1)$$

where  $\omega_c$  is the cyclotron frequency,  $\omega'$  is the wave frequency,  $k_z$  is the axial wavenumber of the electron,  $v_z$  is the axial velocity component of the electron,  $n$  is the  $n^{\text{th}}$  harmonic of the fundamental cyclotron frequency,  $e$  is the charge of an electron,  $B_0$  is the applied magnetic field,  $m$  is the rest mass of the electron and  $\gamma$  is the Lorentz-Fitzgerald factor ( $\gamma = 1 + \frac{eV}{mc^2}$ , where  $eV$  is the electron beam kinetic energy and  $mc^2$  is the rest energy). The term  $k_z v_z$  is known as the Doppler-shift term and is usually negligibly low in most gyrodevices and so their cyclotron frequency is equal to  $n$  times the fundamental cyclotron frequency.

This leads to phase-bunching of the electrons. This bunching can be explained as follows. Electrons with transverse velocity components in the opposite direction to that of the electric field will gain energy due to the increase in  $\gamma$  and thus their cyclotron frequency will decrease resulting in a retardation of their phase. Conversely, electrons with transverse velocity components in the same direction to that of the electric field will have a reduced  $\gamma$  and so their cyclotron frequency increases and their phase advances. After many RF cycles, the electrons which were originally in uniformly distributed positions become phase-bunched. By ensuring that the initial cyclotron frequency of the electrons is somewhat less than the rotational frequency of the electric field, a condition which is known as ‘de-tuning’, it is possible to ensure that the bunch forms in the decelerating phase for net energy transfer from the beam to the wave field to occur.

This interaction can also occur when operating with harmonics of the cyclotron frequency. Generally, when operating a gyrodevice at the  $n^{\text{th}}$  harmonic, one must ensure there is a multipole component of electric field somewhere of the order of  $2^n$ . When operating at these higher cyclotron harmonics, it is important to note that although there is a reduction in the magnetic field required for a specific operating frequency, the interaction becomes weaker i.e. increasing harmonic number decreases the strength of the interaction. This can lead to mode competition and increased losses within the device and for this reason it is usually undesirable to operate any higher than the second harmonic of the cyclotron frequency.

### **3.1 Physical Principles of the Gyro-TWA**

A gyro-TWA experiment couples an electron beam gyrating in a magnetic field in a waveguide with a resonant electromagnetic wave resulting in the onset of the cyclotron resonant maser (CRM) instability and a growth in microwave amplitude. Gain occurs when the Doppler shifted electron cyclotron frequency of the beam is close to and slightly less than the wave frequency.

Amplification of the electromagnetic wave is achieved via the azimuthal phase

bunching of the electrons in the electron beam. The basic operation of the device concerns electrons moving along helical trajectories within a waveguide in the presence of a uniform magnetic field  $\vec{H}_0 = H_0 \vec{z}_0$ .

### **3.2 Estimated Operating Efficiency of Gyro-TWA**

One may determine the upper limits to the efficiency of the Gyro-TWA by analyzing the mechanisms by which saturation can occur. There are two mechanisms which can lead to this saturation – free energy depletion, where the transverse kinetic energy of the electrons is depleted, or phase trapping, where sufficient energy has been removed from the electrons such that their mean cyclotron frequency has increased sufficiently that they move into accelerating phase with respect to the microwave field.

#### **3.2.1 Saturation due to Free Energy Depletion**

It has been documented that if the perpendicular component of the electron velocity,  $v_{\perp}$ , is too low then there are no growing solutions of the dispersion relation. In most practical cases it can be supposed that this critical value of  $\beta_{\perp}$  ( $=v_{\perp}/c$ ) is small. It is then possible to estimate the efficiency limit for the case where  $\beta_{\perp} \rightarrow 0$ .

The efficiency can be defined as

$$\eta = \frac{E_{KI} - E_{KF}}{E_{KI}} = \frac{\gamma_i - \gamma_f}{(\gamma_i - 1)} \quad (3.2)$$

where  $E_{KI}$  and  $E_{KF}$  are the initial and final kinetic energies of an electron in the beam respectively and  $\gamma$  is the Lorentz-Fitzgerald factor.

It can then be shown that the maximum efficiency of the device is limited by the expression

$$\eta = \frac{1 - \sqrt{\frac{1 + \alpha^2}{1 + \gamma_i^2 \alpha^2}}}{1 - \frac{1}{\gamma_i}} \quad (3.3)$$

where the pitch factor  $\alpha = \frac{v_{\perp}}{v_{\parallel}}$ .

Predicted efficiency of proposed gyro-TWA experiment  $\sim 60\%$  for  $\alpha$  of 1.1. In practice  $\beta_{\perp}$  is finite so this is probably an overestimate. It would also never be a practical saturation mechanism for high efficiencies and is only relevant where  $\beta_{\perp}$  is scarcely above critical, resulting in a ‘quasi-linear’ saturation with a very weakly perturbed electron distribution.

### **3.2.2 Saturation due to Phase Trapping**

The other saturation mechanism in the gyrotron is phase trapping. This is when sufficient energy is extracted from the beam that the electrons mean gyrofrequency increases above the wave frequency resulting in the electrons moving into accelerating phase with respect to the wave field and extracting energy back from the waveguide mode.

It can be shown that the single particle efficiency limit for phase trapping is given by the relation

$$\eta = \frac{-2 \frac{\Delta\omega}{\omega_{ci}} \gamma_i}{\left(1 - \frac{2\Delta\omega}{\omega_{ci}}\right) (\gamma_i - 1)} \quad (3.4)$$

where  $\Delta\omega$  is the detuning,  $\omega_{ci}$  is the initial electron cyclotron frequency, and  $\gamma_i$  is the Lorentz-Fitzgerald factor. Note that here we have assumed the detuning at phase trapping is reversed but of the same magnitude as the initial detuning.

Predicted efficiency for proposed gyro-TWA experiment  $\sim 38\%$  based on a detuning of 3%. This prediction must be considered as an overestimate though, as it completely neglects the multi-particle dynamics of the bunching phenomena.

### **3.2.3 Factors Influencing Practical Efficiency**

Conventionally gyro-TWAs employ a smooth cylindrical waveguide as the interaction structure which has some inherent problems. For greater bandwidth, it is usual to operate at grazing incidence where the beam dispersion overlaps with the wave, that is, where the axial electron velocity is close to the group velocity of the wave. When dealing with mildly relativistic electron energies (approximately 50-100keV), the intersection between the beam dispersion line and the curve representing the wave occurs at a point close to cut-off. Thus in the region of the amplification band where the axial wave number and group velocity are small, spurious gyrotron oscillations can easily be excited at the low-frequency boundary. At the high-frequency boundary of the amplification band, the axial wavenumber becomes relatively large and this leads to significant Doppler broadening of the cyclotron resonance line and hence a decrease in the efficiency of interaction due to spread in the axial electron velocity.

In situations where the device involves highly relativistic axial electron velocities, the region of grazing incidence is far from cut-off and hence the axial wave numbers in such systems are greater than those in the subrelativistic devices. Here, the Doppler frequency shift is extremely important and in this limit the gyro-TWA is the same as the cyclotron autoresonance maser (CARM)<sup>51,52</sup>. It should be noted that although this regime is desirable for the production of high-frequency radiation, it is extremely sensitive to electron velocity spread. This is due to the large wave group velocity which implies a large axial wavenumber.

Thus, the dispersion of the smooth cylindrical waveguide gyro-TWA is undesirable due to the increase in the sensitivity to axial velocity spread, which in turn reduces the interaction efficiency of the device. This factor all but ceased development of the



gyro-TWA until it was found that altering the geometry of the inner surface of the cylindrical waveguide could give an improved dispersion (refer to following section).

### **3.3 Ideal Dispersion Characteristics for the Gyro-TWA**

Using a smooth cylindrical waveguide in a gyro-TWA device results in a large wave group velocity only at a large axial wavenumber, which in turn causes velocity spread sensitivity to increase. This prevents them approaching the efficiency (~40%) usual in gyrotrons operating close to cut-off. Attempts to operate the system close to cut-off have been plagued by absolute instabilities and poor bandwidth due to the hyperbolic wave dispersion. The wave dispersion diagram for a conventional gyro-TWA is shown in Figure 3.2, with the interaction taking place where the lines for the wave and the electron beam intersect.

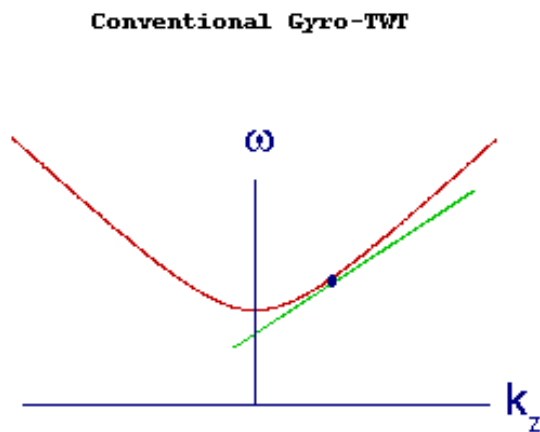


**Figure 3.2. Dispersion of conventional Gyro-TWA.**

The ideal wave dispersion for a gyro-TWA is shown in Figure 3.3 below.

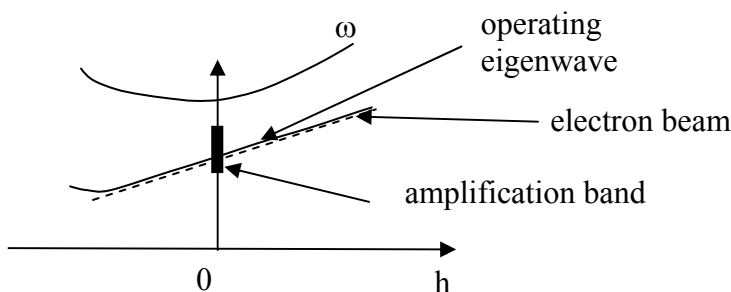


**Figure 3.3. Dispersion of waves for a gyro-TWA with a helically corrugated waveguide.**

Here the wave group velocity is sufficiently large and constant in the region of close-to-zero axial wavenumber. This dispersion may be achieved by the incorporation of a helical corrugation on the inner wall of an oversized cylindrical waveguide. In using an interaction structure with this configuration, several advantages over the conventional “smooth” bore are realised. These include improvements in stability to parasitic self-oscillations, frequency bandwidth and sensitivity to electron velocity spread.

### **3.4 Theory of the Helically Corrugated Waveguide - An Overview**

The geometry of the helically corrugated waveguide causes a radical change in the smooth waveguide dispersion for axial wavenumbers close to zero. This results in a significant increase in the group velocity of the eigenwave and the band over which the beam-wave interaction occurs. Two partial waves, with cut-off frequencies near and far below the operating frequency respectively, are coupled on the corrugations on the inner wall of the waveguide. The near cut-off partial wave undergoes a resonant interaction with the electrons in the beam while the addition of the second, far from cut-off partial wave acts to make the group velocity of the eigenwave zero. By careful adjustment of the parameters relating to the corrugation, it is possible to exhibit control over the group velocity of the eigenwave and thus one can match this to the axial velocity of an electron beam over a broad frequency range in the vicinity of the point where the axial wavenumber is equal to zero. Thus, use of this novel waveguide can achieve near-ideal dispersion characteristics for a gyro-TWA device. Refer to Section 4.2 for a more in-depth look at the theoretical background of the helically corrugated waveguide.

## **3.5 General Electron Beam Theory**

### **3.5.1 Introduction**

In the design of gyro-devices the beam geometry is of great importance. Here, a brief overview of the advantages and disadvantages of different beam geometries are presented, along with particular emphasis on the axis encircling Cusp gun which shall be used in the current gyro-TWA project. Also, operation in the temperature and space-charge limited regimes shall be discussed.

### **3.5.2 Beam Geometries**

#### **3.5.2.1 Axis Encircling ‘Pencil’ Beam**

This beam geometry is obtained when using a Pierce gun with a ‘kicker’ magnet section. The beam describes a helical path around the axis of the system. Collector heating can cause problems due to dissipation of the ‘pencil’ like beam on a small area of the collector. Also problematic for high duty cycle operation is the production of the required transverse magnetic field required to impart transverse velocity on the rectilinear beam from the accelerator. In practice phase mixing due to velocity spread means that in the interaction region this beam is very similar to the axis-encircling annular beam (refer to section 3.5.2.3).

#### **3.5.2.2 Non-Axis Encircling Thin Annulus Beam**

In the gyro-TWA, the beam must have a large component of electron velocity in the transverse direction for efficient interaction to occur, through the cyclotron resonance maser (CRM) instability, with the  $TE_{m,n}$  modes in the interaction region. The problem with non axis encircling annular beams is that the Larmor radius must be much less than the waveguide diameter meaning that one is restricted in beam voltage, pitch factor and harmonic operation. Furthermore mode selectivity is very poor due to the guiding centres of the electron orbits not being on the axis of the waveguide. Expanding the fields around an off-centre beam guide radius shows that

all modes have weak high order field components leading to complex mode competition.

A major advantage of this type of beam geometry is easy control of the electron beam current due to the diode being entirely magnetically confined, plus uniform dissipation of the beam on the collector. Beam current control by cathode temperature is possible, however it is then necessary to operate the cathode in the temperature limited regime in all cases and so this can lead to manufacturing problems relating to the uniformity of the emission surfaces.

### **3.5.2.3 Axis Encircling Annular Beam**

This beam geometry is obtained by using a Cusp gun which has some important benefits. Mode selection is greatly improved over the non-axis encircling annular configuration because only those modes for which the azimuthal indexes are equal to the cyclotron harmonic number can participate in the interaction. This is due to the fact that the Fourier expansion is performed around the guiding centre. For the case of the axis-encircling beam this guiding centre is also the waveguide centre. Therefore the expansion is simple and we have only the  $TE_{n,q}$  modes present with  $2^n$  polar structures in their fields. As the cusp itself gives the electrons in the beam their transverse velocity, there is no need for a kicker and so the size and weight is also reduced. The main advantage lies in the fact that one can use high voltage for operation at the second harmonic because the resulting larger radius is tolerable. Dissipation of the beam is much less problematic than with the ‘pencil’ type axis encircling beam as the power of the beam is dissipated over a much larger area of the collector and it is also possible to scan the beam across the z-axis in order to regulate heating.

It should be noted here that, from an electrodynamic perspective, the RF interaction for realistic beams is identical for the two axis-encircling schemes since phase mixing in realizable beam geometries leads to a very similar configuration.

#### **3.5.2.4 Operating Regime**

For the gyro-TWA experiment, it is most desirable to operate in the temperature-limited regime as opposed to the space-charge limited one. Although operation in the space-charge limited regime is more tolerant of emitter surface uniformity variations, control of the electron beam current is difficult. However, operation in the temperature-limited regime allows the control of the beam current without interfering with other important parameters. For the same reason, it is preferable to use a confined flow as opposed to Brillouin flow as the confined flow method of focussing is relatively insensitive to beam space charge and self-field, allowing adjustment of the beam current density without severely impacting the electron beam quality.

## **Chapter 4. Methods & Apparatus**

## **4.1 Introduction**

In order to minimize the need for re-machining and the alteration of experimental design, it is greatly advantageous to numerically and mathematically model the experimental components. For the gyro-TWA experiment here, it is of particular help as its use can allow the prediction of dispersion characteristics for the helically corrugated waveguide employed as the interaction structure and can also give some indication of the stability to oscillations, gain etc. of the gyro-TWA configuration as a whole.

In this section, a novel method for numerical modeling using the PIC (Particle In Cell) code MAGIC<sup>53,54</sup> is described for calculation of the helically corrugated waveguide dispersion characteristics and the gyro-TWA gain and stability to oscillations etc. Also, a new code is presented which allows the calculation of the small signal linear gain of the gyro-TWA using the mathematical software MAPLE. Together with a method for numerical solution of perturbation theory, these various codes combine to form a complete software modelling suite for determining key experimental parameters before any of the apparatus is machined.

## **4.2 Perturbation Theory**

The helical interaction structure consists of a cylindrical section of waveguide modified by a helical corrugation on the inner surface as shown in Figure 4.1



**Figure 4.1 Helically corrugated waveguide.**

The inner surface of the helically corrugated waveguide can be represented in cylindrical coordinates  $r, \varphi, z$  as follows:

$$r(\varphi, z) = a_0 + a_1 \cos(\bar{m}\varphi - \bar{h}z) \quad (4.1)$$

where  $a_0$  is the mean radius of the waveguide, and  $a_1, \bar{m}$  and  $\bar{h} = 2\pi/d$  are the amplitude, azimuthal and axial numbers of the corrugation, respectively, and  $d$  is the corrugation period. In order to achieve the desired dispersion, the corrugation has to couple two partial rotating waves of a waveguide with a radius of  $r_0$ ; one partial wave is near-cut-off, mode (A), and has a small axial wavenumber,  $h_A \ll k$ , where  $k = \omega/c$ , while the other partial wave, a travelling wave (B), has a large axial wavenumber,  $h_B \sim k$ .

These conditions are met when the azimuthal indices and axial wavenumbers of the waves and the corrugation satisfy the Bragg conditions

$$m_A + m_B = \bar{m}, \quad \bar{h} \approx k_B \quad (4.2)$$

where  $m_A$  and  $m_B$  are the azimuthal numbers of the waves. The resonant coupling of the waves corresponds to the intersection of their dispersion curves on the dispersion diagram shown in Figure 4.2 or more exactly to the intersection between mode A, with cut-off frequency  $\omega_0$ , and the first spatial harmonic of mode B, with cut-off frequency  $\omega_{0B}$

For the desired dispersion they are mode A,  $\vec{E} = \vec{E}_A(\mathbf{r})(a_+ e^{-ik_A z} + a_- e^{ik_A z}) e^{i(\omega t - m_A \varphi)}$  and the first spatial harmonic of wave B,  $\vec{E} = \vec{E}_{B1}(\mathbf{r}) b e^{-ik_{B1} z} e^{i(\omega t + m_B \varphi)}$  where  $k_{B1} = k_B - \bar{k}$ . For the case where the corrugation depth is negligibly small, these modes satisfy the following unperturbed dispersion equations:



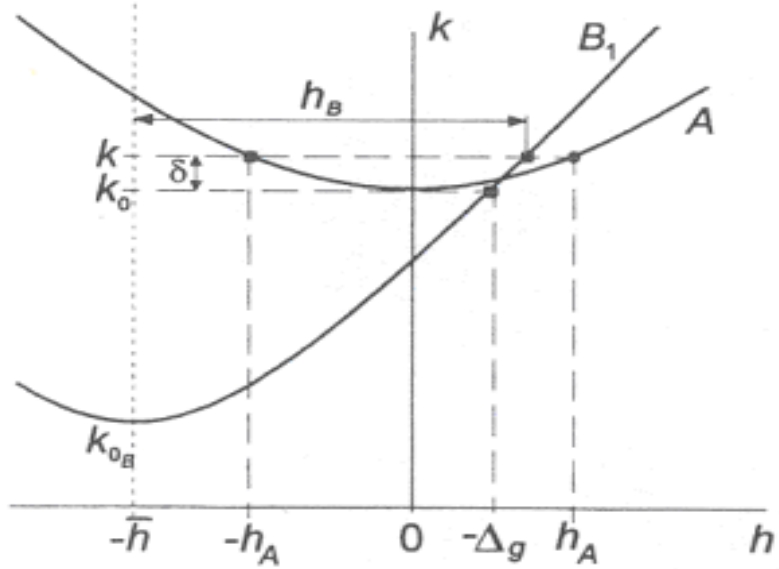


**Figure 4.2 Parameters of the partial waves to be coupled by the corrugation.**

$$k^2 - k_0^2 - k_A^2 = 0$$

$$k^2 - k_{0B}^2 - (k_{B1} + \bar{h})^2 = 0 \quad (4.3)$$

where  $k_0$  and  $k_{0B}$  are wavenumbers corresponding to the cut-off frequencies of modes A and B.

The corrugation depth of the helix is defined as the depth of the ridges into the inner surface of the oversized cylindrical waveguide. If the corrugation amplitude,  $a_1$ , of the helix is small when compared to the wavelength and mean radius, then it is possible to approximate the field structure and dispersion characteristics of the interaction structure using perturbation theory. Thus, the eigenwaves which result from the coupling of the partial waves A and B can be found. By putting the eigenwaves in the form  $e^{-ik_z z}$  we obtain the dispersion equation

$$\left( \frac{\omega^2}{c^2} - (k_z + \bar{h})^2 - \left( \frac{s_B}{r_0} \right)^2 \right) \left( \frac{\omega^2}{c^2} - k_z^2 - \left( \frac{s_A}{r_0} \right)^2 \right) = 4\sigma^2 k_0^4 \quad (4.4)$$

where  $s_B$  and  $s_A$  are the roots of the associated differentiated Bessel functions for the modes A and B in smooth waveguide,  $\omega_0$  is the cut-off frequency of the partial wave

A, and  $\sigma$  is the coupling coefficient which describes the coupling between the A and B modes found by using the method of fictitious currents.

Equation 4.4 has four roots and can be reduced to a quadratic equation in ' $\omega^2$ ' by setting the coupling coefficient equal to

$$\sigma = 0.5 * \left( S_B^2 * S_A^2 + 2 * a_0^2 * \left( \left( \frac{S_B}{a_0} \right)^2 + \bar{h} * h_B \right) \right) / \left( \sqrt{(S_B^2 - 1)} * \sqrt{(S_A^2 - 4)} \right) * (a_1 / a_0^3)$$

$$\text{Where } h_B = 0.5 * \left( \left( \frac{S_A}{a_0} \right)^2 - \left( \frac{S_B}{a_0} \right)^2 + \bar{h}^2 \right) / \bar{h},$$

The solution of the quadratic equation is then trivial and a Microsoft Excel spreadsheet was created to perform this. Previous research has shown that  $\sigma > 1.3$  perturbation theory becomes inaccurate. Thus care must be taken not to apply this theory to deeper grooved waveguides.

Thus the key reason for the use of a cylindrical waveguide with a helical corrugation on the inner wall lies in the fact that the smooth waveguide dispersion is substantially altered in the region of close-to-zero longitudinal wavenumbers. This results in an increase in the group velocity of the eigenwave. By altering the geometrical parameters of the corrugation, it is possible to control the eigenwave group velocity and to adjust it to the longitudinal velocity of an electron beam for a broad frequency band in the region where the longitudinal wavenumber is close to zero.

It is important to note that the dispersion of rotating waves in a helically corrugated waveguide is strongly dependent on the direction of their rotation. Injecting a TE<sub>11</sub> mode into the waveguide, the dispersion of waves co-rotating with the helix is practically unperturbed while the dispersion of waves counter rotating with respect to the helix is significantly modified. The TE<sub>11</sub> mode counter-rotating with the helix couples to the co-rotating TE<sub>21</sub> mode on a three-fold helix.

### **4.3 Linear Theory**

The gain of an amplifier is obviously an important characterizing parameter<sup>55</sup>. Both

saturated and small signal linear gain can be measured by experimental means and also predicted by way of numerical simulation.

In order to predict the linear gain of the gyro-TWA experiment a MAPLE code was written which would allow the input of the helically corrugated waveguide and electron beam parameters in order to obtain the linear gain characteristics of the chosen system. The code solves the following fifth order dispersion equation for the gyro-TWA

$$\begin{aligned} & \left[ (k_w^2 - 2\delta)(k_w + \Delta_g - \delta/h_0) - 2\sigma^2/h_0 \right] [k_w - (\delta - \Delta_H)/\beta_{H_0}]^2 = \\ & C^3 (k_w + \Delta_g - \delta/h_0) \left( 1 + \frac{2s\beta_{H_0}}{\beta_{\perp_0}^2} [k_w - (\delta - \Delta_H)/\beta_{H_0}] \right) \end{aligned} \quad (4.5)$$

where  $k_w$  is the axial wavenumber attributed to the coupled waves,  $\delta = k - k_0$  is the frequency mismatch,  $\bar{h}$  is the axial wavevector of the corrugation,  $h_0$  is the propagation wavevector of the travelling mode at the cut-off of the non-propagating mode,  $\Delta_g = \bar{h} - h_0$  is the geometrical mismatch between the axial geometry and this propagation wavevector,  $\sigma$  is the coupling coefficient (determined by the corrugation depth of the helically corrugated waveguide, the nature of the helix structure and modes being coupled),  $\Delta_H = (s\omega_{ce} - \omega_0)/\omega_0$  is the magnetic field mismatch where  $s$  is the harmonic number and  $\omega_{ce}$  is the cyclotron frequency,

$$\beta = \sqrt{1 - \frac{1}{\gamma^2}}, \quad \beta_{H_0} = \sqrt{\frac{\beta^2}{1 + \alpha^2}}, \quad \beta_{\perp_0} = \beta^2 - \beta_{H_0}^2.$$

$C$  - known as the Pierce parameter is given by

$$C = \left( \frac{4\bar{I}\rho^2}{\gamma_0 N_A \beta_{H_0}} \right) \quad (4.6)$$

where  $\bar{I} = eI/mc^3$  where all terms have the usual meanings,

$\rho = \frac{\beta_{\perp 0}}{\beta_{\parallel 0}} J'_s(s\beta_{\perp 0}) J_{m_A-s}(\hat{r}_g)$  is the cyclotron mismatch for the system where J refers to

Bessel functions and the indices  $m_A$  and  $s$  refer to the azimuthal index of the near cut-off mode and the harmonic number respectively, and  $\hat{r}_g = k_0 r_g$  where  $r_g$  is the guiding centre radius of the electron beam (in the case of an axis-encircling beam this reduces to zero).

The parameter  $N_A = J_{m_A}^2(v)(v^2 - m_A^2)$  is the dimensionless norm of mode A with  $v = k_0 a_0$ . It should be noted here that all parameters were normalized to  $k_0$ .

This equation (Equation 4.5) was solved by MAPLE using the FSOLVE function which uses Newton's method (also known as the Newton–Raphson method) when the argument range is given, e.g. fsolve (f(x), x=Lower..Upper). This method works by finding successively better approximations to the zeroes (or roots) of a real-valued function. Upon solving this equation, the real and imaginary solutions were written to text files so that they could be easily imported to MS Excel. As the equation was solved for a range of delta, the results produced were a list of delta values with their corresponding  $k_z$ . An Excel spreadsheet was then made to process the imaginary solutions which are of interest in this case by converting certain normalized parameters to real quantities and calculation of the gain using the expressions

$$E \sim E_1 e^{ik_z z} \sim E_1 e^{ik_r r} e^{k_i z} \quad (4.7)$$

where  $k_z = k_r - ik_i$

where E is the electric field,  $k_z$  is the axial wavenumber and z is the length of the system.

Since

$$G = 20 \log_{10} \frac{E}{E_1} = 20 \log_{10} e^{k_i z} = 20 k_i z \log_{10} e \quad (4.8)$$

where  $G$  = gain (in this case linear gain) and  $Z$  is the length of the system. Note also that  $k_i$  denotes the imaginary part of  $k_z$ .

The prediction of the linear gain coefficient of a specified helically corrugated waveguide and electron beam configuration is of the utmost importance in the design of the gyro-TWA experiment. As the main electron beam parameters would also to be predicted using this code, it would facilitate greater efficiency in manufacturing process and reduce costs considerably by refining key experimental parameters prior to the experiments assembly.

#### **4.4 Overview of MAGIC PIC code**

MAGIC is an electromagnetic particle-in-cell code and uses a finite-difference, time-dependent method for simulation of processes that involve electromagnetic fields and charged particles. In order to obtain the electromagnetic fields for a given system, the full set of Maxwell's equations are solved in conjunction with the Lorentz force equations and the relativistic equations of particle motion. By solving Maxwell's time-dependent equations, the evaluation of the electromagnetic fields associated with the current and charge distributions of the simulated physical processes occurring within the system may be obtained. Also, the Lorentz equations and the equations of motion determine the impact of the fields on the currents and charges. Thus it is possible to simulate the interaction between charged particles and electromagnetic fields.

#### **4.5 MAGIC Simulation for Determining Dispersion of Helix**

In order to achieve coupling between the electron beam and the eigenwave, it is necessary to have knowledge of the dispersion properties of the helically corrugated waveguide. If the corrugation amplitude is small compared to the wavevector then the method of perturbations described in Chapter 4 can be used to calculate the dispersion characteristics, however for a deep grooved waveguide a numerical approach using the 3D finite-difference time-domain code MAGIC is adopted.

By finding the angle of rotation of a linearly polarised  $TE_{11}$  mode caused by the helix, it is possible to obtain the dispersion characteristics for the system (refer to Chapter 4 for differential impact on rotating components). This was achieved by using the MAGIC code to simulate the injection of a linearly polarised amplitude modulated pulse of 6.5GHz bandwidth into the helix (refer to Appendix A for the code used in this simulation). In order to obtain the correct time profile for the pulse, an inverse Fourier transform was performed on a square spectral profile from 6 to 12.5 GHz. The linearly polarised  $TE_{11}$  mode was then injected into the helix, which causes the polarisation to rotate due to differential dispersion for the two circularly polarized components of the linearly polarized wave. When these are subsequently recombined in a smooth bore receiving section, the resulting linearly polarized wave has a different polarization angle compared to the launched wave. The geometry of this simulation is shown in Figure 4.3 below.

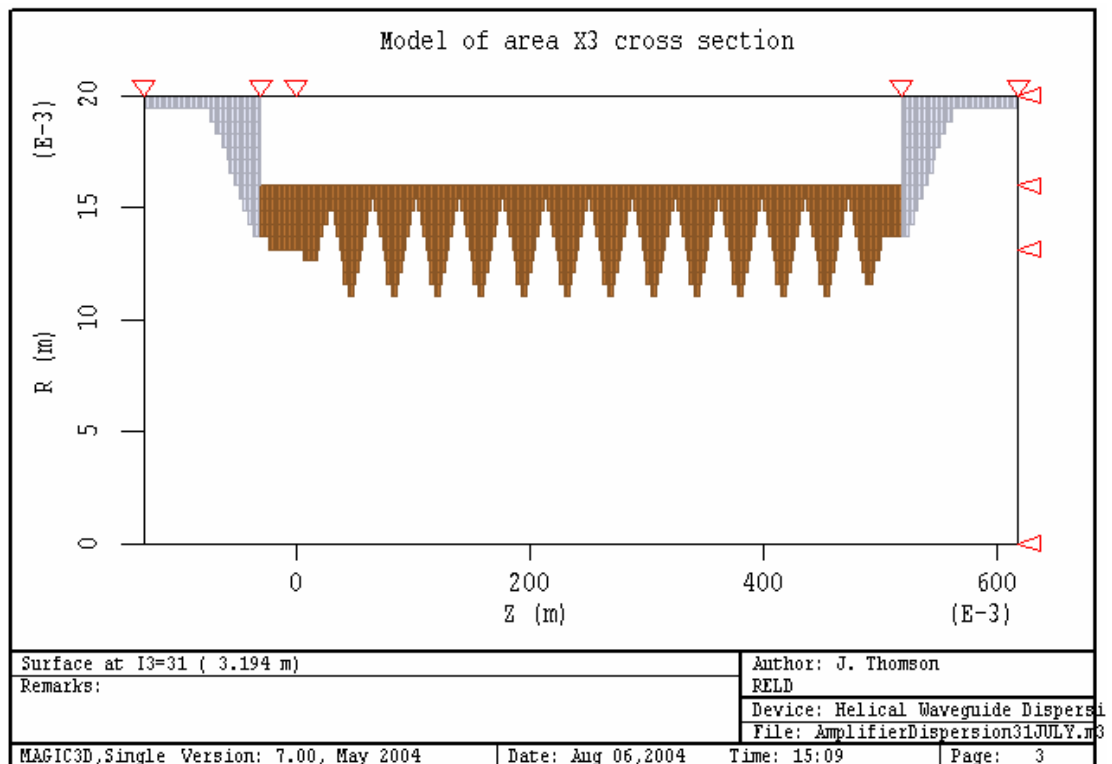


**Figure 4.3 MAGIC simulation for the measurement of helix dispersion.**

The larger diameter waveguide horns at both the input and output of the simulation should be noted. These had to be implemented due to the MAGIC codes dependence on there being a single phase velocity at any input or output plane. By addition of these large diameter sections with tapers, the phase velocities would tend to  $c$  and so would be approximately equal and independent of frequency at both ends of the simulation.

As has been mentioned previously, the wave rotating with the helix is approximately unperturbed while the wave rotating against the helix is coupled to the  $TE_{21}$  mode. The radial electric field at the output of the helix was then measured and a Fourier transform performed on the electric field as it varies with time along polarisations parallel and perpendicular to the initial polarisation. When plotted on a log scale, the frequencies that coincide with the minima correspond to a wave polarisation perpendicular to measurement polarisation at the output of the helix. These correspond to a phase difference of the two rotating components of  $(2n + 1)\pi$   $n \in Z$  for polarizations perpendicular to the initial polarizations and  $2n\pi$   $n \in Z$  for polarizations which are parallel to the initial polarizations. By measuring the frequency at each of these spikes it was then possible to find the change in axial wavenumber due to the corrugation and hence plot the dispersion for the helically corrugated interaction structure.

#### **4.6 MAGIC Simulation for Modelling of Gyro-TWA**

In order to successfully model the gyro-TWA using a numerical PIC code such as MAGIC, it is imperative to ensure that the geometry is accurately modelled in accordance with the geometry to be used in the physical experiment itself. Also, and equally critically, once the geometry is input the resolution must be set such that the electrons in the code ‘see’ the interaction structure properly and that no resolution-dependent effects degrade the results.

The initial step of designing the code in MAGIC is to input the desired geometry to

the code, this is achieved by co-ordinate based commands using a cylindrical or polar co-ordinate system. Once the geometry is defined, it is necessary to set a suitable resolution for the Finite Difference mesh which in the first instance should be a compromise between low running time for the code and accuracy of the final result. There were, however, some other factors to be taken into consideration when the resolution settings were chosen for the simulation. One of the most important factors in the system geometry are the corrugations which make the helically corrugated waveguide unique. In order that the radiation properly ‘sees’ these corrugations, it is of the utmost importance that there is adequate resolution in the  $r$  plane. These corrugations in this case are of the order of a few mm so the radial resolution setting must reflect this. The only concern in the  $Z$  plane is the wavelength of the propagating wave so as long as the axial resolution is reasonably defined with respect to the wave then no problems pertaining to grid density should exist. In the azimuthal plane,  $\emptyset$ , it was most important to consider resolutions which would facilitate the propagation of modes with the required azimuthal indices.

It is most important is to ensure that the code employs enough cells at transitions in the inner surface topology of the geometry as sharp transitions can cause impedance mismatch problems. In MAGIC, all systems must be enclosed and this is achieved by the used of the PORT command. PORTs are lines or planes which are used to ‘cap’ ends of the simulation. It is also possible to monitor diagnostics across these. One key factor in the application of these PORTs is that a PORT can be either POSITIVE or NEGATIVE.

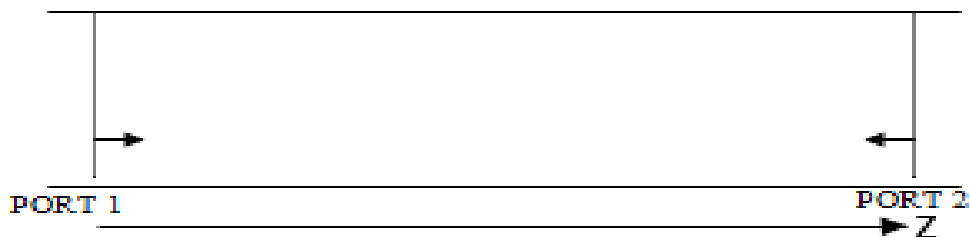


**Figure 4.4 Diagram illustrating directions of PORTs.**

This can be illustrated in Figure 4.4 above. The alignment of the PORTS is always termed from outside the perimeter of the system to the inside. Thus PORT 1 is



assigned the POSTIVE alignment and PORT 2 the NEGATIVE alignment. These alignments are so named because coming from the outside of the simulation geometry to the inside is an increase in z co-ordinate and thus we have a POSITIVE PORT 1 and vice-verse for PORT 2. PORTS can also be used as injection points for either an electron beam or radiation. However, problems were found when trying to introduce both an electromagnetic wave and an electron beam to the system in order for interaction to take place. Various configurations were tested. The first of these is shown overleaf in Figure 4.5.

This arrangement was found to produce strange non-physical effects, whereby the electron beam would briefly reverse in direction towards the port and then continue on in the intended direction. The output of the simulation also indicated that non-physical beam-wave interaction was taking place. Whilst the electron beam itself appeared to be sensible enough, these strange effects and the fact that they could not be explained was clearly undesirable and so a better configuration had to be designed.

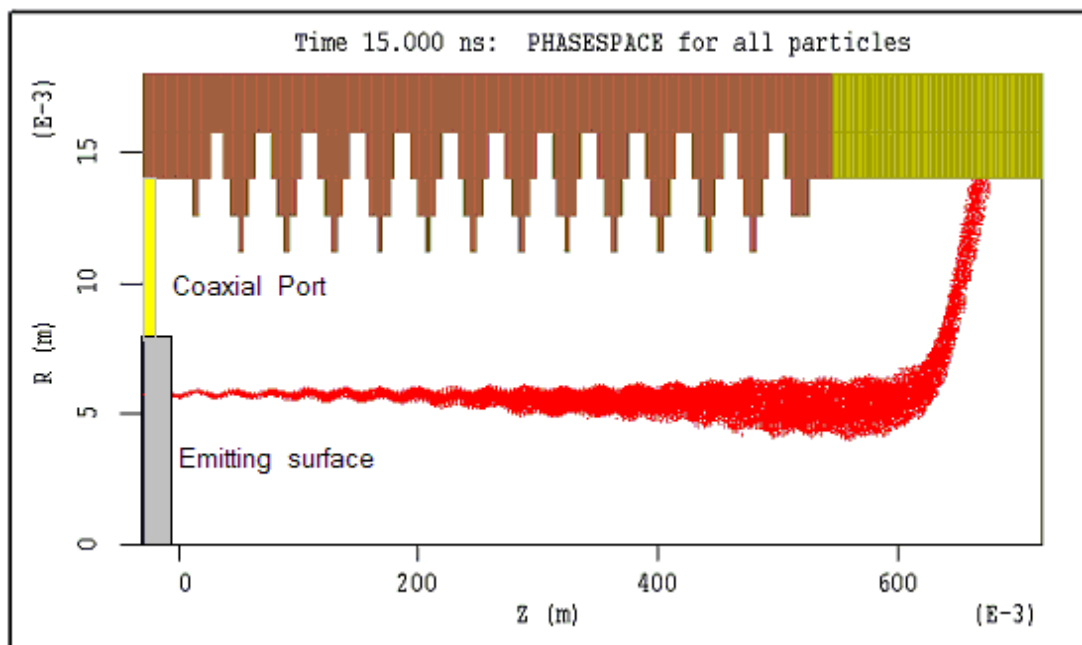


**Figure 4.5 Coaxial port configuration for MAGIC gyro-TWA simulation.**

However, it was found that this particular arrangement gave way to unclear or distorted mode patterns at the output. It was found that as this was an attempt to inject a TEM mode in the co-axial section between the emitter and the waveguide and thus excite the  $TE_{11}$ , this geometry configuration caused poor overlap of integrals and hence no coupling could occur. Another possible configuration was the inclusion of a dielectric emitting surface with permittivity set to the permittivity of free space with a port positioned behind it to input the radiation i.e. a ‘phantom’ area for the emitting surface. An option was defined for the dielectric that prevented it accumulating charge. This arrangement is shown below in Figure 4.6.

After some research of the available methods for injecting radiation and electron beams into a MAGIC simulation, it was decided that possibly the best way to tackle this particular problem would be to use MAGIC’s ‘IMPORT’ and ‘EXPORT’ commands. This facility allows one to ‘EXPORT’ data files containing particle and field data of an electron beam passing through a PORT.

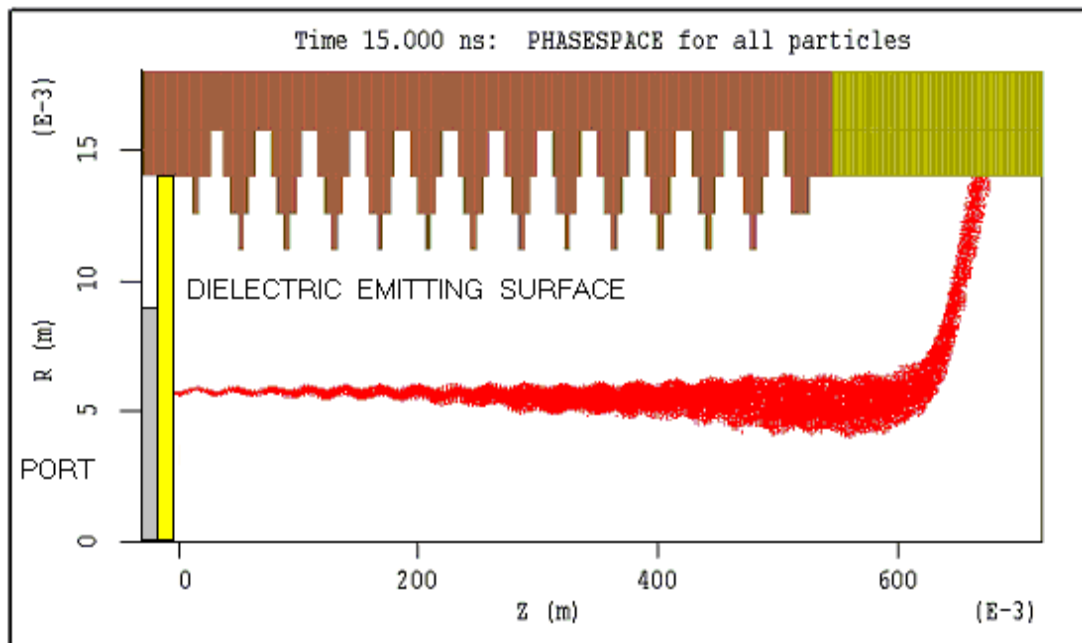


**Figure 4.6 Dielectric emitting surface with emitting port behind it.**

It is then possible to ‘IMPORT’ this beam into a separate simulation. The electron

beam emission section of the gyro-TWA code (see Appendix A) was removed and then a separate code was written to simulate a beam travelling through a smooth bore tube with the same dimensions and gridding as the input waveguide in the main gyro-TWA simulation. In this code the ‘EXPORT’ command was used in order to save field and particle data files for the electron beam. Particular care had to be taken at this point to ensure that the field and particle trajectory information produced by the EXPORT code was as accurate as possible. It was ensured that the plane circular waveguide used in the code was of the same radius as the electron beam injection point in the main simulation. It was also found that it was important to set the run time of the EXPORT code sufficiently long enough. Failure to do this caused discontinuities in the electron beam when running the main simulation for longer durations.

These files were then imported into the main simulation at a plane transverse to the z-axis and, by using MAGIC’s ‘DRIVER’ function to input the radiation it was found that the beam-wave interaction could be simulated.

Various diagnostics were set up in the code in order to measure key parameters. In order to measure the magnetic field profile, MAGIC’s ‘range’ command was used. This produced a plot of the axial component of the magnetic field in space and was used to ensure the electron beam travelled a sufficient distance along the interaction structure. Commands were also used to measure the beam current on the anode and the code would obtain the output power by measuring the Poynting’s flux through the output port. Thus, the gain could be found by knowing the input driving power and obtaining this measurement of output power. In order to make frequency measurements, a diagnostic was setup within the code to calculate the Fourier Transform of the electric field.

#### **4.7 Design of the Helically Corrugated Waveguide for use in the Gyro-TWA**

In most cases, the final design of the helically corrugated waveguide is greatly determined by the final electron beam design for use in the system. In order for

interaction between the mode of operation and the electron beam, it is essential to match such parameters as the confining magnetic field (B), voltage (V), current (I) and also pitch factor ( $\alpha$ ). The first stage of any helix design is to obtain plots of the helix dispersion superimposed on the electron beam dispersion using perturbation theory. A spreadsheet was constructed utilizing the Excel software which would allow both the plotting of these dispersions and also the alteration of important helix and beam parameters. By careful adjustment of the helix mean diameter  $a_0$ , corrugation depth  $a_1$ , and the periodicity of corrugations, it is possible to match the gradient of the dispersions over some range – it is at this point that the main interaction will occur. This is shown in Figure 4.7, which illustrates how the analytical method for obtaining the dispersion characteristics using perturbation theory can be used along with electron beam parameters to match the gradient of the two curves.

As was previously stated in Chapter 3, in order to avoid problematic oscillations and Doppler broadening it is desirable to utilize the helically corrugated structure in order that we have a sufficiently large wave group velocity ( $v_g$ ) in the region of close-to-zero axial wavenumber.

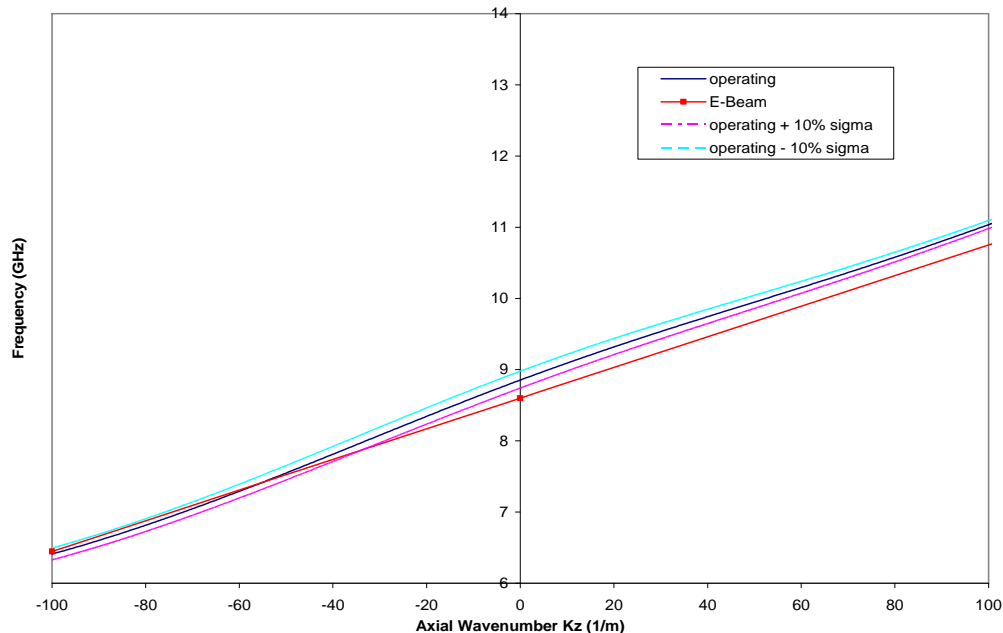


**Figure 4.7 Illustration of how the gradients of dispersions of both the electron beam and helically corrugated waveguide can be matched using a numerical method to solve the perturbation theory-derived coupled dispersion relation.**

After finding the approximate design parameters via these plots, the helix geometry was input to the MAGIC code designed to measure the dispersion characteristics. This simulation gave a more accurate prediction of the helix dispersion characteristics.

The next stage in the design of the helix was to input the design parameters into a MAGIC code created to simulate the gyro-TWA experiment i.e. a simulation incorporating an axis-encircling beam and the helix geometry, along with input radiation. By configuring the code to run with beam and helix parameters previously estimated, it was possible to obtain predictions of gain, bandwidth, stability to oscillations etc. These results (as well as the dispersion characteristics from perturbation theory and from the MAGIC simulation for a previous experiment) are presented in the subsequent chapters, and their accuracy compared to the experimental data.

#### **4.8 Experimental Apparatus**

As the purpose of this thesis was to design a helically corrugated waveguide for use in a gyro-TWA experiment utilizing an axis-encircling beam configuration as its electron beam source, it is helpful to summarise the experimental setup against which the codes were benchmarked. In the following section, the components of the gyro-TWA experiment used as the benchmark test for this suite of codes will be briefly described and the construction of the experiment itself discussed. The basic configuration of the gyro-TWA is shown below in Figure 4.8.

The electron beam was generated by electrons emitted from the surface of the electron gun assembly. The electron beam then traveled through the drift tube, focused by a B field generated by the magnet coils (in this case the B field was 0.21 T). These electrons were then ‘kicked’ or given a transverse velocity component by a magnetic field coil known as the ‘kicker’ coil.

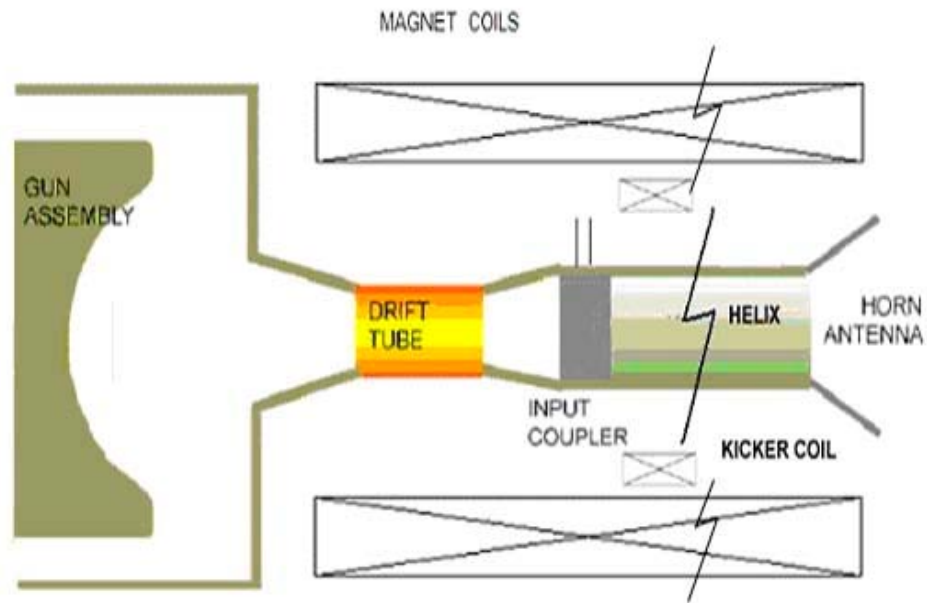


**Figure 4.8 Configuration of gyro-TWA experiment.**

Thus, the beam became axis-encircling. From here the beam passes through the helically corrugated waveguide where the input coupler was used to input  $TE_{11}$  radiation. As has been previously discussed, conventional smooth-bore waveguides are undesirable for use in gyro-TWA experiments as they are plagued by parasitic oscillations and Doppler broadening problems. In order to gain a near-ideal dispersion a waveguide featuring a helically corrugated inner surface was employed. The parameters of the helix used in this experiment were:

$$a_0 = 1.41 \text{ cm}$$

$$a_1 = 0.22 \text{ cm}$$

$$d = 3.9 \text{ cm}$$

This waveguide facilitated the interaction between the electron beam and the microwave radiation and thus microwave radiation amplification. This radiation was measured in free space beyond the output horn antenna. A range of diagnostics was used in order to monitor or measure important experimental parameters. Electron

beam current was measured using a Rogowski coil, a type of coil which can be used as a passive current sensor. The beam voltage was measured using a voltage divider, a configuration which allows the measurement of large voltages. Gain and power measurements were made by calibrated attenuators and rectifying diodes and frequency measurements by a cut-off filter.

#### **4.8.1 Elliptical Convertors**

Elliptically deformed waveguide polarisers were used in order to ensure that the entire wave was in the operating eigenmode. These polarisers circularly polarize the wave before it enters the helically corrugated waveguide.

A wave is said to be left or right circularly polarized if the transverse electric field components can be represented by the following equations

$$\underline{E}_{left} = E_0 (\vec{e}_y \cos(k_{z1}z - \omega t) - \vec{e}_x \sin(k_{z2}z - \omega t)) \quad (4.8)$$

or

$$\underline{E}_{right} = E_0 (\vec{e}_y \cos(k_{z1}z - \omega t) + \vec{e}_x \sin(k_{z2}z - \omega t)) \quad (4.9)$$

where  $E_0$  represents the electric field amplitude and  $\vec{e}_y$  and  $\vec{e}_x$  are unit vectors.

It is possible to represent the linear polarized wave with the following expression

$$E_{lin} = E_0 (\vec{e}_x \pm \vec{e}_y) \cos(k_z z - \omega t) \text{ or}$$

$$E_{lin} = E_0 (\vec{e}_x \pm \vec{e}_y) \sin(k_z z - \omega t) \quad (4.10)$$

Linearly polarized radiation consists of two circularly polarised components of equal amplitude. As the perpendicular components of the electric field vector are in phase, the vector sum of these components is constant.

By taking linearly polarized radiation and adjusting the geometry of the polarizer to make two perpendicular components  $\pi$  out of phase, then when one component is at its maximum or minimum electric field, the other component is at zero. The resulting field configuration is known as circularly polarized radiation.

#### **4.8.2 Vector Network Analyser**

The VNA is an instrument which allows the accurate measurement of change of electrical wave amplitude and phase from a reference point. This provides a means by which to measure the dispersion of the helically corrugated interaction structure.

A vector network analyzer, or VNA, is an instrument which measures the complex transmission and reflection characteristics of two-port devices in the frequency domain. It does this by sampling the incident signal, separating the transmitted and reflected waves, and then performing ratio measurements that are directly related to the reflection and transmission coefficients of the two-port device being investigated. Frequency is swept to rapidly obtain amplitude and phase information over a band of frequencies of interest.

The s-parameter representation is the most common format used to represent VNA measurements. The s-parameters  $S_{11}$  and  $S_{21}$  can be interpreted as the input reflection coefficient and forward transfer coefficient (gain or loss). Likewise  $S_{22}$  and  $S_{12}$  can be interpreted as the output reflection coefficient and reverse transfer coefficient (gain or loss).

Prior to the development of the VNA method of dispersion measurements presented here, an SNA (or Scalar Network Analyser) was used in order to measure dispersion characteristics of the helically corrugated waveguide. Unfortunately, the SNA approach possessed some inherent problems. Primarily, it was only able to measure amplitude of the signal. As calculation of the dispersion was greatly dependent on the number of whole rotations of the mode (or  $n$ ), to achieve reasonable



measurements it was necessary to use many periods of helically corrugated waveguide (often of the order of a metre or so) to obtain a sufficient number of measurement points. This meant that measuring with the SNA took much more time, cost more (as long waveguide sections had to be machined for testing), and also due to the long length it was difficult to determine the value of the integer  $n$ . As the VNA was capable of phase measurement also, this meant that there were more points of measurement for a given length of helix. This made it easier to estimate the value of  $n$  (difference between  $n=2$  and  $n=3$  – as in VNA - would be obvious compared with the difference between  $n=20$  and  $n=21$  – as in the SNA). Thus, it was possible to use a shorter section of helix for measurement, which reduced time and also saved considerably on machining costs.

Calibration is necessary to correct for cable losses, to correct for non- $Z_0$  conditions, and to establish phase reference planes. In this case, the calibration was performed in the following way.

The calibration method that was used here is known as the LRL or Line-Reflect-Line calibration that was set to exclude isolation. In calibrating the VNA, it was necessary to choose calibration planes – these were set to be at the interface between the elliptical polarisers and the helical tapers for both sides of the apparatus. Note that this was a two-port calibration using two different lengths of line. The LRL calibration consisted of three distinct stages. Firstly two LINE measurements were made using a section of smooth waveguide of the same mean radius as the corrugated waveguide of known length and cut-off frequency. Secondly, a REFLECT measurement was made by placing a short over each PORT. Note that here the reflection co-efficient was not known, but it was important to know that it was either above or below the line impedance at all frequencies (this ensures that one knows the sign of the reflection).

#### **4.8.3 Method for Analysis of Helically Corrugated Waveguide Dispersion**

Dispersion characteristics of the operating eigenwave can be found by launching a circularly polarised  $TE_{11}$  wave into the helix (which is of 4 axial periods length) and

measuring its phase evolution using the VNA. A new experiment was performed to measure the dispersion characteristics of a section of helically corrugated waveguide using the VNA measurement method.

As the VNA is only capable of measuring the principal value of the phase the actual measurement obtained is equal to the phase less  $2\pi n$  where  $n$  is an integer. For small corrugation depths and helix section lengths, the method of perturbation can be used to estimate the value of  $n$  to a good approximation. The change in axial wavenumber of the operating eigenwave is given by the change in phase due to the helix divided by the length of the helix.

The experimental setup for measurement of  $k_z$ , the axial wavevector for the operating eigenwave using the VNA is shown above in Figure 4.9. Coaxial to waveguide adaptors were connected to ports 1 and 2 of the VNA in order to allow the injection of the signal into the waveguide.

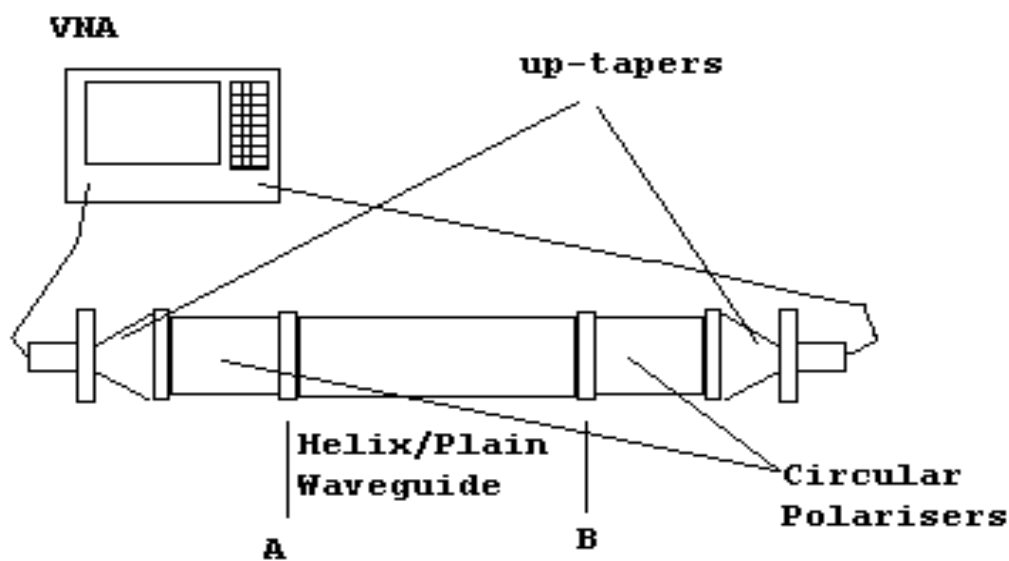


**Figure 4.9 Diagram of measurement of helix dispersion using VNA method.**

As the ends of these adaptors were rectangular waveguide, it was then necessary to convert to circular waveguide. It was important to ensure that the radius of the circular waveguide was such that only the  $TE_{11}$  mode could propagate. Rectangular to circular up-tapers were used to achieve this. The signal was then passed into

circular polarisers which were used to convert the linearly polarized signal into a circularly polarized one (with the correct direction of rotation). From here the signal passed into the helically corrugated waveguide, which was of approximately 4 periods length. Using this arrangement, it was possible to measure the phase evolution of the waveguide. Note that the circular polarizers used were operational over a 2.5GHz bandwidth and so measurements were limited to this frequency range.

As a preliminary experiment, the co-rotating circularly polarised TE<sub>11</sub> dispersion was measured and this was compared to the dispersion of a normal TE<sub>11</sub> mode in a circular waveguide of the same mean radius as the helix. These were found to be in good agreement.

A counter-rotating circularly polarised TE<sub>11</sub> wave was injected into the helix and the phase evolution of the eigenwave was measured and this was used to plot the dispersion using the well known expression

$$\phi = k_z L \tag{4.11}$$

where  $\phi$  is the phase and L is the length of the interaction region.

The raw data output from the VNA is shown in Figure 4.10.

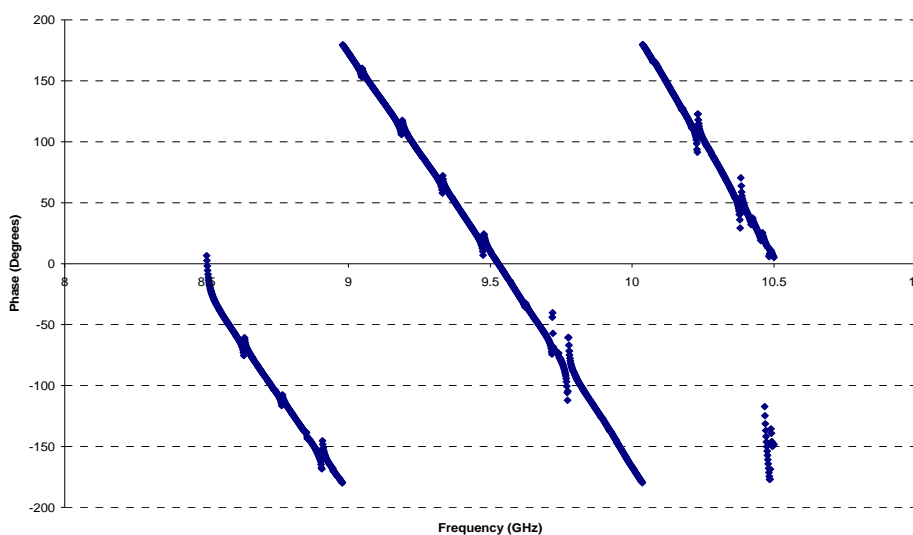


**Figure 4.10 Raw data output from VNA method for measurement of helix dispersion.**

As the VNA gives only the phase evolution within the integer 'n' revolutions, it is necessary to obtain this value n (for number of complete phase revolutions) by an iterative method using a spreadsheet in the Microsoft Excel software. Thus, it was possible to find the value of n for each frequency and phase value measured by the VNA and subsequently calculate the value of  $k_z$ , allowing the plotting of the dispersion – an example of this is shown in Figure 4.11.

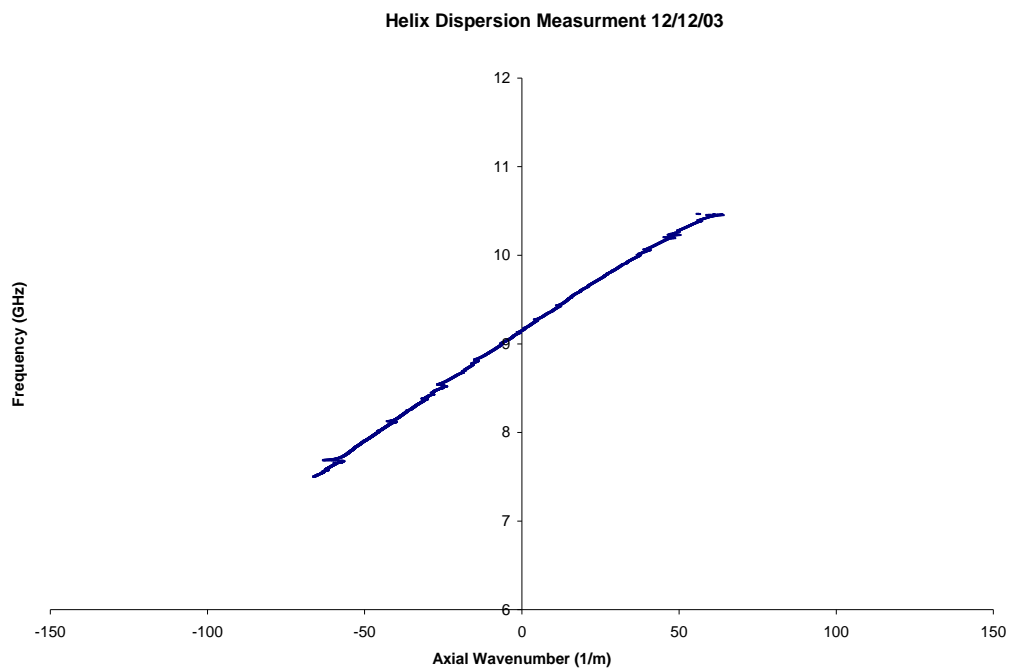


**Figure 4.11 An example of processed VNA data showing helix dispersion.**

Measurement of helix dispersion in this way saves much time in the experimental design stages as only a small section of helix needs to be made for measurement. It is also allows an accurate prediction of how the experiment is going to perform by providing the dispersion characteristics of the helically corrugated waveguide.

#### **4.8.4 Summary of Design Software**

The work presented here comprises a complete software design suite with novel new codes which allow the prediction of all experimental and geometrical parameters

prior to the construction stage of the experiment. As it was previously the norm to manufacture such components as the helix and bench test these to evaluate performance etc., this modelling saves much time in the design and construction stages of the experiment. Not only does it predict electron beam and interaction structure (helically corrugated) parameters, but it does so accurately and in very little time.

It is crucial to note here the key differences between MAGIC and prediction of the dispersion using the numerical method i.e. perturbation theory. This lies in the fact that MAGIC allows one to simulate a system using an approximated geometry, whereas perturbation theory makes approximations of the laws of physics. As it is already accepted that use of perturbation theory imposes an upper limit of corrugation depth on the helically corrugated waveguide, it is obviously desirable and necessary to have a method which will allow the prediction of dispersion characteristics for deeper corrugations and this was the purpose for which the MAGIC code was designed.

After much study and evaluation of results output by each code, it was possible to suggest a new strategy for the prediction of gyro-TWA experimental parameters. Firstly, Microsoft Excel was used to give a rough approximation of the helix parameters using perturbation theory. Note that in solving perturbation theory in this way, it can only be assumed that the dispersion calculated is fairly near the true value. This is due to the fact that, as mentioned earlier, perturbation theory is only accurate when dealing with small corrugation depths. As it is not trivial to ascertain the corrugation depth cut-off point for which this theory becomes inaccurate, it was necessary to assume that the input depth was sufficiently small. These helix parameters would then be entered into the MAGIC code for prediction of the dispersion. Here it was necessary to carefully adjust parameters to achieve the correct dispersion characteristics. Once confirmed numerically, a final experimental check was performed on a short section of fabricated waveguide. The linear gain was then modelled and again key parameters (electron beam parameters in this case) were carefully adjusted in order to attain the desired linear gain. All parameters could then

be input to the MAGIC gyro-TWA code which would allow the prediction of gain, stability to oscillations etc. for the final experiment.

Thus, after using each code in this way it was possible to obtain accurate values for all necessary experimental and geometrical parameters.

## **Chapter 5. Results**

## 5.1 Introduction

In this chapter experimental results are presented for measurements of the dispersion of the helically corrugated waveguide sections, as well as calculations of the ‘cold’ and ‘hot’ dispersion by perturbation theory, linear theory and numerical calculation. The term ‘cold’ refers to experiments or simulations which are conducted without an electron beam source. The term ‘hot’ is simply the converse of this.

The following chapter will compare these calculations with each other and with experimental data.

## 5.2 Measurement of Helically Corrugated Waveguide

In this section, the results obtained using a novel method to measure the dispersion characteristics of a section of helically corrugated waveguide using a Vector Network Analyser are presented. For a detailed description of this method, the reader should refer to Section 4.8.2.

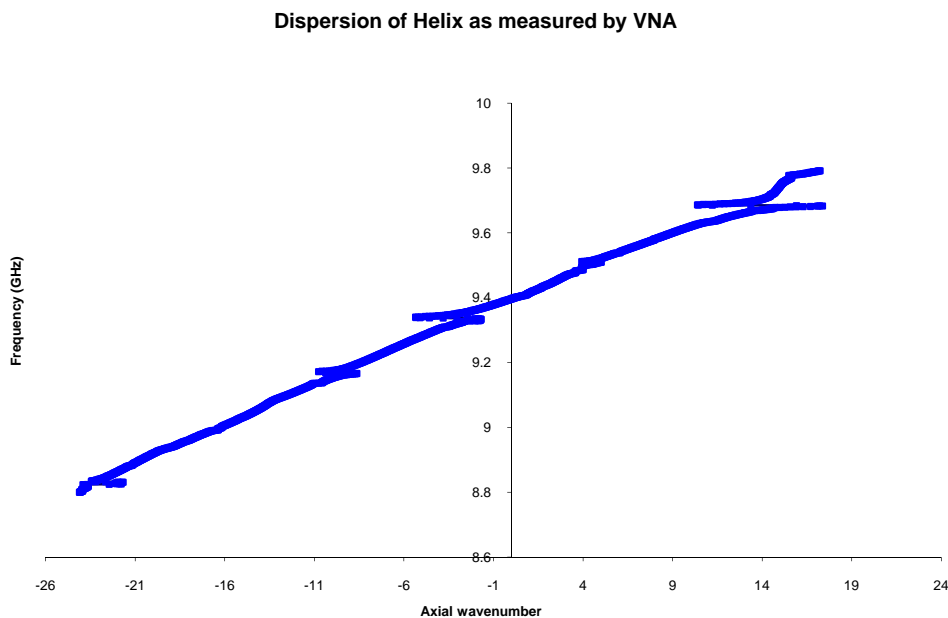


**Figure 5.1 Dispersion characteristics of section of helix with dimensions  $a_0 = 1.41\text{cm}$ ,  $a_1 = 0.22\text{cm}$ , and  $d = 3.7\text{cm}$  as calculated from VNA measurements.**



Figure 5.1 shows the dispersion characteristics of a section of helically corrugated waveguide as calculated from VNA measurement data. The discontinuities in the data are probably due to weak cavity resonances at specific frequencies combined with singularities caused by regions of frequency where the error matrix was ill-conditioned.

### **5.3 Numerical Models**

This following section discusses briefly the two methods used to predict the dispersion of the helically corrugated waveguide and also highlights the differences between these. The limitations of each model are also discussed and thus the importance of utilising two methods is shown.

#### **5.3.1 Modelling of Helically Corrugated Waveguide**

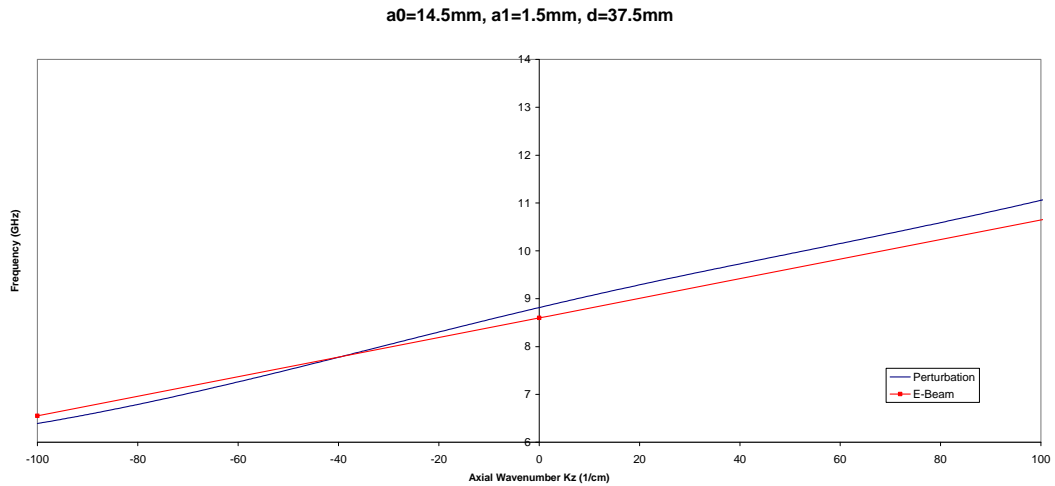
When modelling the helically corrugated waveguide prior to manufacture, it is of paramount importance that we obtain as accurate an approximation of the various important geometrical parameters needed to obtain the required dispersion and therefore the predicted performance of the amplifier as possible. This was achieved by the use of two methods: one based on an analytical approach using perturbation theory and the other an application of the PIC mode MAGIC.

The importance of the utilisation of two methods should not be underestimated. The analytical approach uses perturbation theory and makes various approximations of the laws of physics whereas the MAGIC approach makes approximations for the geometry and for the values of the fields which are represented on a finite mesh within a PIC code simulation.

#### **5.3.2 Perturbation Theory**

For a relatively small corrugation depth, with  $\sigma < 0.1$ , the method of perturbation can be used to predict the dispersion for the helix with good agreement with ‘cold’ (in the

absence of an electron beam) experiments.



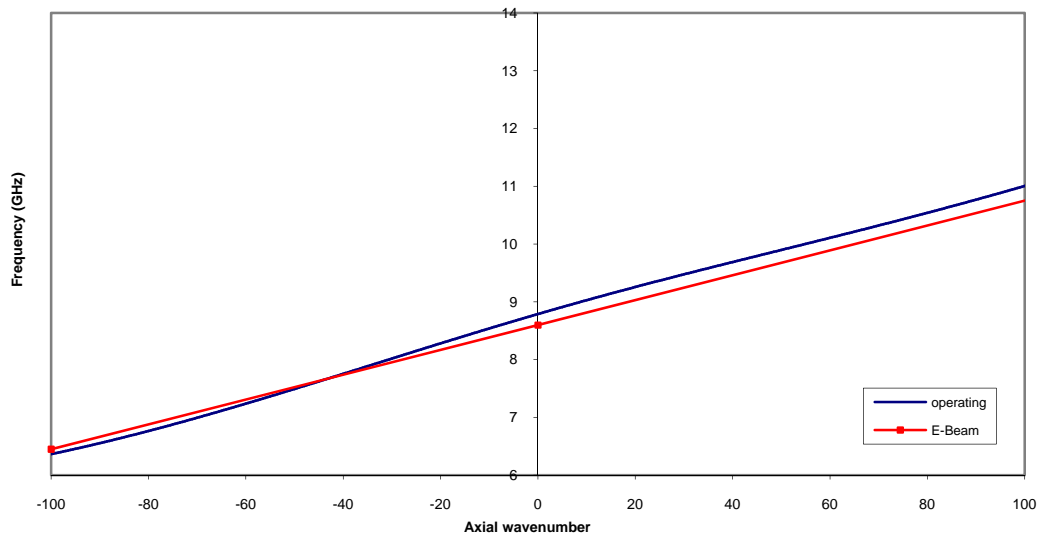
**Figure 5.2 Plot showing prediction of dispersion for helically corrugated waveguide with electron beam dispersion.**

Figure 5.2 illustrates the dispersion of a waveguide having a mean radius of 14.5mm, with a corrugation amplitude of 1.5mm and a period of 37.5mm superimposed with the dispersion of a typical cyclotron electron beam. The electron beam dispersion was plotted by finding the cyclotron frequency in the conventional way and then taking the second harmonic of this and adding the Doppler-shift term (Equation 3.1) for  $k_z = -100, 0,$  and  $100$  (cm). Note that these values were chosen so as to ensure the beam dispersion was extrapolated to the full scale of the plot. This waveguide had a coupling factor,  $\sigma$  of 0.117. The electron beam in this plot has a cyclotron frequency of 8.71 GHz set by a magnetic flux of 0.212 T and a beam energy of 185 kV. The

electron beam pitch factor was  $\alpha = \frac{V_{\perp}}{V_{\parallel}} = 1.1$ .

In Figure 5.3 the dispersion characteristics of the helically corrugated waveguide employed in the benchmark experiment (in year 2000) are illustrated, along with the electron beam dispersion. The coupling co-efficient,  $\sigma$ , used here was 0.116.

### Dispersion Characteristics for Helix $a_0 = 1.41\text{cm}$ , $a_1 = 0.22\text{cm}$ and $d = 3.7\text{cm}$



**Figure 5.3 Plot of dispersion characteristics for helix with parameters  $a_0 = 1.41\text{cm}$ ,  $a_1 = 0.22\text{cm}$ , and  $d = 3.7\text{cm}$  as calculated by perturbation theory. Electron beam dispersion is also added.**

### 5.3.3 MAGIC Simulation of the Helical Waveguide

As was described in Chapter 4, a MAGIC code was used in conjunction with an Excel spreadsheet to obtain predictions of the dispersion characteristics of a helically corrugated waveguide.

Predicted dispersion characteristics of a helically corrugated waveguide with  $a_0=1.315\text{cm}$ ,  $a_1 = 0.25\text{ cm}$  and  $d = 3.7\text{cm}$  are shown in Figure 5.4.

Figure 5.5 shows the dispersion characteristics predicted by the MAGIC code for a helical waveguide with dimensions  $a_0 = 13.15\text{ mm}$ ,  $a_1 = 2.05\text{ mm}$ , and  $d = 37\text{ mm}$ . These results will later be compared to both other numerical methods and (in one case) to experimental results.

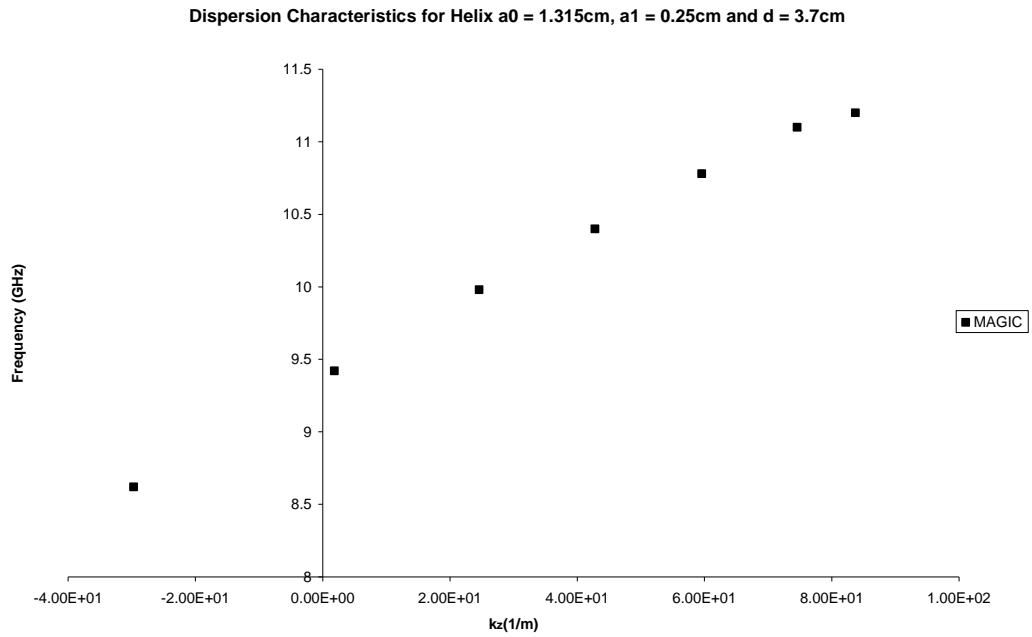


**Figure 5.4** Plot of dispersion characteristics for helically corrugated waveguide with parameters  $a_0 = 13.15$  mm,  $a_1 = 2.05$  mm,  $d = 37$  mm as predicted by the MAGIC code.

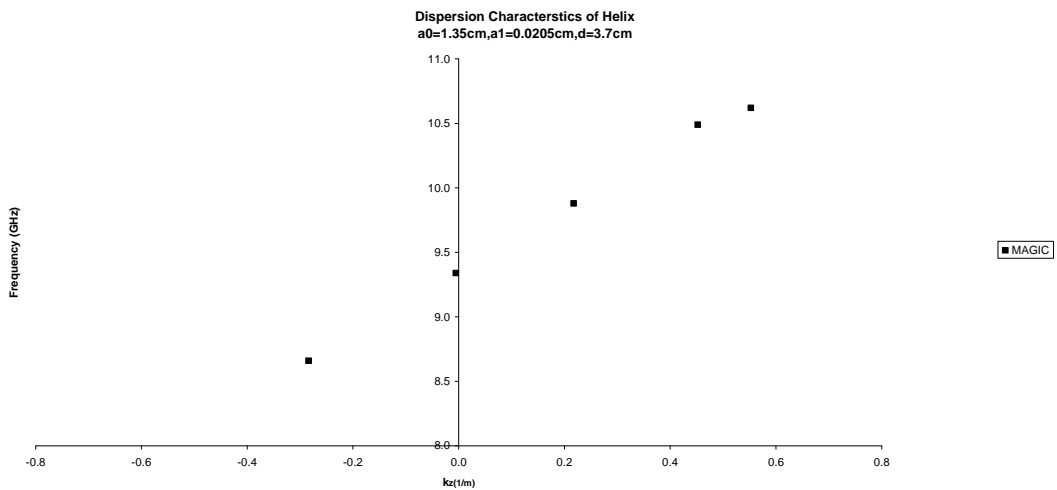


**Figure 5.5** Plot of dispersion characteristics for helically corrugated waveguide with parameters  $a_0 = 13.5$  mm,  $a_1 = 2.05$  mm,  $d = 37$  mm as predicted by the MAGIC code.

### 5.3.4 MAGIC Simulation of the Amplifier

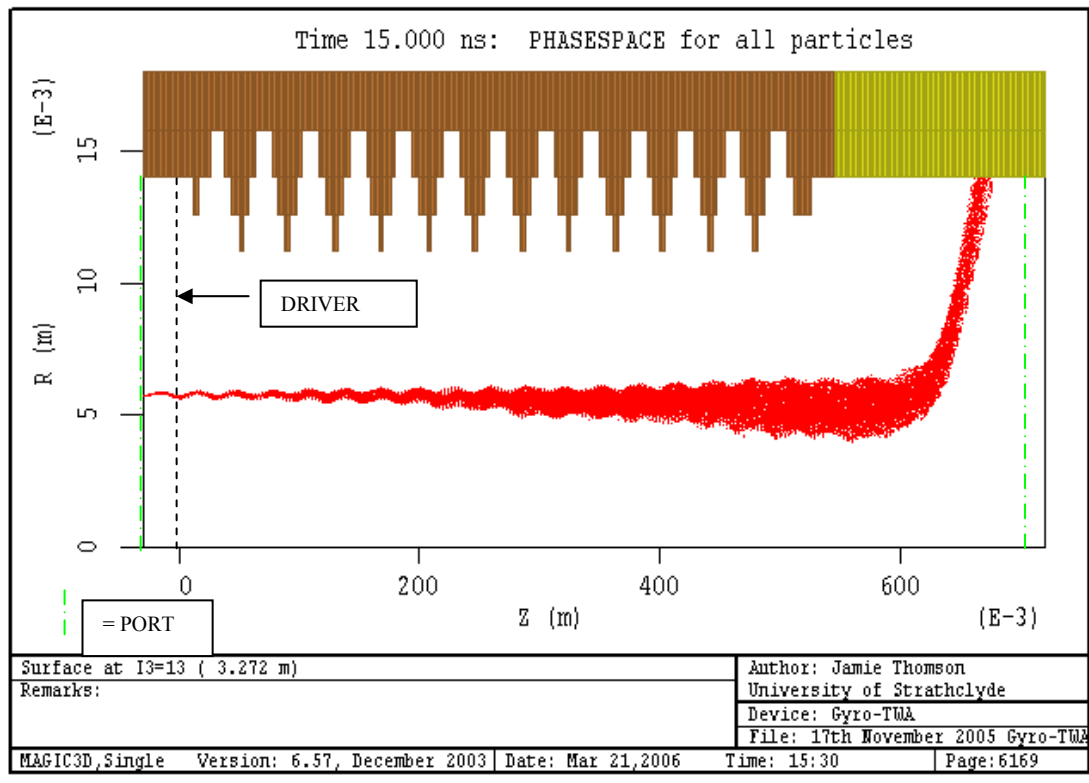


**Figure 5.6 Cross sectional view of Gyro TWA MAGIC simulation geometry.**

A code was written using MAGIC to simulate a gyro-TWA incorporating a helically corrugated waveguide with the parameters shown in Table 5.1:

Helix Length	60cm
Taper Lengths	12cm
Mean Radius ( $a_0$ )	1.4cm
Corrugation Amplitude ( $a_1$ )	0.22cm
Corrugation Period (d)	3.9cm
Accelerating Potential (V)	185kV
Beam Current (I)	20A
Beam ( $\alpha$ )	1.1
Magnetic Flux Density (B)	0.212T
Drive Power	1W – 500W

**Table 5.1 Experimental parameters for year 2000 experiment.**

where  $a_0$  is the mean radius,  $a_1$  is the corrugation depth, and  $d$  is the corrugation period. The electron beam and other experimental parameters from the 2000 experiment are also shown –  $V$  is the electron beam voltage,  $I$  the electron beam current,  $\alpha$  the pitch factor and  $B$  the confining magnetic field. This geometry has the same configuration as in the previous experiment referred to in Chapter 4.

The basic geometry of the simulation is shown in Figure 5.6 and consists of the following:

A short section of circular waveguide as an input beam tunnel (from approx -3cm to 0 cm in diagram), a section of helically corrugated waveguide of  $n$  periods ( $n$  in the case shown was of 12 periods length), ending with an output section of circular waveguide.

Ports were positioned as shown in Figure 5.6.

In order to model this particular configuration, it was found rather problematic to introduce both an electron beam and radiation to the geometry. This was thought to be due to inherent problems with the MAGIC software itself in that it has very strict rules for positioning of ports and strange behaviour was observed when trying to insert both radiation and an electron beam using the standard methods i.e. PORT commands, defining plane to inject radiation etc. This problem was resolved (refer to Section 4.6) by incorporating the DRIVER command to drive the radiation at a plane defined in the code (driver position is shown in Figure 5.6) and then using the IMPORT command to import electron beam data (particle and field data) from another simulation. The latter simulation used a very simple geometry (a short, circular waveguide) with the electron beam propagating through it and then the beam data captured at the output port using the EXPORT command. After various tests, it was found that this was an effective and satisfactory way of including both electron beam and electromagnetic radiation into the main section of code.

It is of vital importance that the mesh density for the MAGIC simulation is selected

to ensure accurate results whilst maintaining reasonable code runtime.

The basis for selection of the mesh density is the Nyquist Theorem

$$\Delta x \sim \lambda / 3$$

This implies that

$$\Delta x \sim \lambda / 10 \quad \text{to deal with non-sinusoidal behaviour}$$

Similarly to accurately describe structure sizes, for example the sinusoidal corrugation of the waveguide we must also set resolution according to

$$\Delta x \sim \text{dim} / (5 - 10)$$

It should be noted that using a high resolution mesh impacts greatly on the simulation runtime as

$$\text{runtime} \sim 1 / \Delta x^4.$$

Since the time step  $\sim 0.8 * (\Delta x / c)$  (Courant Stability Requirement)

Therefore runtime varies with the mesh size as  $(x / \Delta x)(y / \Delta y)(z / \Delta z)(t / \Delta t)$

From these relationships it can be demonstrated that doubling resolution increases the RAM requirement of the PC increase by a factor of 8 and runtime of the simulation increases 16-fold. This clearly highlights the importance of properly selecting the mesh resolution in order to gain accurate results with reasonable runtime.

Another aspect to be considered as regards mesh density is that reducing  $\Delta t$  increases  $t / \Delta t$  and thus the number of computations. This could result in a cumulative error effect resulting in the growth of numerical error.

The density of the mesh for the simulation was chosen partly by taking into account previous work done at Strathclyde to investigate the effect of mesh density on runtime and accuracy and also by running identical physical problems from a coarse to a fine mesh. Once the effects in results became very slight, the optimal mesh density was chosen and used for all codes to maintain consistency (refer to Table 5.2).

Axial resolution	Radial resolution	Azimuthal Resolution
$d/78\text{mm} = 0.5\text{mm}$ where $d$ = period of corrugation for helix = 3.7cm here	$a_1/2.2 = 1\text{mm}$ where $a_1$ = the corrugation depth for helix = 0.22 cm here	$2\pi/23$

**Table 5.2 Axial, radial and azimuthal resolutions chosen for MAGIC code.**

It is interesting to note how the rationale for selection of the chosen resolution. There are 3 azimuthal corrugations, and therefore the arc subtended by one is  $2 * \pi/3$ . Hence the azimuthal resolution should be less than approximately one third of this to satisfy a sort of spatial Nyquist requirement and thus the chosen resolution easily satisfies this at  $2\pi/23$ .

It should be noted that the PORTS in the code are matched for the actual simulation frequency. After numerous studies it was found that this method of PORT matching seems to be imperfect and only gives valid results for a short time period. After this time radiation reflections complicate the system and this in turn was found to cause strange anomalies in the results.

The following results were gained by IMPORTing an electron beam with the following parameters into the MAGIC code:

$$B = 0.212 \text{ T}, V = 185\text{kV}, \alpha = 1.1, \text{Input RF Drive power} = 100\text{W}$$

Note that where a result is presented at a given frequency, the simulation frequency was 9.2GHz. Also, the following results are for a helically corrugated waveguide of 16 periods length.

It is important to note the differences between the MAGIC simulation and the actual 2000 experiment itself. Firstly the MAGIC code included no input coupler as the experiment did. The input coupler and output antennae were replaced in the MAGIC code by setting up current sources with the DRIVER command and an output aperture with the PORT command. The electron gun was not modelled in the



MAGIC simulation, instead a beam was modelled and then this data was imported into the simulation (by way of the DRIVER command). As the beam imported was chosen to be axis-encircling this allowed an accurate modelling of the experiment without either the beam or kicker being separately modelled. No elliptical convertor was included in the MAGIC simulation – although one was present in the experiment.

The most important difference was that a 10dB sever which had been present in the 2000 experiment was not present in the simulation. It would be logical to assume then that higher gain etc. would result from the simulation than was recorded in the experimental results.

Figure 5.7 shows the variation of saturated gain with frequency for the gyro-amplifier configuration modelled by the MAGIC code. This plot was obtained by varying the driving frequency of the simulation and calculating the gain using the input and output powers after one pass through the amplifier. The gain curve is relatively flat, varying from approximately 33 to 37db over a 2GHz frequency band. This flat shape of curve was related to the fixed detuning and coupling of the system interaction over a wide spectral range due to the helical waveguide (refer to Section 5.3). Hence the fluctuations indicate small variations in detuning.

It should be noted that over the spectral range from 8.2GHz to 10.2GHz, single mode  $TE_{11}$  output was observed. Outwith this frequency range the MAGIC simulation indicated the undesired operating transverse eigenmode. Thus results outwith this frequency band were not plotted.

Variation of Gain with Frequency as calculated by MAGIC code  
 (a0=1.4cm, a1=0.22cm, d=3.0cm), Input Drive of approx.  
 100W, 185kV, 20A, Alpha = 1.1, B = 0.212T

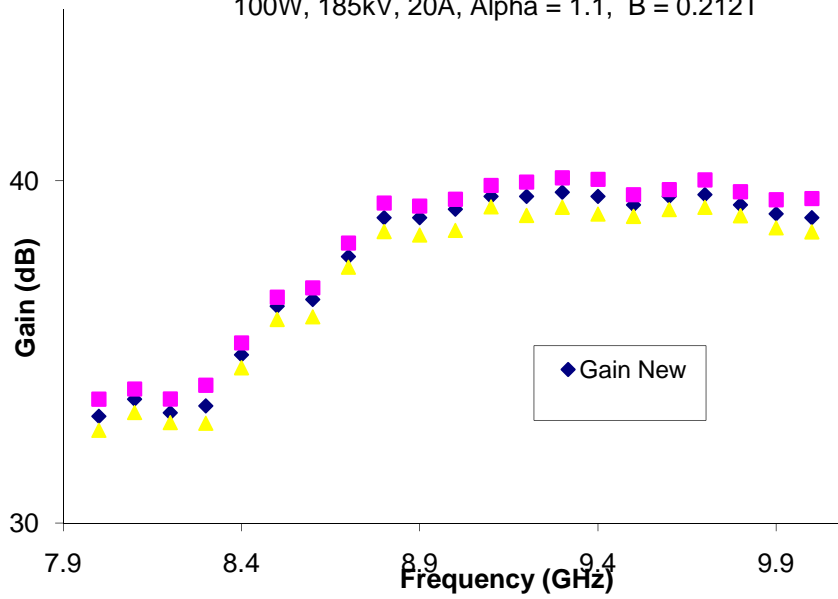


**Figure 5.7** Variation of saturated gain vs. Frequency as calculated by MAGIC code.

Output Power and Gain versus Input Power at f = 9.2 GHz for 2000 paper helix parameters

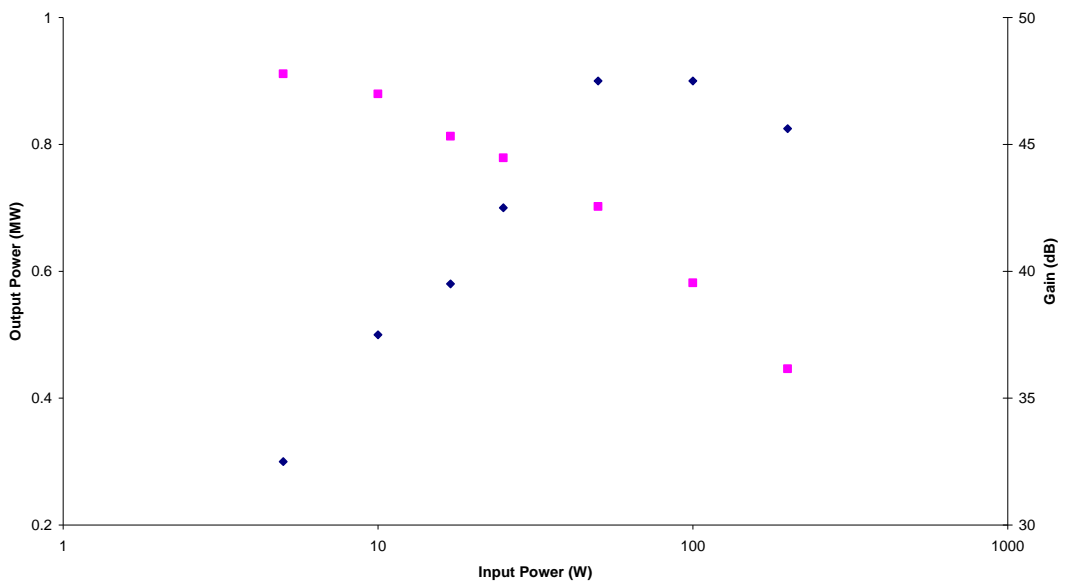


**Figure 5.8** Gain and output power versus input power.

In Figure 5.8, the gain and output power as a function of input power are illustrated. From this plot it can be seen that there is a roll-off as we move to higher input powers due to saturation. In this particular case, the saturation is due to the phase-trapping effect. This is where sufficient energy has been removed from the electrons such that their mean cyclotron frequency has increased sufficiently that they move into accelerating phase with respect to the microwave field.

Figures 5.9 - 5.11 show the raw data plots obtained from the MAGIC simulation for power at various points along the simulation geometry. The location of the driver can be seen from Figure 5.6. Results of the Poynting flux at the drive location and the outlet provide the basis for the results of Figures 5.7 and 5.8.

It is important to note here the point at which output power was measured from the MAGIC simulation plots (as in Figure 5.9). The output power used for gain calculations was selected to be at the first peak in power after enough time had passed for the electron beam to traverse once through the interaction structure to the output region. This was taken to be around the 12ns point. The reason for this was that the MAGIC code was found to produce strange results after this time due to radiation reflecting and passing back through the simulation causing the DRIVER function to re-adjust due to some internal correction algorithm. This caused unstable behaviour and so any output after this 12ns point was deemed to be invalid (see Fig 5.9 after 12ns).

In order to calculate gain from these output powers in dB, the following relation was used

$$G = 10 \log_{10} \left( \frac{P_{out}}{P_{in}} \right) \quad (5.1)$$

Note that in this case (Figure 5.10) the input power was 100W.

As the power values shown in Figure 5.9 are fluctuating due to the nature of the

measurement made in MAGIC, the actual power is the average of this periodic fluctuation. Hence the 200 W shown here actually corresponds to a 100W input drive power.

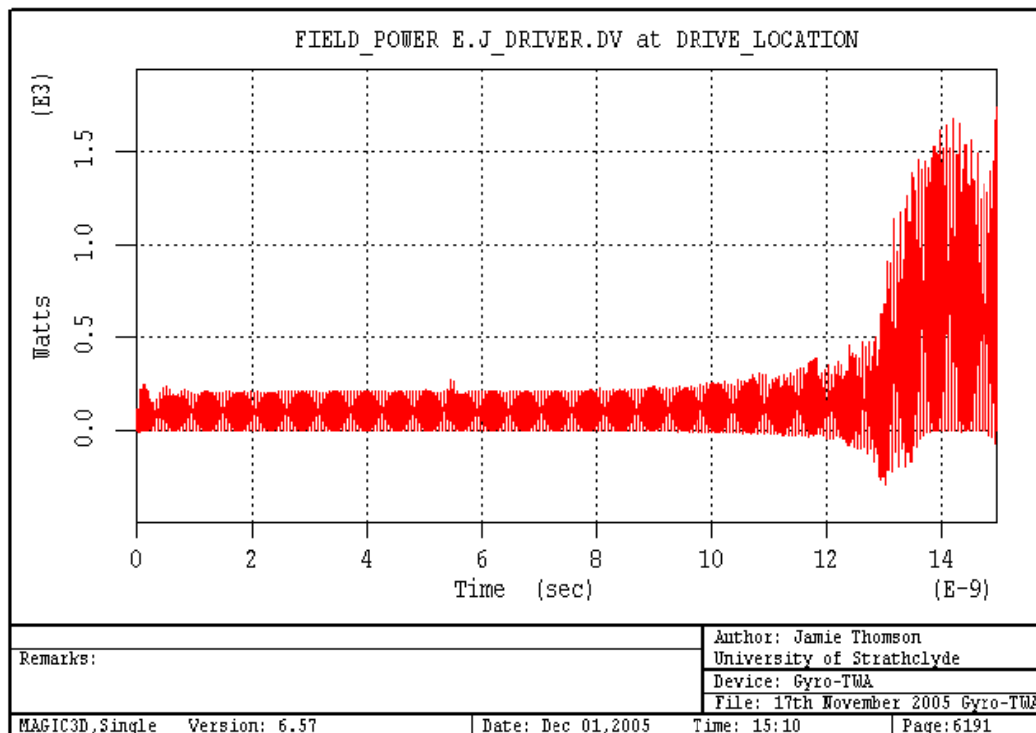


Figure 5.9 Input power from DRIVER command as function of time.

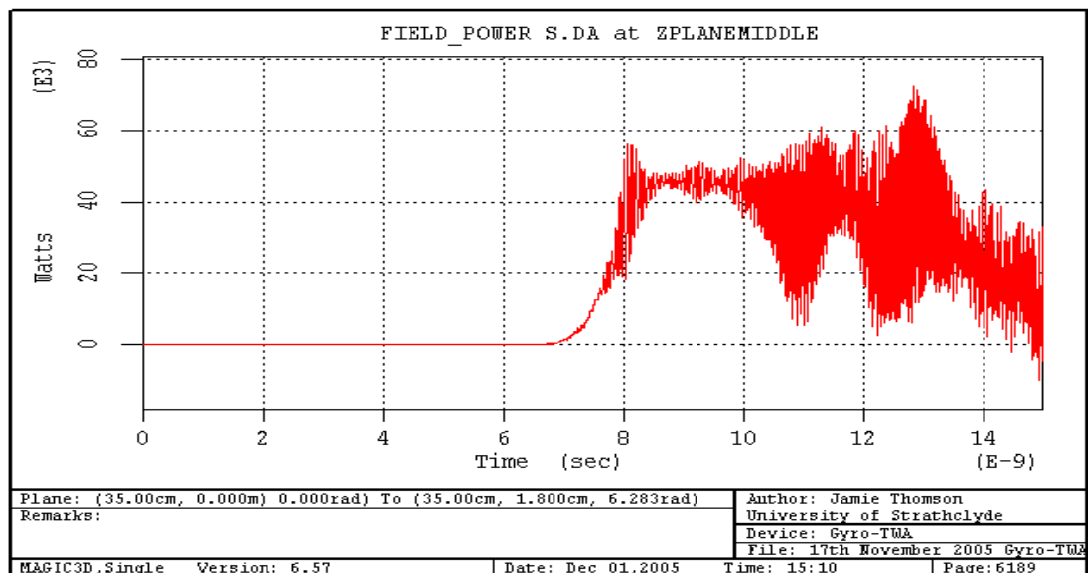
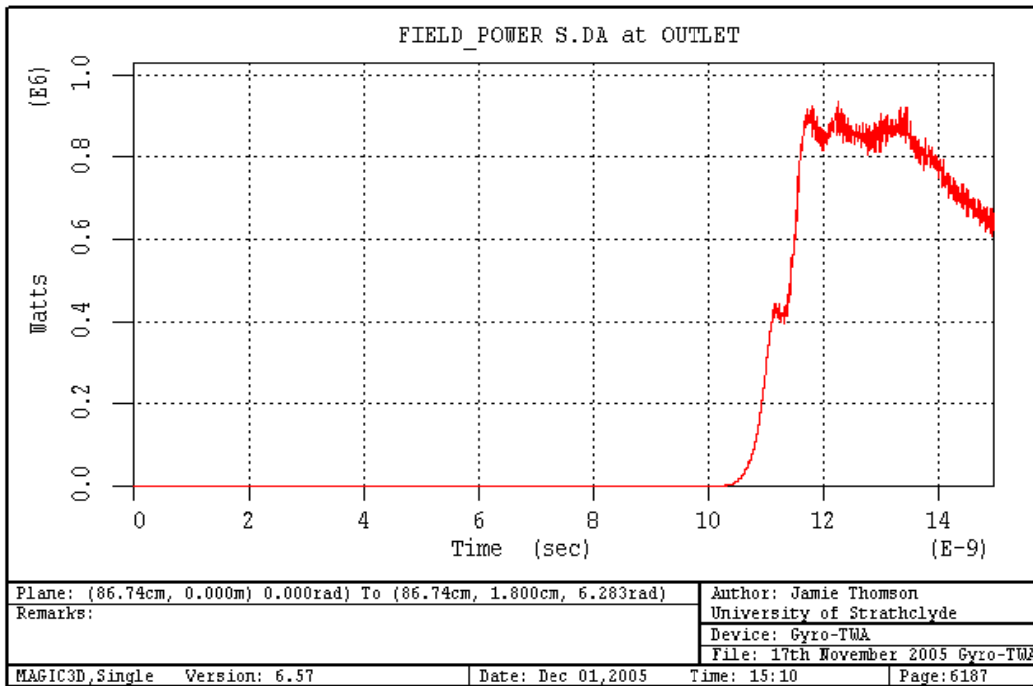
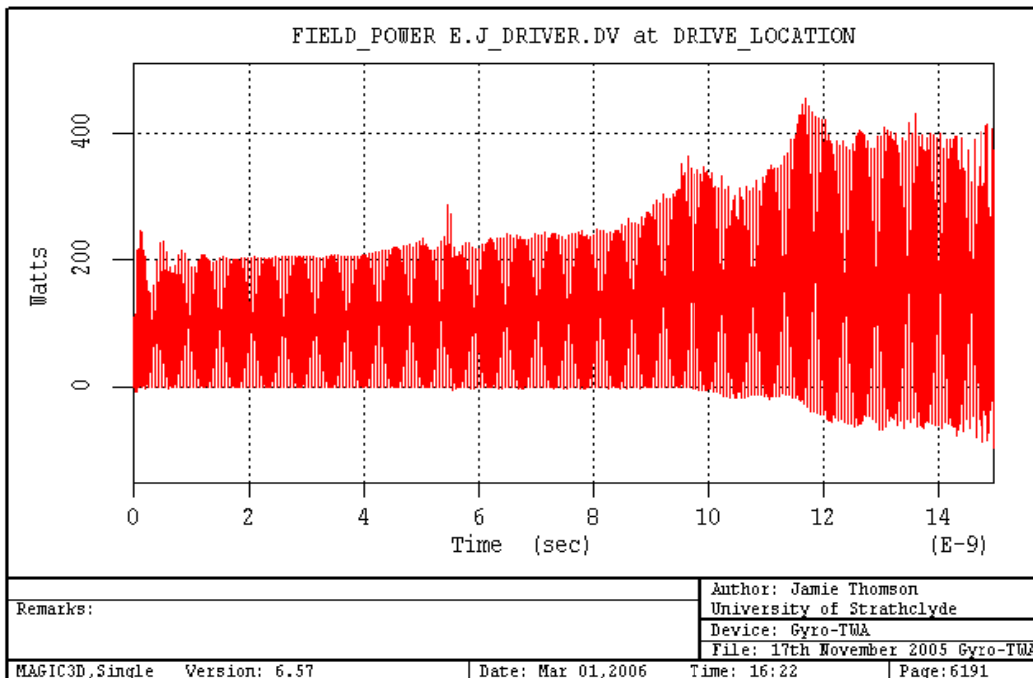


Figure 5.10 Power at mid-point of helically corrugated waveguide as function of time.



**Figure 5.11 Power at output PORT as function of time.**

The following results were achieved by shortening the helically corrugated interaction structure (to 8, 12 and then 13 periods) for an operating frequency of 9.2GHz. This was also compared to the previous result using 16 periods length.



**Figure 5.12 Driver input power variation with time (8d length, 9.2GHz).**

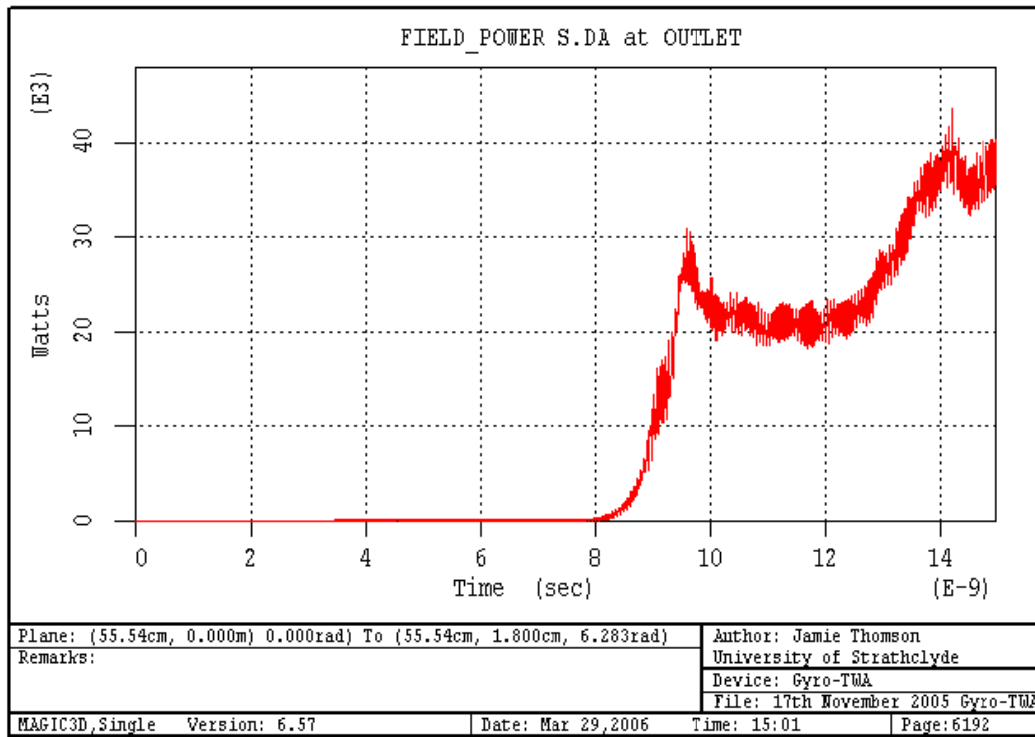


Figure 5.13 Output power variation with time (8d length, 9.2GHz).

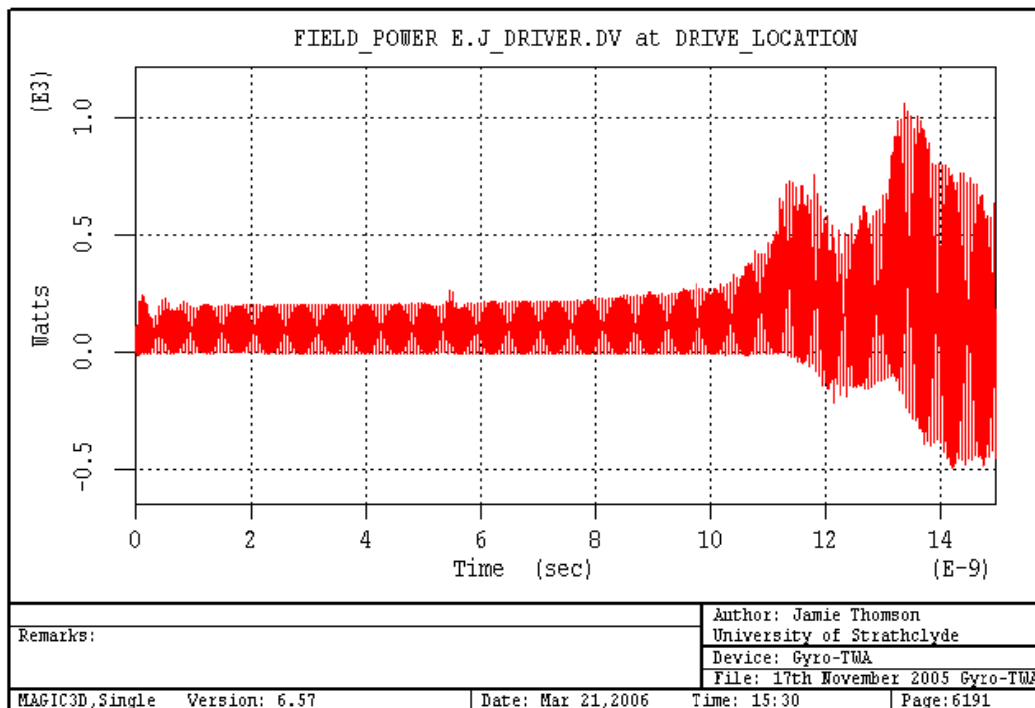


Figure 5.14 Driver input power variation with time (12d length, 9.2GHz).

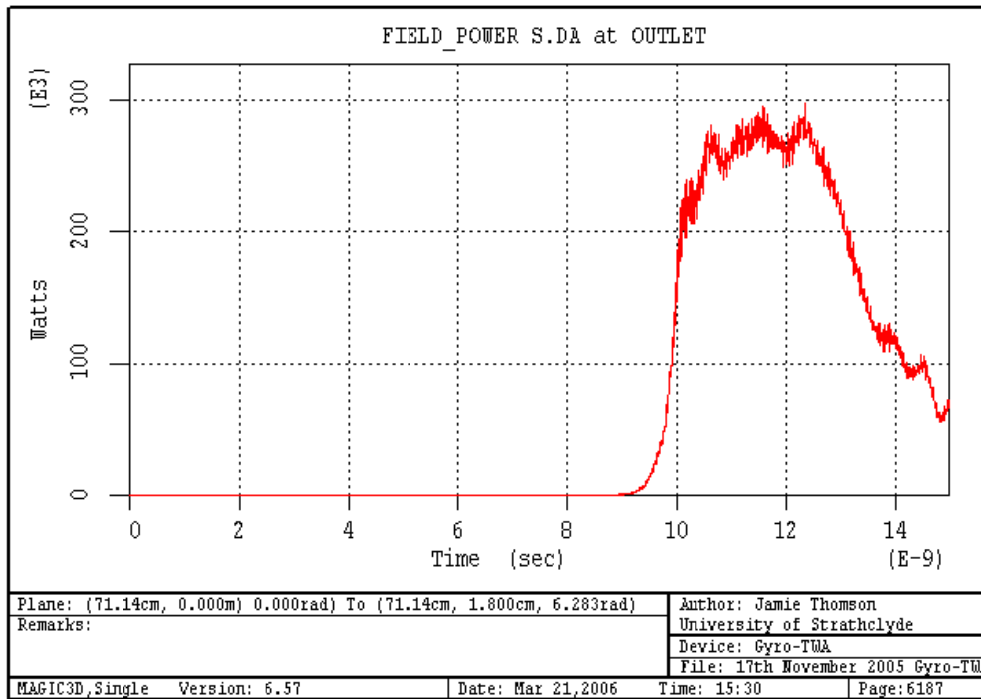


Figure 5.15 Output power variation with time (12d length, 9.2GHz).

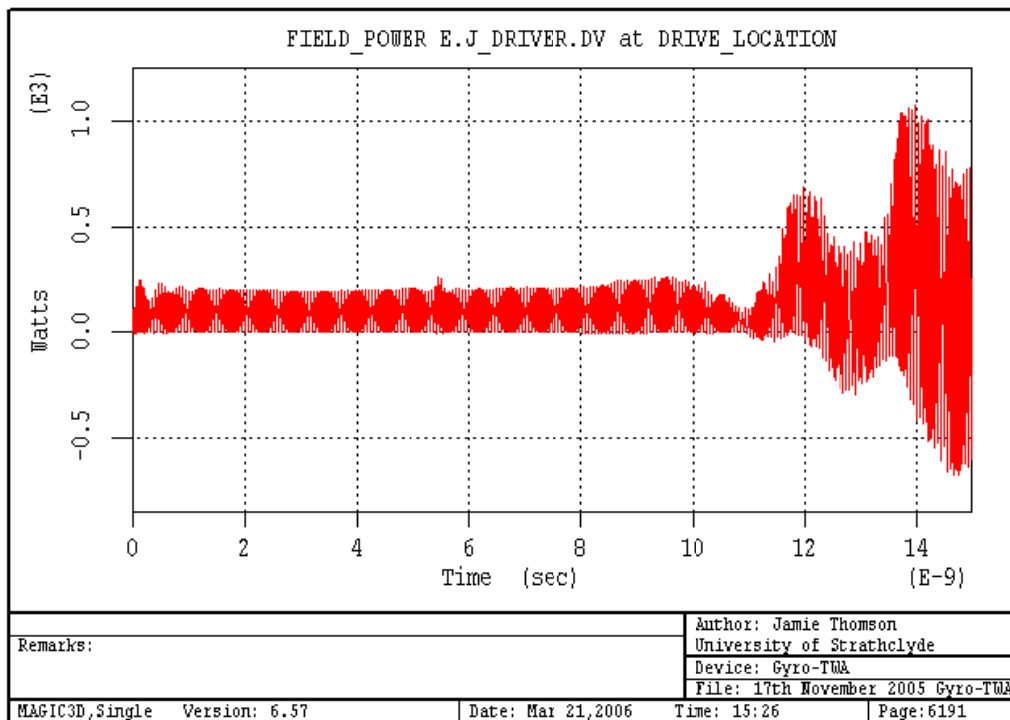
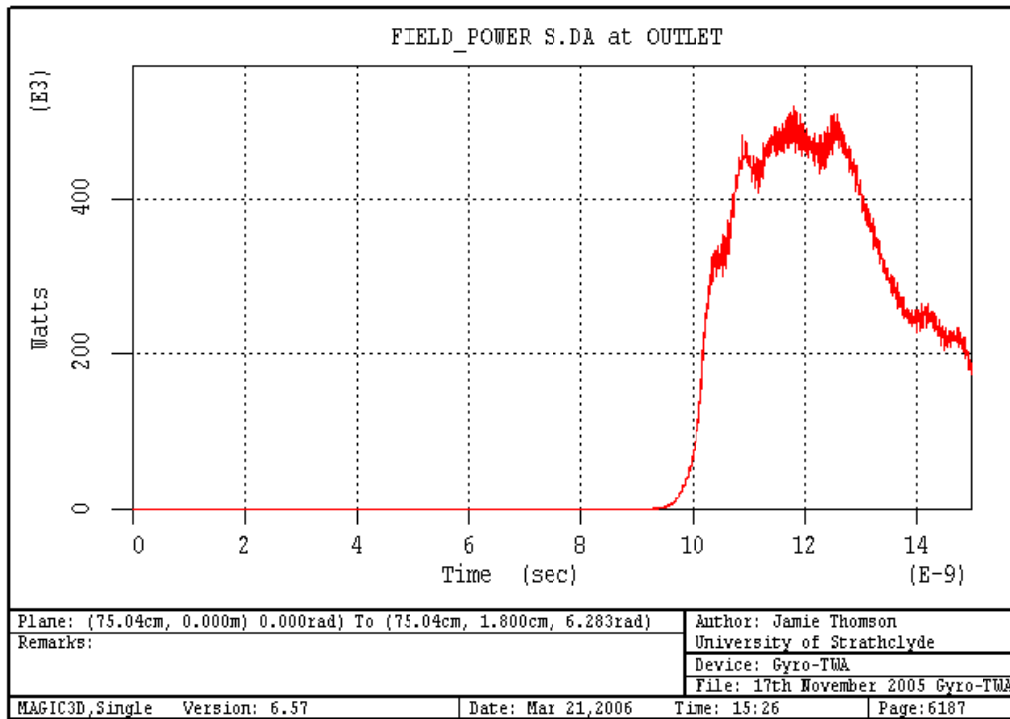
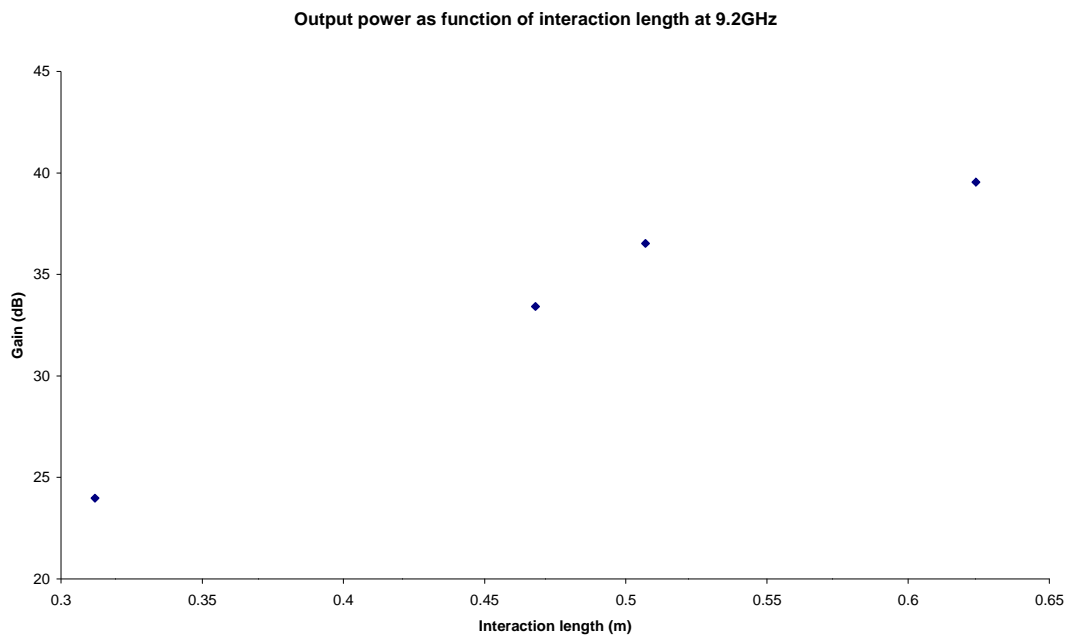


Figure 5.16 Driver input power variation with time (13d length, 9.2GHz).



**Figure 5.17 Output power variation with time (13d length, 9.2GHz).**



**Figure 5.18 Output power as a function on interaction length at 9.2GHz with input drive power of 100W for parameters shown in Table 5.1.**



The relationship between output power and interaction length in Figure 5.18 can be explained by noting that in any amplifier we have a growth of signal in space. Hence by reducing the length of the interaction structure, whilst holding the gain per unit length constant the exponential amplitude has less growth - there is less gain. Note that the input power used for this study of gain variation with interaction length was 100W.

The apparently large variation in efficiency illustrated in Figure 5.19 compared to Figure 5.7 is due to the fact that this parameter is not plotted on a log scale (whereas the gain shown in previous plots is). Note that the experimental drive frequency was 9.2GHz.

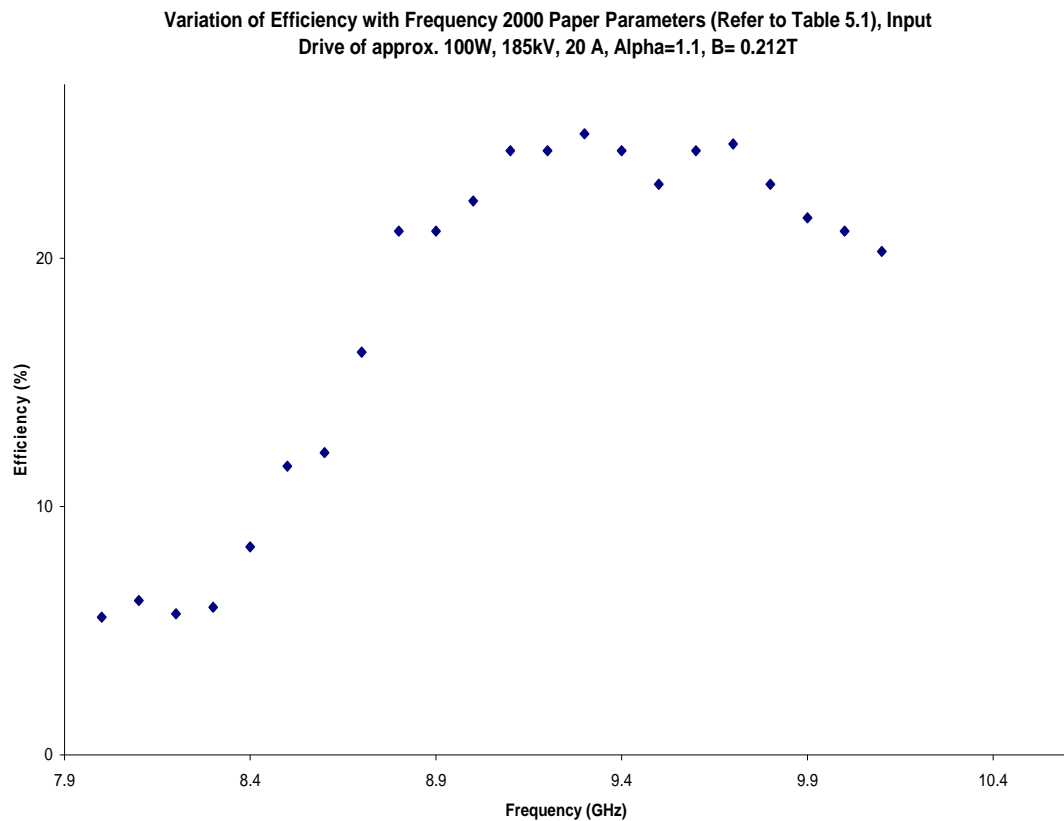


**Figure 5.19 Variation of efficiency with frequency.**

The following diagram (Figure 5.20) shows the Fourier Transform (FFT) of the frequency spectrum for the Erho component of the electric field in the parallel plane

at the output of the MAGIC simulation.

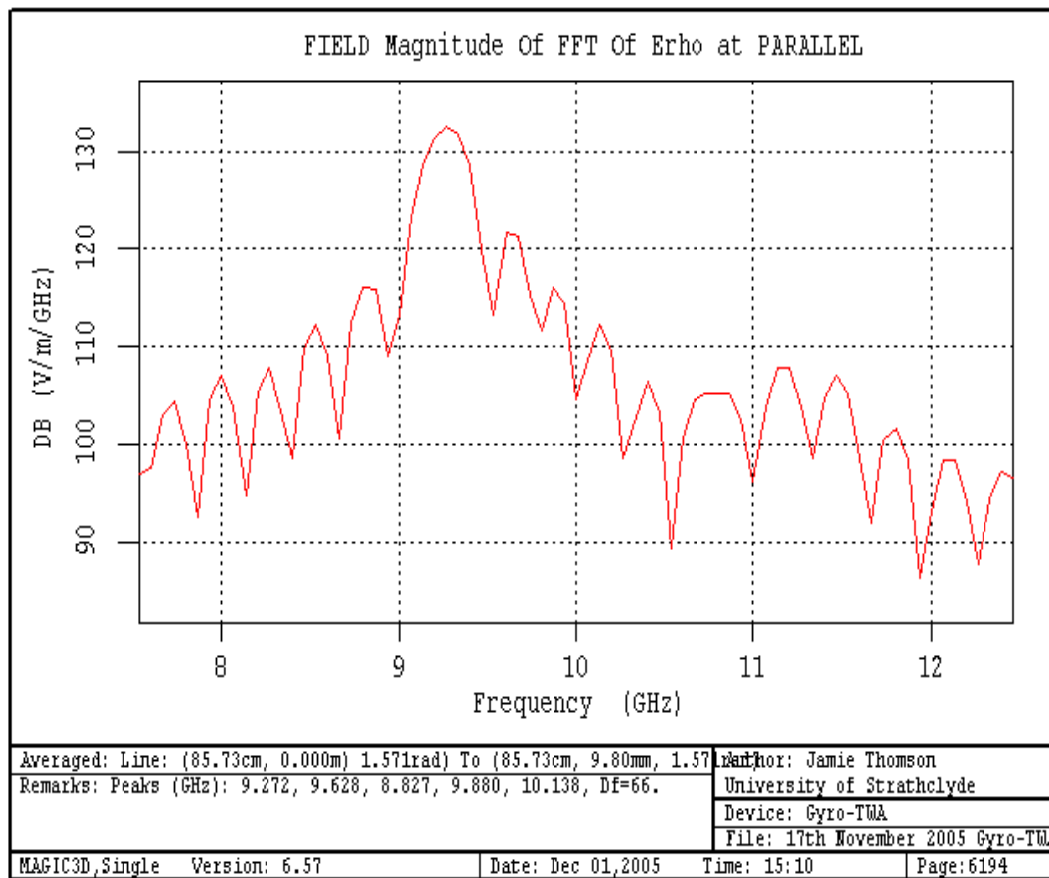


**Figure 5.20 Frequency spectrum at output.**

The low spectral resolution in Figure 5.20 was due to the fact that the plot shows the transform of the Erho field component of a relatively small window. It is hence reasonable to expect that by increasing the range of this transform would decrease these variations. However the onset of feedback oscillations limits our potential to do this.

When dealing with the MAGIC PIC code, it is always of the utmost importance that checks are made to ensure the simulation still outputs the required operating mode (in this case the TE<sub>11</sub> mode). This was done by taking contour field plots at various planes in the simulation - particularly at the output (Refer to Figure 5.21-5.26 below). Thus it was ensured that all measurements were valid.

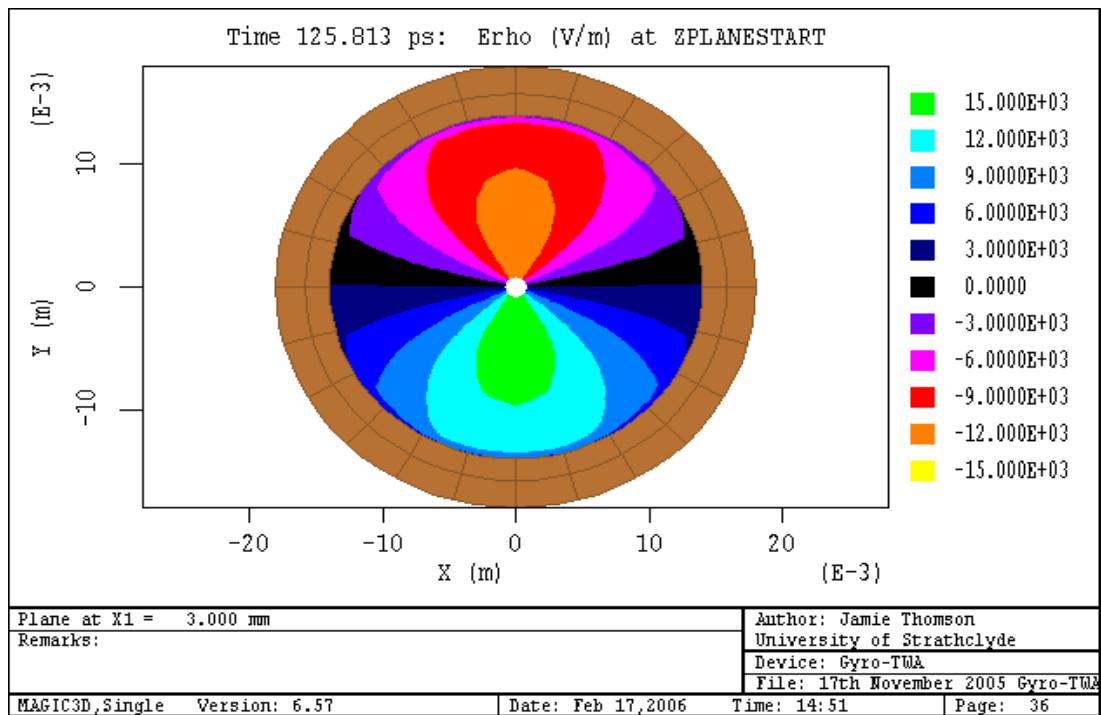


**Figure 5.21** Contour plot showing Erho component of electric field at near the input of the MAGIC gyro-TWA simulation.

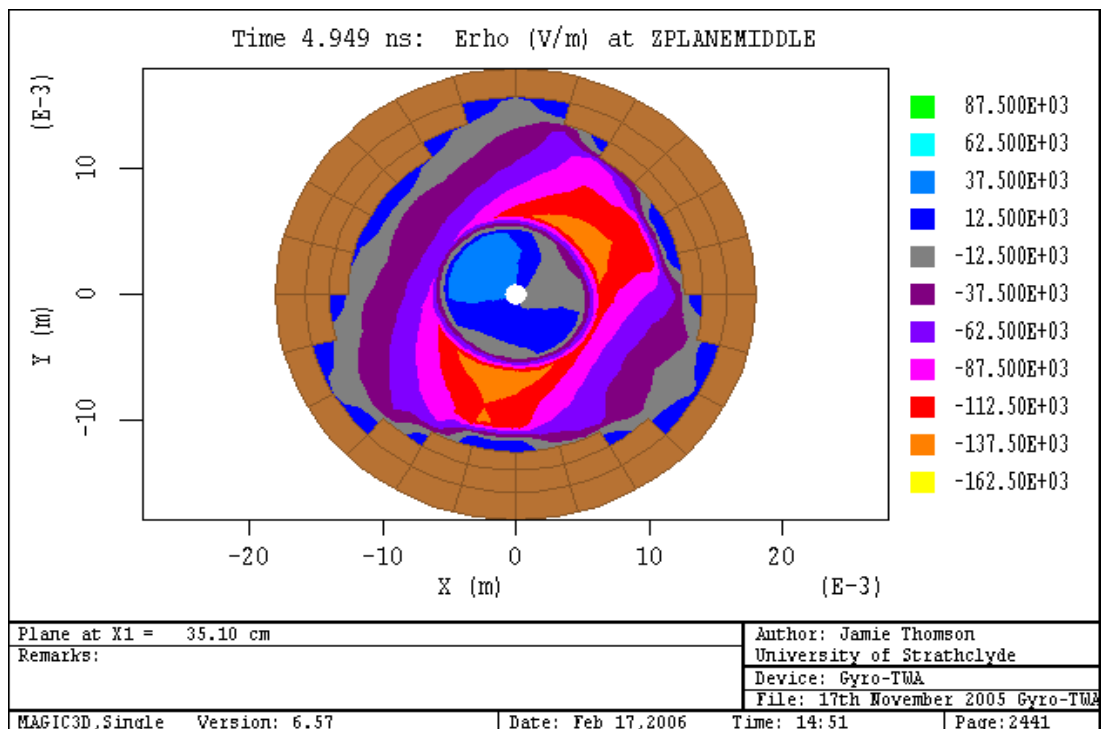


**Figure 5.22** Contour plot showing Erho component of electric field at the middle of the MAGIC gyro-TWA simulation.

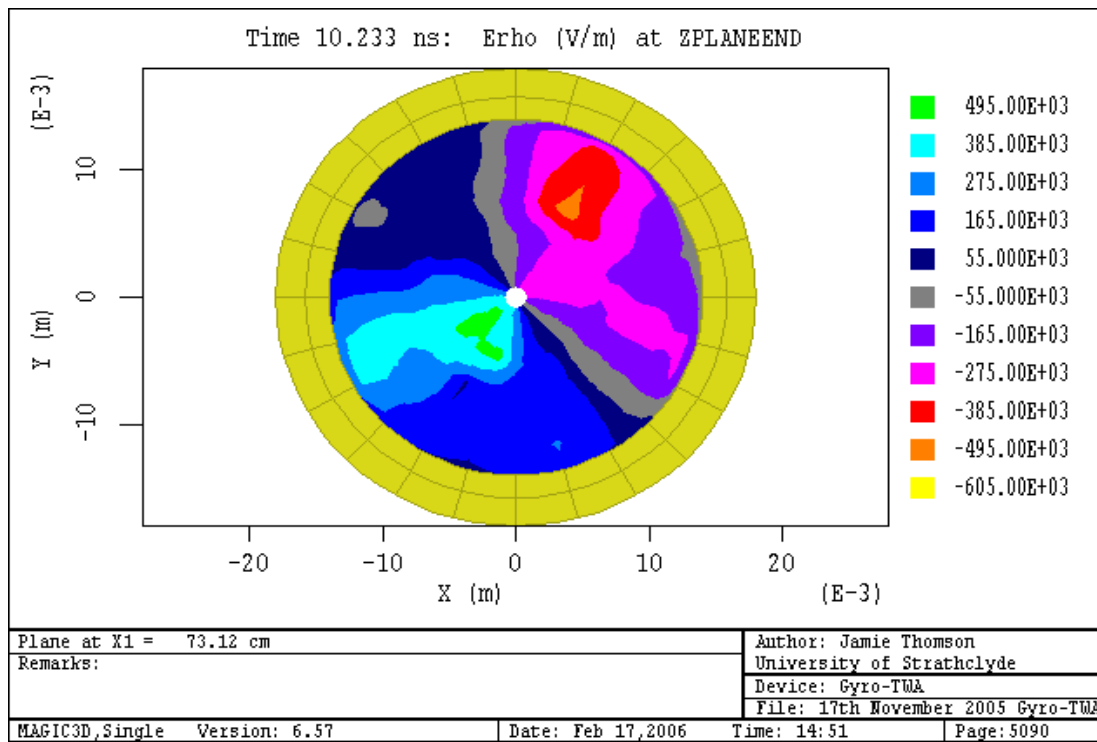


**Figure 5.23** Contour plot showing Erho component of electric field at the output end of the MAGIC gyro-TWA simulation.

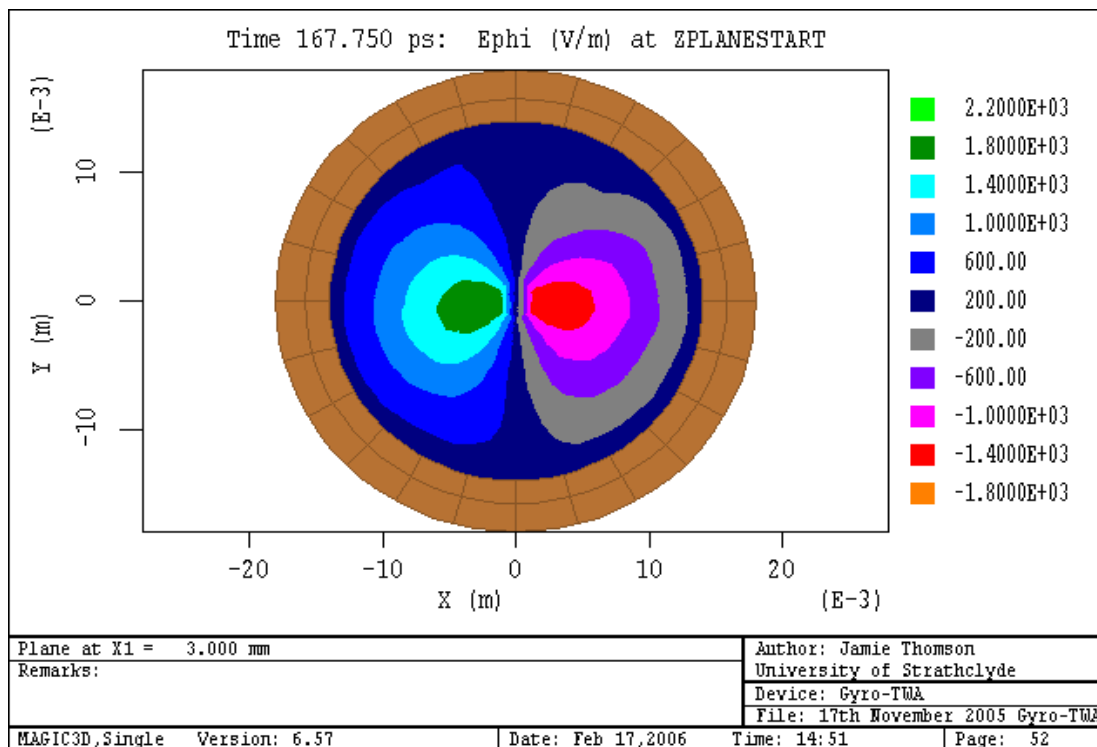


**Figure 5.24** Contour plot showing Ephi component of electric field at the input of the MAGIC gyro-TWA simulation.

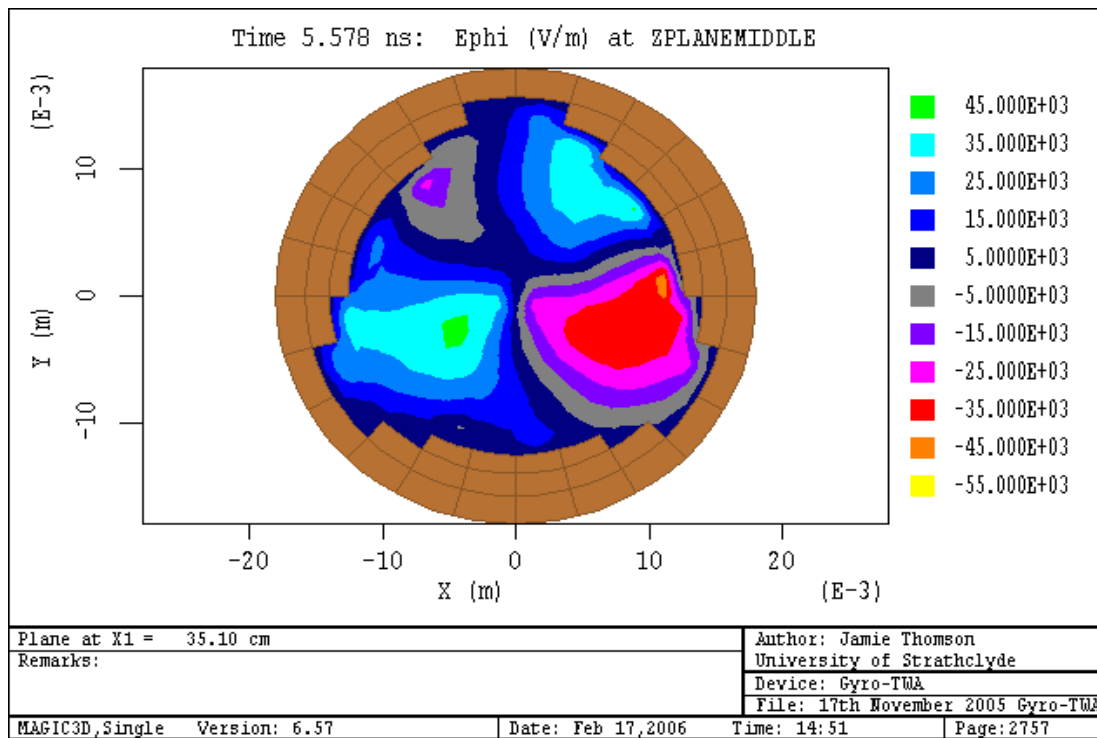


**Figure 5.25** Contour plot showing Ephi component of electric field at middle of the MAGIC gyro-TWA simulation.

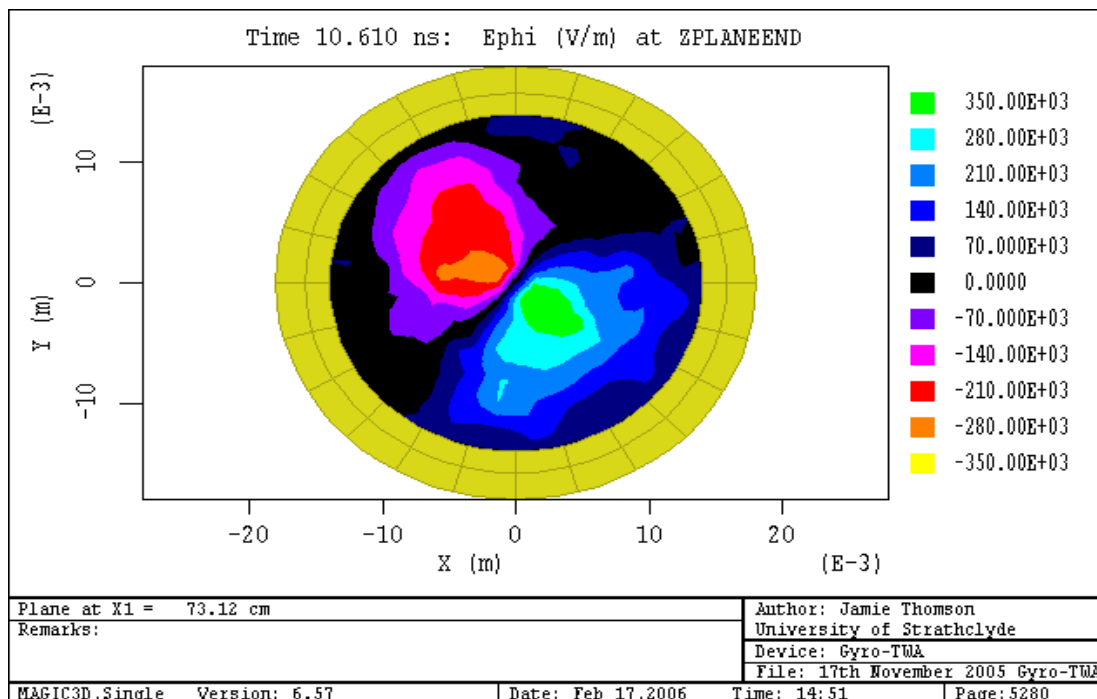


**Figure 5.26** Contour plot showing Ephi component of electric field at the output end of the MAGIC gyro-TWA simulation.

### **5.3.5 Comments on the Output of the Code**

To ensure that the simulation code had sensible output, a range of physical parameters were observed and these compared to what would be expected from theory. The output frequency of the radiation was in the bandwidth range predicted by theory and matched the drive frequency.

The expected coupling of the  $TE_{11}$  and  $TE_{21}$  modes was observed in the simulation as predicted by linear analysis which predicts coupling of the primary mode of the interaction region with the hybrid mode. It was observed that the particles remained subluminal as would be expected from basic physics. Also, very importantly energy conservation was observed.

### **5.4 Modelling of Linear Gain**

The linear gain was modelled numerically using a MAPLE code which was written especially to calculate values of  $h$  (the normalised axial wavevector) for a given  $\Delta$  (Refer to Chapter 4). Note that only the imaginary part of the complex roots of the equations were of use for the purposes of this model. Once obtained, the MAPLE code would write these values to a text file in order for them to be input to Excel. By inspection of these results, it was possible for the relevant linear gain of the instability to be calculated and plotted.

#### **5.4.1 Results**

The MAPLE code displayed plots to aid design and adjustment of parameters at three distinct stages. Firstly, the coupled waves themselves were plotted as in Figure 5.27 overleaf. Next, the electron beam dispersion was plotted along with these coupled waves so that it was possible for one to adjust the matching between the helically corrugated waveguide and electron beam dispersion. This is shown in Figure 5.28 with the waveguide and electron beam dispersions being the second bottom and bottom lines respectively.

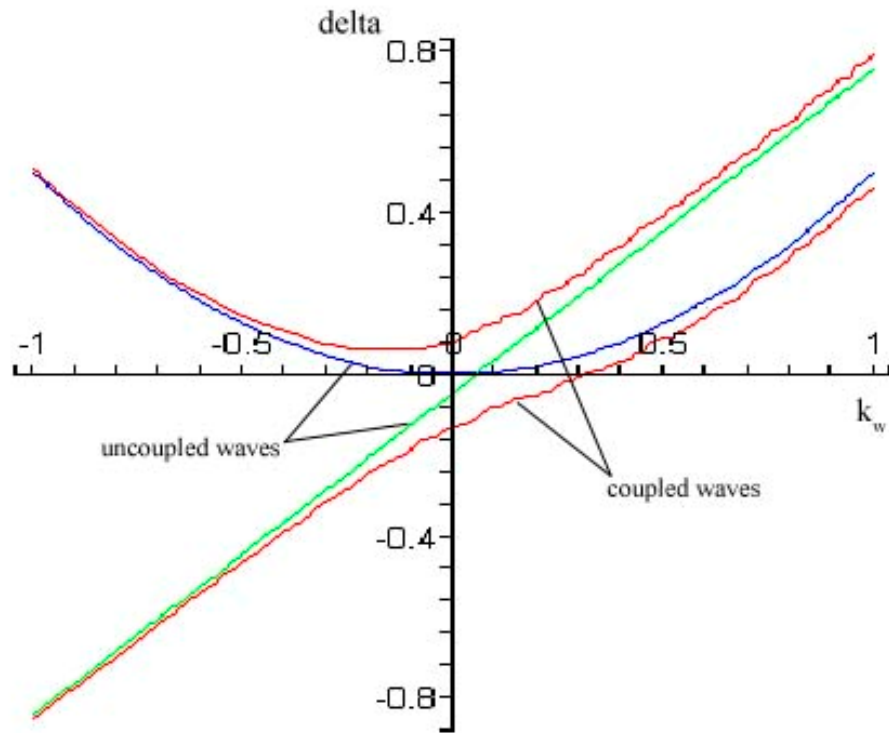


Figure 5.27 Plot of coupled waves produced by MAPLE code.

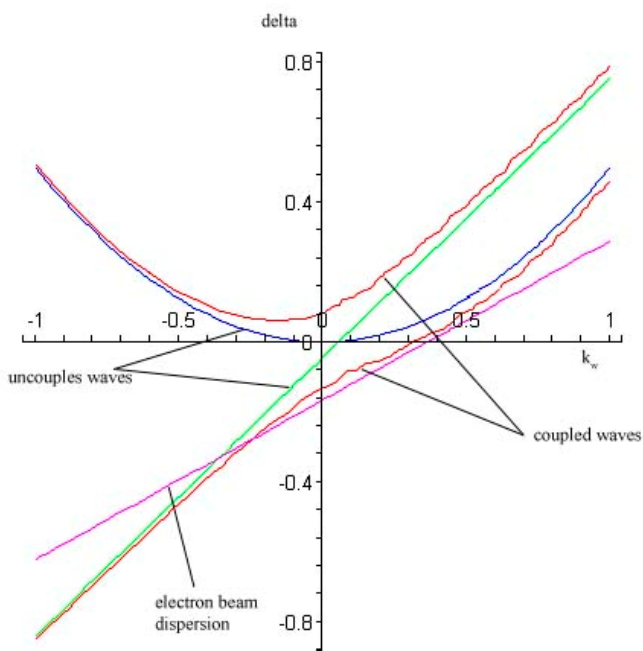


Figure 5.28 Plot of coupled waves with beam dispersion added as output by MAPLE code.

Figure 5.28 shows the solutions for the fifth order dispersion equation (Equation 4.5).

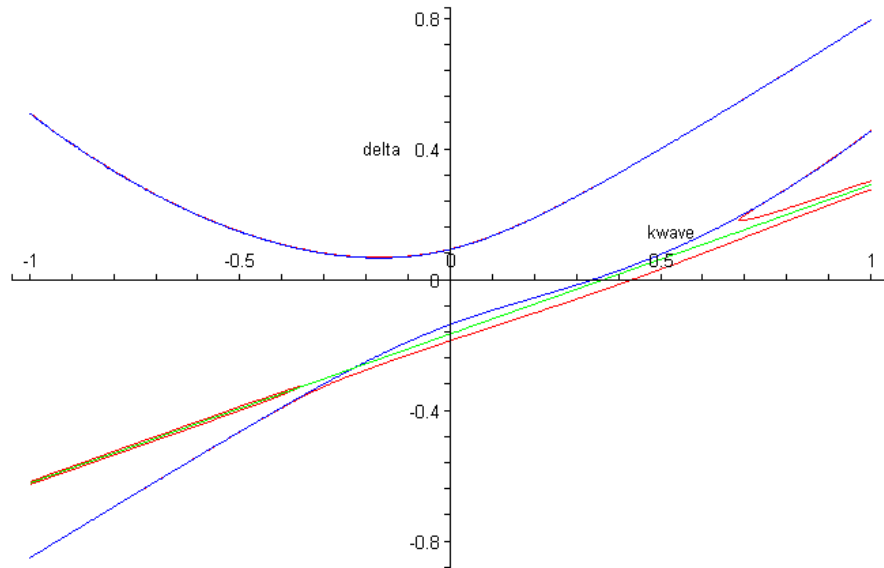


Figure 5.29 Plot of the solutions (red) of the fifth order equation from MAPLE code.

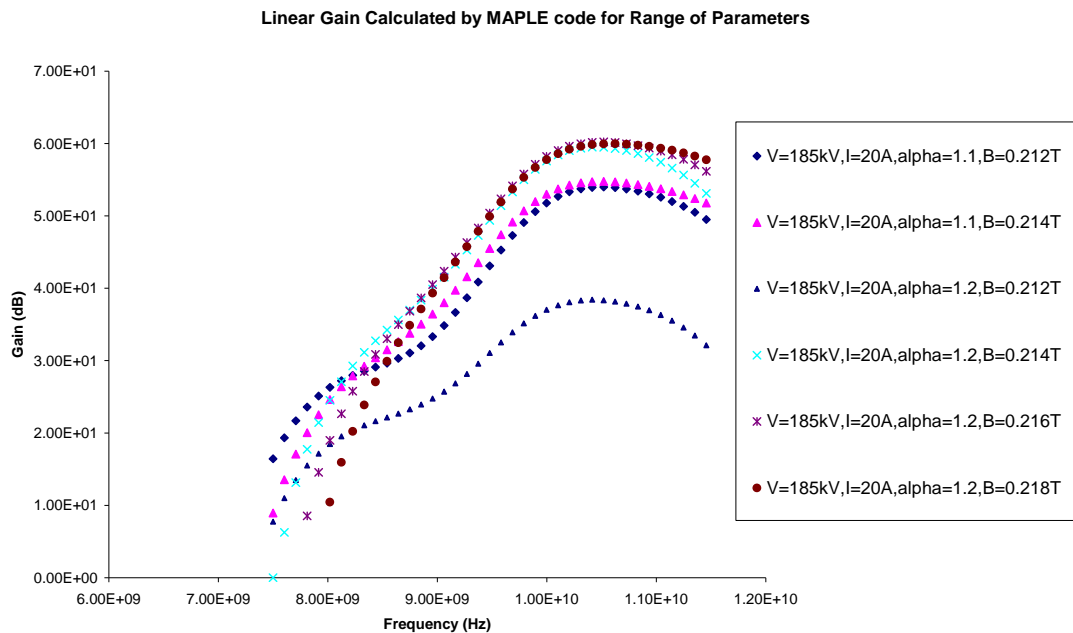
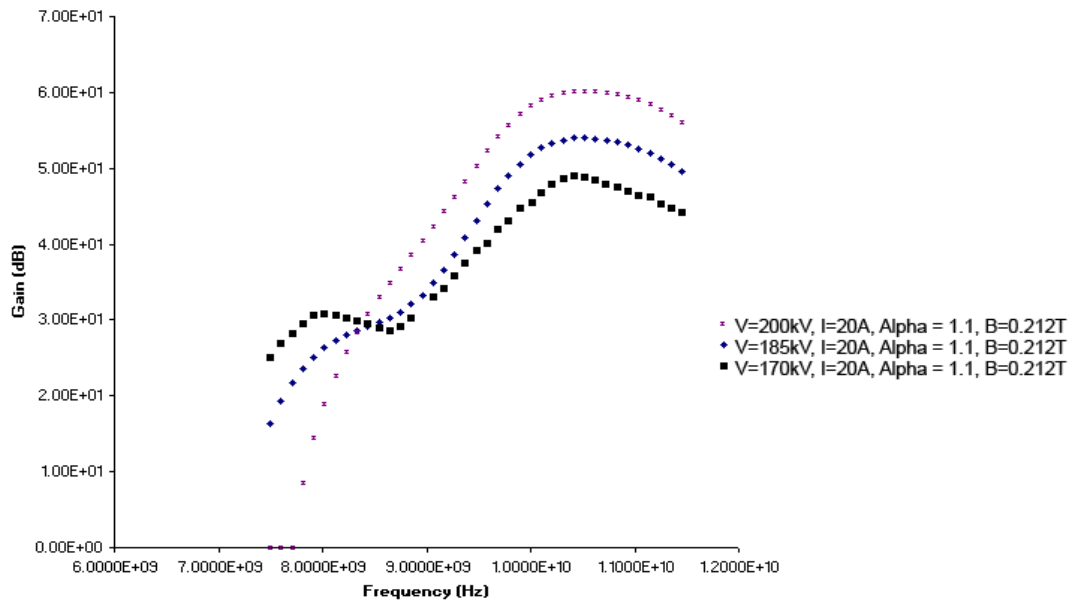


Figure 5.30 Linear gain as calculated by MAPLE code from the imaginary parts of the complex roots for the fifth order dispersion relation for a range of parameters.





**Figure 5.31 Linear gain as calculated by MAPLE code from the imaginary parts of the complex roots for the fifth order dispersion relation for a range of parameters (with variation in voltage).**

The variation of the linear gain behaviour with changing B fields and  $\alpha$  was to be expected as the system is sensitive to these parameters as adjustment of these would result in an alteration of the detuning. It was found that through careful adjustment of B or  $\alpha$  (and sometimes both) it was possible to broaden the gain curves. Increasing the detuning would cause a dip in the centre of the gain curve which – with further reduction of these parameters – became two distinct peaks with a prominent dip between. The reason for the adjustment of these values from the experimental estimates and the values used in the computer simulations was two-fold: Firstly it was possible that the beam parameters recorded from the experiment displayed some inaccuracies and so it was interesting to see the effects of slight variations in the parameters on the linear gain behaviour. Secondly, the linear theory is obviously a small signal approximation in any event. It is also based on the approximate perturbation theory for the wave dispersion, where the uncoupled waves have been reduced to a line and a parabola instead of a hyperbola to make the mathematics treatable. It is therefore not unreasonable to have slight variations in the optimum beam parameters from this model.

## **Chapter 6. Comparison of Results**

## **6.1 Waveguide Dispersion Theory**

As has been previously mentioned, in order to further understanding and to assist in the design of new gyro-TWA experiments and helically corrugated waveguide design, some novel new methods were developed utilising numerical and analytical methods to predict the behaviour of these systems. The present section briefly outlines how certain results were obtained, but more importantly compares these to those obtained from a benchmark experiment that was carried out in the year 2000.

### **6.1.1 Modelling**

Results presented here from modelling were obtained by three previously described methods – from the MAGIC PIC code (simulations for both the dispersion characteristics and the gyro-TWA simulation which allowed prediction of dispersion characteristics and key experimental parameters), from a new MAPLE code (which allowed the prediction of linear gain for the final system and also experimental parameters), and an MS Excel sheet which utilised an approximation to solve perturbation theory for given parameters.

### **6.1.2 Measurement**

The results obtained from physical measurements (other than the experimental results of an earlier amplifier experiment) were all obtained using a novel method which allowed one to measure the dispersion characteristics of a short section of helically corrugated waveguide using a Vector Network Analyser and some processing in MS Excel.

The amplifier experiment itself consisted of the aforementioned apparatus (refer to Chapter 4) and various diagnostics were employed in order to obtain measurements of various microwave parameters such as gain, efficiency and various frequency parameters. This section presents the results obtained from the experiment and also discusses them in some more detail.

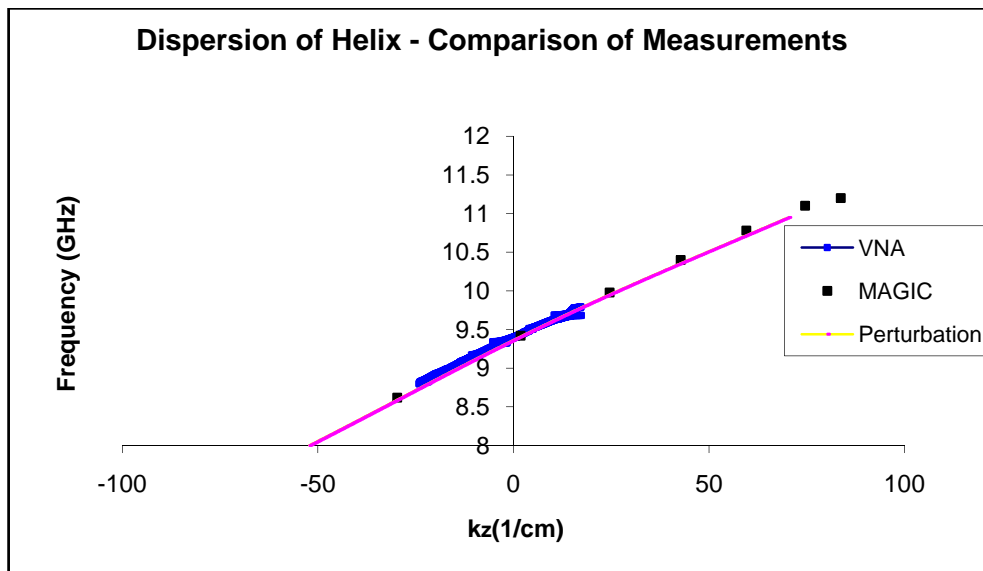


**Figure 6.1 Comparison of perturbation theory, MAGIC code and VNA measurement method of dispersion of helically corrugated waveguide (parameters as shown in Table 5.1).**

In order to check the validity of the MAGIC code method of obtaining the dispersion characteristics, a comparison was made between results from these and the predictions made by perturbation theory with the measurements obtained by the VNA. As perturbation theory only holds for small corrugation depths, and due to the fact that results from the three methods were in reasonable agreement, it can be concluded that the corrugation depth of the waveguide measured and modelled here (0.22cm) was sufficiently small for perturbation theory to accurately predict the dispersion. This highlights the importance of the methods developed in this thesis as one can never be certain that the corrugation depth is sufficiently small for perturbation theory to be valid, but by utilising these other codes this can always be checked and where perturbation theory is not longer valid, the MAGIC code (and also the VNA method of measurement) will still obtain accurate results.

## **6.2 Measurement of Microwave Output from Amplifier**

The following results were obtained utilising various microwave diagnostics to measure such important parameters as the microwave output power from the gyro-

TWA experiment. Descriptions of the various devices used for diagnostics are included in the preceding chapter.

Note that all results were obtained using the following experimental parameters:

Helix parameters: As shown in Table 5.1

Input Drive of up to 1kW

Beam Voltage = 185kV

Beam Current = 20A

$\alpha = 1.1$

$B = 0.21\text{T}$

### 6.2.1 Gain

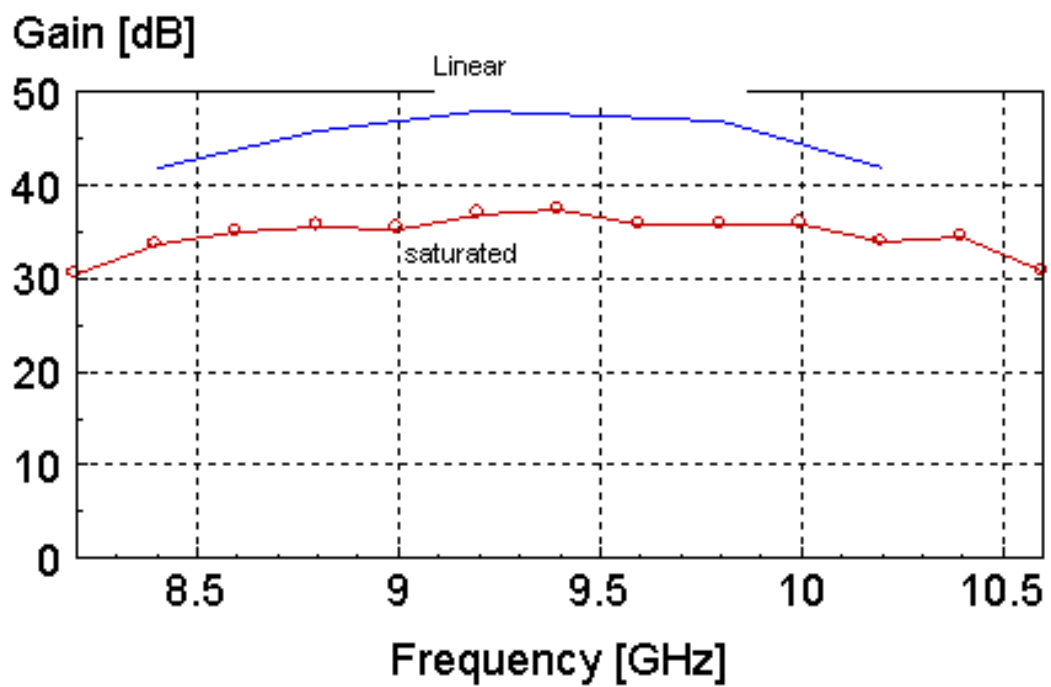
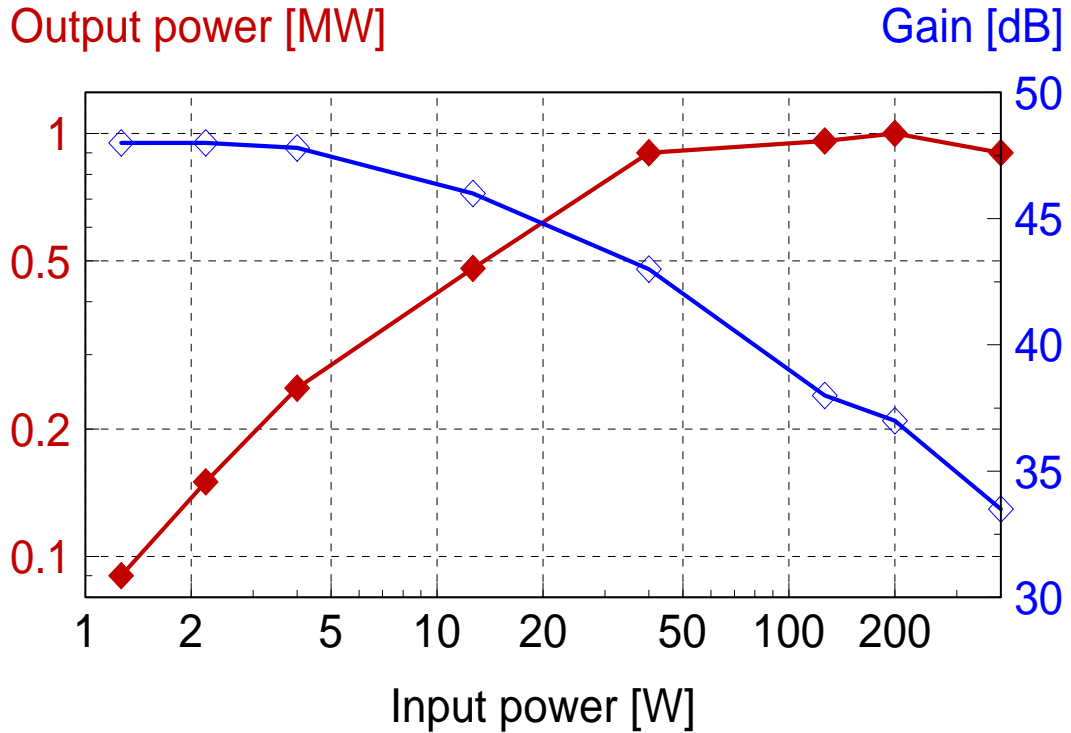


Figure 6.2. This plot shows the variation of saturated gain with frequency as well as the corresponding variation of linear gain with frequency (where linear gain is the solid line).

In Figure 6.2 the variation of saturated and linear gain with frequency obtained from experimental measurements obtained are plotted. Peak saturated gain was found to be approx. 37dB at around 9.4GHz with peak linear gain approx. 47dB. The gain was observed to be relatively flat over a bandwidth of around 2.5 GHz.



**Figure 6.3 Variation of gyro-TWA output power as a function of input power at 9.2GHz**

The experiment input power had been sufficient to saturate the CRM interaction. This can be seen in Figure 6.3, where the output power is plotted against the input power at an operating frequency of 9.2 GHz. The characteristic roll-off of power that is associated with the saturation mechanism can be clearly seen here. Peak power of approx. 1MW was achieved with an input drive power of 200W. This was a gain of approx. 37dB.

Figure 6.4 shows the effect of variation of the interaction length on the gain of the system. It should be noted that the origin for interaction length measurement was taken to be the start of the input taper to the helically corrugated waveguide.

The effect of saturation can also be clearly seen here as we move towards the end of the helically corrugated waveguide. From the results, it's clear that as saturation occurred at approx. 65cm along the interaction region (a peak gain of ~37dB), the extra helix length (beyond 65cm on this diagram) was perhaps not required.

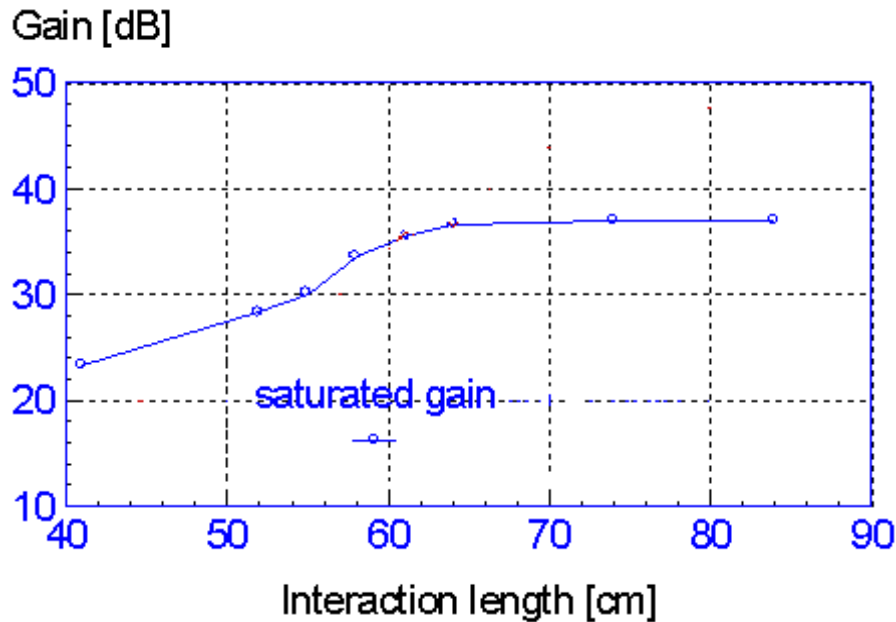


**Figure 6.4** The variation of saturated and linear gain as a function of interaction length for year 2000 experiment.

### 6.2.2 Efficiency

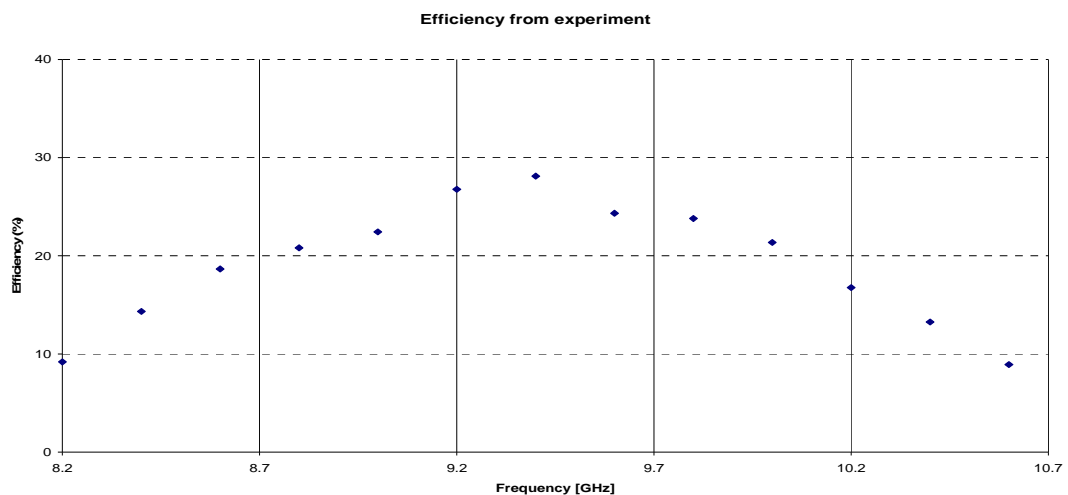


**Figure 6.5** This plot shows the measured saturated efficiency as a function of frequency.

The percentage efficiency was calculated using measurements from the aforementioned experiment and this is shown in Figure 6.5. It should be noted that the larger variation in these values compared to the gain etc. is due to the fact that these are not plotted on a LOG scale here. Peak efficiency was found to be around  $\eta = 29\%$ .

### **6.3 Gain, Efficiency and Bandwidth Results Compared**

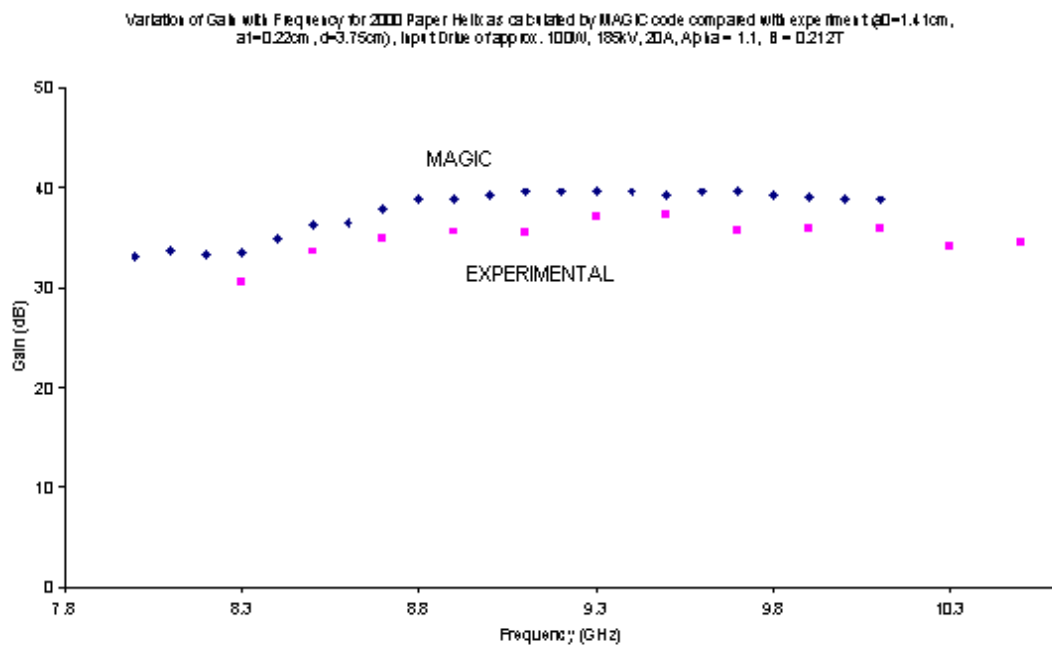


**Figure 6.6 Comparison of saturated gain calculated by MAGIC and measured in 2000 experiment.**

In Figure 6.6 the gain calculations are compared to measurements obtained in a benchmark gyro-TWA experiment carried out in the year 2000. It can be seen that the saturated gain from the MAGIC code was  $\sim 38\text{dB}$  with the comparable experimental gain  $\sim 37\text{ dB}$ . The saturated gain obtained in the experiment was slightly lower than that obtained by the MAGIC simulation. This was probably to be expected as the simulation was really an ideal model i.e. with idealised electron beam source and also the simulation could not take into account the use of the 10dB surface-loss sever in the experiment, so the results were found to be in fair agreement



when taking this into account.

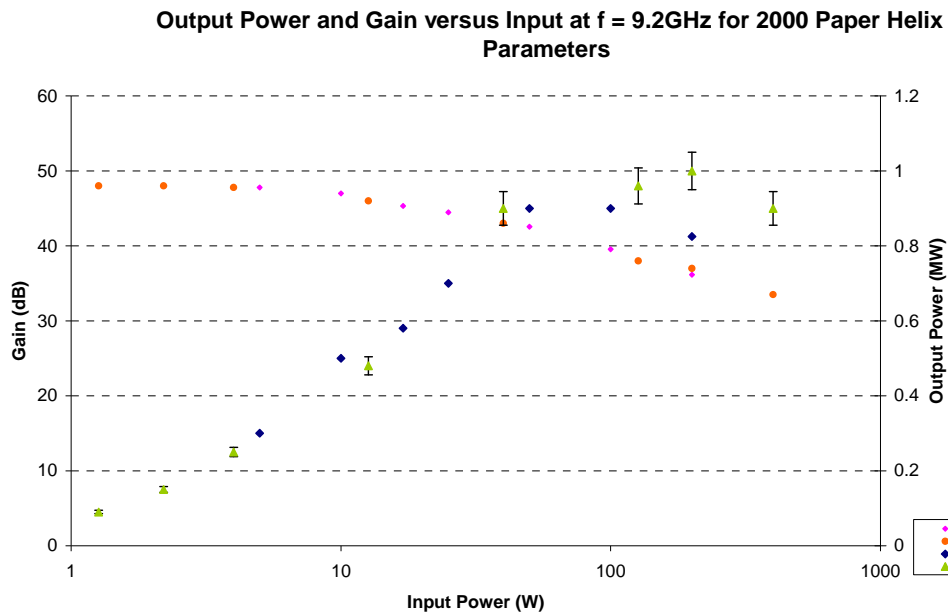


**Figure 6.7 Output power and gain versus input power at an operating frequency of 9.2GHz for experiment and as predicted by theory.**

In Figure 6.7 a comparison of the experimental results and theoretical predictions of the output power and gain versus input power is made. In the lower input power range (below 50W) the experimental results and theoretical predictions obtained using the MAGIC code were in reasonable agreement. In the higher input power region there is some mismatch between the experimental and theoretical values – for MAGIC saturation occurs at an input power of  $\sim 150\text{W}$ , while the experiment reached saturation around the 200W. This is where the characteristic ‘roll-off’ of gain occurs due to saturation (phase trapping in this case). The simulations appear to saturate at a slightly lower efficiency and input power than the experiment. Both the experiment and MAGIC calculations showed linear gain  $\sim 47\text{dB}$  which was comparable with the results from linear theory (Section 5.3). Peak output power predicted by MAGIC was 900kW while for the experiment the value was closer to 1MW. However there was a 10% uncertainty in the experimental data.#

One of the most important and oft-quoted performance indicators of any amplifier is its efficiency. In Figure 6.8 results from the benchmark experiment carried out in

2000 were used to compare to the numerical predictions obtained using the MAGIC code.

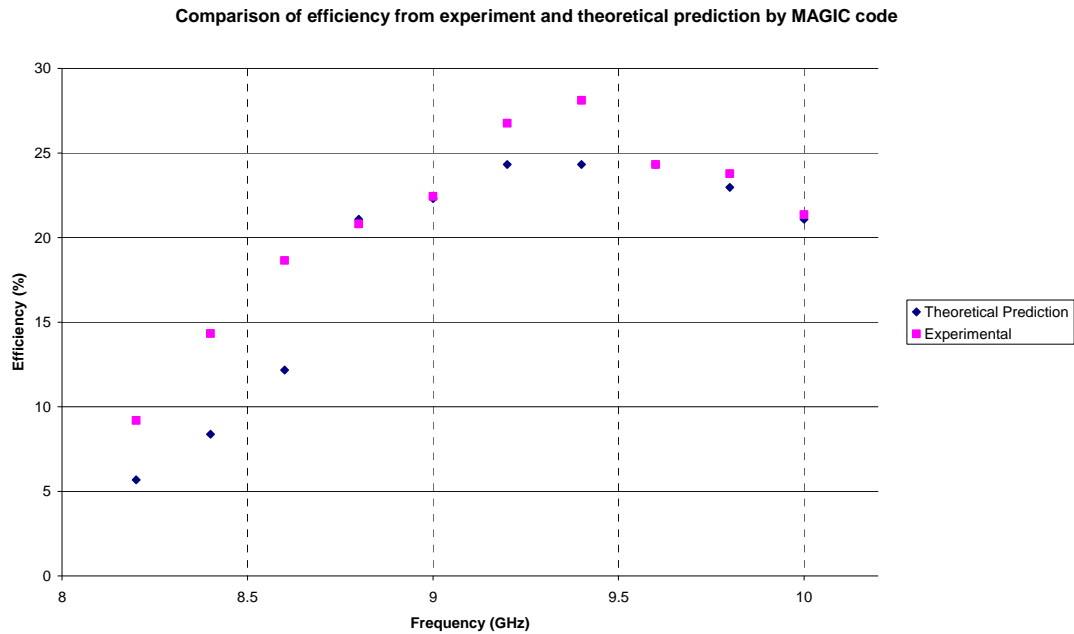


**Figure 6.8 Comparison of experimental and theoretically predicted efficiencies for the gyro-TWA experiment.**

It was observed that the theoretical predictions for the most part exceeded the experimental measurements which are as to be expected from the simulation. The overall trend of an efficiency increase up to around the 9.2 GHz (approx.) point before a roll-off in efficiency towards the higher frequency range was observed in both simulation and in experiment. This will be due to variations in coupling parameters and detuning.

When analysing the performance of the gyro-TWA experiment, it was helpful to gain an insight into the variation of output power with the length of the interaction structure in order to study the gain behaviour. Figure 6.9 shows predictions from the MAGIC code (refer to Section 5.1.8) compared with experimental results. It was observed that the predictions were higher than the measurements obtained by experimental measurement – for example comparing two similar interaction lengths, MAGIC gave 34dB of gain at a helix length of 0.46m whereas the experiment yielded a gain of 28dB at 0.525m.

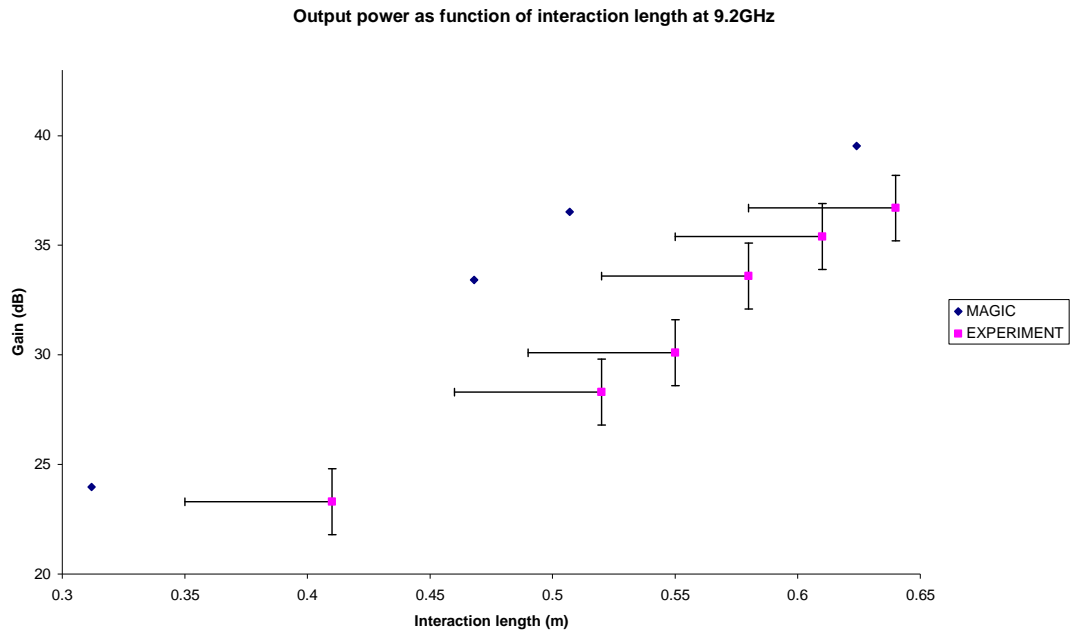


**Figure 6.9 Output power as a function of interaction length – comparison between predictions from MAGIC code and experimental measurements.**

This was to be expected as the MAGIC simulation deals with an ideal case and so does not allow for the inaccuracies which can occur under experimental conditions. Most importantly, the MAGIC code utilises an ideal electron beam source and this is obviously not possible to replicate in experiment. It was noted however that the overall trend of the data obtained from the MAGIC code matched that of the experiment i.e. the gradients of the data sets showed reasonable agreement, showing an increase of gain with interaction length. It is likely that some ‘zero-offset’ discrepancy between the origin chosen for the experimental data and the numerical data may be responsible. Also, the MAGIC code does not include the microwave sever.

The error bars in Figure 6.9 illustrate the fact that a horseshoe magnet was used to dump the electron beam in the experiment. As it was placed some distance from the tube axis significant fringing may result in the beam being disrupted upstream from the magnet location. This would give rather strong agreement with the numerical simulation as indicated by the error bars in Figure 6.9.’

#### **6.4 Frequency Measurements**

The output and input frequencies were measured by an X-band waveguide cut-off filter. These were found to be in reasonable agreement for all presented data.

## **Chapter 7. Conclusion and Future Work**

## **7.1 Introduction**

In this chapter, the work presented in this thesis is reviewed, namely the design and implementation of a novel software suite allowing the design of a gyro-TWA experiment and the development of a new method for measuring the waveguide dispersion. The key findings in developing the various codes, as well as the advantages over existing methods are also discussed. Predictions from the codes were compared with a benchmark experiment to test the validity of the new software suite. At the end of the chapter, ideas for future work are briefly discussed.

## **7.2 Conclusions**

The research pursued in this thesis was aimed at the development of a software suite which would allow the prediction of all key parameters for the construction of a gyro-TWA experiment. Several codes were developed using the particle in cell (or PIC) code MAGIC and the mathematical package MAPLE. Any digital processing was carried out using custom-made MS Excel spreadsheets. The novel contributions made during this research are as follows:

1. Development of a MAGIC code to model the output of an electron beam which is readily transportable between MAGIC codes.
2. Development of a MAGIC code to model a gyro-TWA using imported electron beam data. This code allowed the prediction of gain, stability to oscillations, frequency measurement and other parameters.
3. The design of a MAPLE code which allowed prediction of the linear gain behaviour for a given set of electron beam and helically corrugated waveguide parameters.
4. The development and testing of a novel new method of measuring the dispersion characteristics of a short section of helically corrugated waveguide using a VNA.

These new codes combined with existing methods for predicting the waveguide dispersion (MAGIC code and a numerical method for solving perturbation theory) constitute an entire suite of design software for a gyro-TWA. This work resulted in a complete software suite which would allow the accurate prediction of all parameters and performance for a gyro-TWA experiment. Use of this code and the new VNA dispersion measurement method would not only result in reduction in time for the gyro-TWA experimental design process and save considerably on manufacturing costs, but would allow new ideas to be tried that would not otherwise have been contemplated with high confidence in the final experimental design.

### **7.2.1 Approximate prediction of dispersion by perturbation theory**

As has been previously explained (refer to Chapter 4), perturbation theory allows the prediction of the dispersion characteristics of a section of helically corrugated waveguides for sufficiently small corrugation depths. By using an approximation, it was possible to solve perturbation theory and obtain the dispersion for a helically corrugated waveguide with given parameters. The research pursued here suggested that this method may only be useful as a preliminary tool to gain some insight into helically corrugated parameters required to obtain the desired dispersion. This was due to the fact that the limit of the validity of this method i.e. the exact cut-off point at which the corrugation depth becomes too large for the method to work, is not well known. Also, it was noted that perturbation theory is itself an approximation, and by using the method presented here we add a further approximation (the cubic approximation). Thus, one could not be confident that this method would always give accurate predictions but is nonetheless a very useful step in gyro-TWA experimental design.

### **7.2.2 MAGIC code for prediction of dispersion**

In order to further refine the predictions of the important parameters required for the manufacture of the helically corrugated waveguide, a MAGIC code was used to simulate radiation passing through a section of the waveguide. By measuring the

rotation of the polarisation of radiation due to the helically corrugated waveguide, it was possible to obtain the dispersion characteristics. It was found that by taking the parameters found from solving perturbation theory numerically (refer to preceding section) and then using these to run this MAGIC simulation (which also models the geometry), it was possible to find a more accurate prediction of the dispersion characteristics. Hence, this method allowed further adjustment of parameters required to obtain the desired dispersion for input to the gyro-TWA simulation.

This particular MAGIC code had to be altered to relieve problems caused by phase matching at the PORTs. The MAGIC code requires the phase velocities at the input and output ports to be equal. This problem was overcome by the addition of large horns at the input and output sections, which meant that all phase velocities would be approximately equal to the velocity of light,  $c$ .

### **7.2.3 MAGIC code for simulation of electron beam**

A code was written using the PIC code MAGIC to simulate an axis-encircling electron beam. The code allowed one to simulate the propagation of a beam with specified parameters through a short smooth-bore section of waveguide and provided output particle and field data for use in further codes. Using plane waveguide (with same radius as the helically corrugated waveguide to be modelled) as opposed to helically corrugated waveguide would allow much faster generation of electron beam data. These data files could then be imported to a MAGIC code to directly input an axis-encircling electron beam. It was found that this was a much more efficient and faster way to input an electron beam to a MAGIC simulation. The main advantage though, was that by injecting this electron beam to a plane in a MAGIC simulation, one could also input radiation without problems previously observed (refer to Chapter 4).

### **7.2.4 MAPLE code for prediction of linear gain behaviour**

A novel new code was written for the mathematical package MAPLE which allowed the prediction of the linear gain characteristics of a given gyro-TWA experiment i.e.



the helically corrugated waveguide and the electron beam parameters. The code (refer to Appendix B) numerically solved linear gain theory for the helically corrugated waveguide. Use of this code allows the refinement of the parameters of both the helically corrugated waveguide and the electron beam prior to construction of the gyro-TWA experiment.

The predictions obtained from this code were compared to experimental results from experiment. They were found to be in reasonable agreement, given they are based on an approximate representation of the operating eigenwave.

### **7.2.5 MAGIC code for gyro-TWA simulation**

In order to check the parameters for both the electron beam and the helically corrugated waveguide, a MAGIC code was developed which would simulate the gyro-TWA. Particle and field data from an axis-encircling electron beam generated by a new MAGIC code and input to the simulation (refer to preceding section). TE<sub>11</sub> radiation was then injected at the input in order to allow beam-wave interaction to occur. By using inbuilt diagnostic commands in MAGIC and adapting them to monitor fields etc., it was possible to predict a number of important parameters. In particular, the output power could be measured and, as the input driving power was known, the gain characteristics of the amplifier could be studied as a function of frequency.

During the development of this novel new code, some problems had to be overcome. The main difficulty lay in the method used to insert both the radiation and to inject the electron beam. Several methods of generating both the electron beam and radiation were tried (refer to Chapter 4) but none produced satisfactory results. The solution to this problem was to create two distinct codes – one which simulates the electron beam and stores the data required to reproduce this in another MAGIC simulation and another which would have this electron beam injected and also input radiation using the DRIVER command. This method was found to allow correct

interaction of the electron beam and wave and thus resulted in accurate predictions of gyro-TWA experimental parameters.

Results from this simulation were compared to a benchmark experiment which was carried out in the year 2000 by University of Strathclyde (refer to Chapter 6). The predictions obtained using the MAGIC code was found to be in good agreement with the experimental results.

#### **7.2.6 Measurement of dispersion characteristics using VNA method**

A novel new method for measurement of the dispersion characteristics of a section of helically corrugated waveguide using a VNA was developed and tested. This method allowed a more accurate measurement of the helically corrugated waveguide dispersion than was previously possible. Prior to this, Scalar Network Analyser (SNA) measurements were relied upon but it was found that the VNA method had some major advantages. The SNA was only capable of measuring the frequency and amplitude of the signal, whereas the VNA could also make phase measurements. Calculation of the dispersion was greatly dependent on knowledge of the number of whole rotations of the mode propagating through the helically corrugated waveguide. For the SNA case, many periods of waveguide were required for a sufficiently accurate measurement and so larger sections had to be machined – increasing costs and design times considerably. The VNA method was found to give accurate results with much shorter test-pieces of the waveguide and with a greater number of points of measurement due to its phase measuring capabilities.

This validity of this method was verified by comparison to dispersion characteristics calculated by the MAGIC code and by perturbation theory. It was found to be in good agreement with these predictions. It also agreed well with the SNA results to within the limits of which these could be relied upon.

#### **7.3 Discussion on Application of New Code**

The development of this suite of codes was seen to have some important benefits.

The demonstrated use of coupled mode dispersion theory could be utilized to save much time in the experimental phase by allowing one to predict the ideal geometrical parameters of the helically corrugated waveguide, detuning, pitch angle, energy and current, thus it is possible to minimise adjustments of said parameters throughout the experiment. The VNA measurement technique pioneered here allows accurate measurement of helically corrugated waveguide dispersion with only a short section easily fabricated on a mill. This ensures the correct geometry is chosen before an expensive large scale process is used to make the entire amplifier waveguide.

The non-linear simulation method pioneered in this thesis also clearly demonstrates the ability to optimize the pitch angle beam current and energy with a much greater accuracy than was previously possible. For instance, the linear gain of the 2000 Experiment could have been reduced by shortening the interaction region (helically corrugated waveguide) to give better stability to oscillations. As the 2000 experiment was very effectively experimentally optimised, the code could not have improved greatly upon performance but it certainly would have reduced the experimental time and negated work performed to tweak each variable to obtain the best performance. It is important to note that the 2000 experimental results [Bratman et al 2000] derived from a six year research programme including one prototype experimental stage [Denisov et al 1998]. The work presented here could have cut this phase down by 1/3 to 1/2. Thus it is a tool of extreme importance in the pre-experimental design period. The experiments used longer interaction structures than were actually necessary. This measure had originally been taken since the gain of the gyro-TWA experiment was not accurately known prior to the assembly of the apparatus. Since the work in this thesis has clearly demonstrated a method for prediction of the linear gain and saturation behaviour of a gyro-TWA experiment, this would have allowed the use of shorter interaction structures. The benefits of this are clear - from a practical viewpoint the experiment can be assembled in shorter time with greater confidence in its ultimate performance. This will be critical in future attempts to create commercial 'real world' amplifiers. The interaction length increased the tendency of the amplifier to oscillation which could have been averted with the enhanced predictive capability of these simulations. It may also then have been

possible to increase the current or alpha and hence the power without risking the possibility of oscillation occurring, whilst removing some of the losses included in the experiment to stabilize oscillation.

#### **7.4 Future Work**

Several improvements could be made to the software suite to further enhance its use. A study of the effects of varying grid densities and observing the change in accuracy of the results for the MAGIC codes presented here would prove to be a useful insight. Most importantly, adjustments in the grid resolution of the MAGIC representation of the helically corrugated waveguide could well provide results with a higher degree of accuracy. Primarily this would be achieved by using the MAGIC code for the prediction of the dispersion characteristics and altering the grid resolution while recording such parameters as the resultant increase in runtime and the corresponding effects on the accuracy of the predictions. This grid density could then be carried across to the gyro-TWA MAGIC code and would thus reduce in either a more efficient or more accurate code.

The MAPLE code presented here obtained predictions of the linear gain characteristics of a gyro-TWA system by solving the corresponding linear theory. At present, this theory used the cubic approximation, and so it could be further modified by altering the code to solve directly the full double hyperbolic.

It would be most advantageous to utilise the software suite developed here to design an entirely new gyro-TWA experiment and subsequently make a comparison of the predictions and experimental results.

#### **7.5 Summary**

New experimental and numerical methods for the measurement and prediction of key parameters of gyrotron TWAs have been demonstrated and proven\*. These

---

\* These include accurate measurements of the dispersion of short sections of helically corrugated waveguide, calculations of the linear and non-linear gain, bandwidth and the efficiency of the amplifier. The results have been checked against existing benchmark experimental data.

techniques can be used for accurate prediction of the performance of such amplifiers resulting in more efficient use of valuable and limited experimental resources.

## **Appendix A. Computer Codes**

## MAGIC Code for Electron Beam Export

```
!=====
=
HEADER ORGANIZATION "University of Strathclyde" ;
HEADER Author      "Jamie Thomson" ;
HEADER DEVICE "Gyro-TWA" ;
!=====
=
ON = 1 ;
OFF = 0 ;
IDISPLAY = ON ;
IFREQUENCY = ON ;
IVECTOR = ON ;
IVIEW = On ;
IDUMP = On ;

GRAPHICS PAUSE ;
GRAPHICS PAUSEOFF TSYSS$FIRST ;

SYSTEM CYL ;

        CYL_LENGTH = 3_CM;
        CYL_RADIUS = 2_CM;
! Mesh resolution parameters.
        DELTA.Z = 0.5_MM;      ! Axial resolution      d/18
        DELTA.R = 1_MM;        ! Radial resolution    a1/4
        DELTA.PHI = 2.PI/23;   ! Azimuthal Resolution  2.pi/60

! Define the confining shell.

        POINT3 SHELL.LO 0.0,CYL_RADIUS,0.0PI ;
        POINT3 SHELL.HI CYL_LENGTH,+DELTA.R+CYL_RADIUS,2PI ;
        VOLUME SHELL CONFORMAL SHELL.LO SHELL.HI ;;

! Define Endcap 1 (DIODE END ENDCAP)
        ENDCAPRAD=0.02;
        POINT ENDCAP1.BASE.PT -0.01,0,0;
        POINT ENDCAP1.TOP.PT 0.0,0,0;
        VOLUME ENDCAP1 CYL ENDCAP1.BASE.PT ENDCAP1.TOP.PT
        ENDCAPRAD;

        POINT3 OUTLET.LO 2.9_CM,0.0,0.0 ;
        POINT3 OUTLET.HI 2.9_CM,2_CM,2pi ;
        AREA3 OUTLET CONFORMAL OUTLET.LO OUTLET.HI;

! MARK the objects for AUTOGRID and create the grid.
        MARK SHELL X1 SIZE Delta.Z ;
```

```

MARK SHELL X2 SIZE Delta.R ;
MARK SHELL X3 SIZE Delta.PHI ;

MARK ENDCAP1 X2 size delta.r;
MARK ENDCAP1 X3 SIZE delta.phi;
MARK ENDCAP1 X1 SIZE delta.z;

MARK OUTLET X2 size delta.r;
MARK OUTLET X3 SIZE delta.phi;
MARK OUTLET X1 SIZE delta.z;
AUTOGRID ;

! Add uniform confining axial magnetic field.
Confinement_B=0.2_TESLA;

FUNCTION B_axial(z,r) = Confinement_B ;
PRESET B1ST FUNCTION B_axial ;

Beam_current = 1Amps;          ! Beam current
Beam_voltage = 185KiloVolts;   ! Beam energy
Beam_alpha = 1.2 ;             ! Pitch Factor
electronchg = 1.6021e-19 ;     ! Electronic Charge
electronmass = 9.10956e-31 ;   ! Electronic Mass
clight = 3e8 ;                 ! Speed of light
Gamma = 1 + (electronchg*Beam_voltage)/(electronmass*clight**2); ! LF Factor
Velocity_all = clight*(SQRT(1-(1/(gamma**2)))); ! Total v
Velocity_axial = Velocity_all/(SQRT(1+Beam_alpha**2)); ! v//
Velocity_transverse = Velocity_axial * Beam_alpha; ! v_||
GuidingCenter_radius = 0.00cm ; ! Guiding center radius
!*****
! Assign material properties, boundary conditions, and drive applications.

CONDUCTOR SHELL MATERIAL COPPER SOLID TRANSPARENCY 50;
CONDUCTOR ENDCAP1 MATERIAL GOLD SOLID TRANSPARENCY 95;

! Define inlet port plane

POINT3 INLET.LO 0.0,0.0,0.0 ;
POINT3 INLET.HI 0.0,2_CM,2pi ;
AREA3 INLET CONFORMAL INLET.LO INLET.HI ;

! Define outlet port plane

POINT3 OUTLET2.LO 3.0_CM,0.0,0.0 ;
POINT3 OUTLET2.HI 3.0_CM,2_CM,2pi ;
AREA3 OUTLET2 CONFORMAL OUTLET2.LO OUTLET2.HI;

PORT INLET POSITIVE;

```



PORT OUTLET2 NEGATIVE;

DrvFreq=9.5GHz;  
maxwell biased; ! changed from high\_q  
Period = 1./DrvFreq ;  
KPERIOD = period/sys\$dttime ;  
dttime =period/kperiod ;  
time\_step dttime ;

! =====emission model for generating the electron beam.

FUNCTION CURRENT(T) = BEAM\_CURRENT ;  
P\_axial = Gamma\*Velocity\_axial ;  
P\_transverse = Gamma\*Velocity\_transverse ;  
delta\_emit = dttime \* 1.c \* velocity\_axial ;  
POINT3 GUIDING\_CENTER 0,0,0.0;  
EMISSION GYRO Current Confinement\_B P\_axial P\_transverse  
GUIDINGCENTER\_RADIUS  
guiding\_center;  
EMIT gyro ENDCAP1 ;  
observe eMITTED eNDCAP1 eELECTRON cCURRENT ;

OUTPWG.ZMAX = 20.00\_CM;  
POINT OUTPUTCENT.PT 20\_cm,0,0;

! =====Diagnostics section

!Define lines and planes for diagnostics

LINE ZLINE CONFORMAL ENDCAP1.TOP.PT OUTPUTCENT.PT;

ZBY3 = OUTPWG.ZMAX ;

Zstart = 0.1\_cm;

Zmiddle = 1.5\_CM;

Zend = 2.9\_cm;

RBY3 = 0 ;

TBY3 = 0 ;

AREA ZPLANESTART CONFORMAL Zstart,SYSSX2MN,SYSSX3MN,Zstart  
SYSSX2MX,SYSSX3MX ;

AREA ZPLANEmiddle CONFORMAL Zmiddle,SYSSX2MN,SYSSX3MN,Zmiddle  
SYSSX2MX,SYSSX3MX ;

AREA ZPLANEend CONFORMAL Zend,SYSSX2MN,SYSSX3MN,Zend  
SYSSX2MX,SYSSX3MX ;

AREA TPLANE CONFORMAL SYSSX1MN,SYSSX2MN,TBY3  
SYSSX1MX,SYSSX2MX,TBY3 ;

!Define timers for diagnostics

TIMER BTIME DISCRETE 1;

tIMER eARLY DISCRETE 1;

tIMER eARLY1 DISCRETE 11;

Graphics PauseOff Early1 ;

Graphics PauseON Tsys\$last ;

```
Timer ShowFrames1 periodic 20 300000 20 ;
Timer ShowFrames3 periodic 100 300000 100 ;
```

```
!Define required range and observe outputs
```

```
RANGE FIELD B1ST ZLINE BTIME;
      POINT3 INLET2.LO 1.0CM,1cm,0.0 ;
      POINT3 INLET2.HI 1.0CM,2_CM,2pi ;
      AREA3 INLET2 CONFORMAL INLET2.LO INLET2.HI ;
```

```
PHASESPACE AXES X2 X3 eARLY ;
PHASESPACE AXES X1 X2 TSYS$LAST dump ; ! ;
```

```
PHASESPACE AXES X1 X2 ShowFrames1 Nodump ;
VIEWER ShowFrames3 ;
```

```
VIEWER TSYS$LAST ; !;
```

```
PHASESPACE AXES X1 KE TSYS$LAST AXIS X SYSS$X1MN SYSS$X1MX ;
PHASESPACE AXES X1 KE showframes3 AXIS X SYSS$X1MN SYSS$X1MX ;
PHASESPACE AXES X2 X3 eARLY ;
PHASESPACE AXES X1 X2 TSYS$LAST dump ; ! ;
```

```
runfor = 1_nanoseconds;
EXPORT OUTLET NEGATIVE elecbeam2 binary ;
duration runfor;
DISPLAY ;
START ;
```

### **MAGIC Code for IMPORT of electron beam data and gyro-TWA simulation**

```
!=====
=====
HEADER ORGANIZATION "University of Strathclyde" ;
HEADER Author      "Jamie Thomson" ;
HEADER DEVICE "Gyro-TWA" ;
!=====
=====
```

```
ON = 1 ;
OFF = 0 ;
IDISPLAY = ON ;
IFREQUENCY = ON ;
IVECTOR = ON ;
IVIEW = On ;
IDUMP = On ;
```

```
GRAPHICS PAUSE ;
GRAPHICS PAUSEOFF TSYS$FIRST ;
```

SYSTEM CYL ;

CYL\_LENGTH = 65\_CM;

CYL\_RADIUS = 1.4\_CM;

! Mesh resolution parameters.

!DELTA.Z = d/25; ! Axial resolution d/18

!DELTA.R = a1/3; ! Radial resolution a1/4

!DELTA.PHI = 2.PI/24; ! Azimuthal Resolution 2.pi/60

DELTA.Z = 0.5\_MM; ! Axial resolution d/18 0.5\_MM

DELTA.R = 1\_MM; ! Radial resolution a1/4 1\_MM

DELTA.PHI = 2.PI/23; ! 2.PI/23

! Define the confining shell.

POINT3 SHELL.LO 0.0,CYL\_RADIUS,0.0PI ;

POINT3 SHELL.HI CYL\_LENGTH,+DELTA.R+CYL\_RADIUS,2PI ;

VOLUME SHELL CONFORMAL SHELL.LO SHELL.HI ;

! Define Endcap 1 (DIODE END ENDCAP)

ENDCAPRAD=0.014;

POINT ENDCAP1.BASE.PT -0.01,0,0;

POINT ENDCAP1.TOP.PT 0.0,0,0;

VOLUME ENDCAP1 CYL ENDCAP1.BASE.PT ENDCAP1.TOP.PT

ENDCAPRAD;

POINT3 OUTLET.LO 60\_CM,0.0,0.0 ;

POINT3 OUTLET.HI 60\_CM,1.4\_CM,2pi ;

AREA3 OUTLET CONFORMAL OUTLET.LO OUTLET.HI;

! MARK the objects for AUTOGRID and create the grid.

MARK SHELL X1 SIZE Delta.Z ;

MARK SHELL X2 SIZE Delta.R ;

MARK SHELL X3 SIZE Delta.PHI ;

MARK ENDCAP1 X2 size delta.r;

MARK ENDCAP1 X3 SIZE delta.phi;

MARK ENDCAP1 X1 SIZE delta.z;

MARK OUTLET X2 size delta.r;

MARK OUTLET X3 SIZE delta.phi;

MARK OUTLET X1 SIZE delta.z;

AUTOGRID ;

! Add uniform confining axial magnetic field.

Confinement\_B=0.212\_TESLA;

```

FUNCTION B_axial(z,r) = Confinement_B ;
PRESET B1ST FUNCTION B_axial ;

Beam_current = 20Amps;      ! Beam current
Beam_voltage = 185KiloVolts; ! Beam energy
Beam_alpha = 1.2 ;         ! PitchFactor
electronchg = 1.6021e-19 ; ! Electronic Charge
electronmass = 9.10956e-31 ; ! Electronic Mass
clight = 3e8 ;             ! Speed of light
Gamma = 1 +(electronchg*Beam_voltage)/(electronmass*clight**2); !LF
Factor
Velocity_all = clight*(SQRT(1-(1/(gamma**2)))); ! Total v
Velocity_axial =Velocity_all/(SQRT(1+Beam_alpha**2)); ! v//
Velocity_transverse = Velocity_axial *Beam_alpha; ! v_||
GuidingCenter_radius = 0.00cm ; ! Guiding center radius

!*****
! Assign material properties, boundary conditions, and drive applications.

CONDUCTOR SHELL MATERIAL COPPER SOLID TRANSPARENCY 50;
CONDUCTOR ENDCAP1 MATERIAL GOLD SOLID TRANSPARENCY 95;

! Define inlet port plane

POINT3 INLET.LO 0.0,0.0,0.0 ;
POINT3 INLET.HI 0.0,1.4_CM,2pi ;
AREA3 INLET CONFORMAL INLET.LO INLET.HI ;

! Define outlet port plane

POINT3 OUTLET2.LO 61_CM,0.0,0.0 ;
POINT3 OUTLET2.HI 61_CM,1.4_CM,2pi ;
AREA3 OUTLET2 CONFORMAL OUTLET2.LO OUTLET2.HI;

PORT INLET POSITIVE;
PORT OUTLET2 NEGATIVE;

DrvFreq=9.5GHz;
maxwell biased; ! changed from high_q
Period = 1./DrvFreq ;
KPERIOD = period/sys$dttime ;
dttime =period/kperiod ;
time_step dttime ;
! =====emission model for generating the electron beam.

FUNCTION CURRENT(T) = BEAM_CURRENT ;
P_axial = Gamma*Velocity_axial ;
P_transverse = Gamma*Velocity_transverse ;

```

```

delta_emit = dtime * 1.c * velocity_axial ;
POINT3 GUIDING_CENTER 0,0,0.0;
EMISSION GYRO Current Confinement_B P_axial P_transverse
      GUIDINGCENTER_RADIUS
      guiding_center;
EMIT gyro ENDCAP1 ;
      observe eMITTED eNDCAP1 eELECTRON cURRENT ;

OUTPWG.ZMAX = 59.00_CM;
POINT OUTPUTCENT.PT 59_cm,0,0;

!=====Diagnosticssection
!Define lines and planes for diagnostics
LINE ZLINE CONFORMAL ENDCAP1.TOP.PT OUTPUTCENT.PT;
ZBY3 = OUTPWG.ZMAX ;
Zstart = 0.1_cm;
Zmiddle = CYL_LENGTH/2;
Zend = CYL_LENGTH-2_CM;
RBY3 = 0 ;
TBY3 = 0 ;
AREA ZPLANESTART CONFORMAL
Zstart,SY$$X2MN,SY$$X3MN,Zstart SY$$X2MX,SY$$X3MX ;
AREA ZPLANEmiddle CONFORMAL
Zmiddle,SY$$X2MN,SY$$X3MN,Zmiddle SY$$X2MX,SY$$X3MX ;
AREA ZPLANEend CONFORMAL Zend,SY$$X2MN,SY$$X3MN,Zend
SY$$X2MX,SY$$X3MX ;
AREA TPLANE CONFORMAL SY$$X1MN,SY$$X2MN,TBY3
SY$$X1MX,SY$$X2MX,TBY3 ;

!Define timers for diagnostics
TIMER BTIME DISCRETE 1;
tIMER eARLY DISCRETE 1;
tIMER eARLY1 DISCRETE 11;
Graphics PauseOff Early1 ;
Graphics PauseON Tsys$last ;
Timer ShowFrames1 periodic 20 300000 20 ;
Timer ShowFrames3 periodic 100 300000 100 ;

!Define required range and observe outputs

!RANGE FIELD B1ST ZLINE BTIME;
      POINT3 INLET2.LO 1.0CM,1cm,0.0 ;
      POINT3 INLET2.HI 1.0CM,1.4_CM,2pi ;
      AREA3 INLET2 CONFORMAL INLET2.LO INLET2.HI ;

!observe eMITTED ENDCAP1 eELECTRON cURRENT ;

!=====

```

!Use the times and observation planes previously defined to measure the  
!positions of the ptls in space and in energy, and plot the field patterns  
!at an instant in time. Save bitmap trails of some of these to produce  
!videos

```
PHASESPACE AXES X2 X3 eARLY ;  
PHASESPACE AXES X1 X2 TSYSS$LAST dump ; ! ;
```

```
PHASESPACE AXES X1 X2 ShowFrames1 Nodump ;  
VIEWER ShowFrames3 ;
```

```
VIEWER TSYSS$LAST ; ! ;
```

```
PHASESPACE AXES X1 KE TSYSS$LAST AXIS X SYSS$X1MN  
SYSS$X1MX ; PHASESPACE AXES X1 KE showframes3 AXIS X  
SYSS$X1MN SYSS$X1MX ;  
PHASESPACE AXES X2 X3 eARLY ;  
PHASESPACE AXES X1 X2 TSYSS$LAST dump ; ! ;
```

```
runfor = 12_nanoseconds;  
duration runfor;  
EXPORT OUTLET NEGATIVE elecbeam2 binary ;  
DISPLAY ;  
START ;  
STOP;
```

```
!
```

```
=====
```

```
HEADER ORGANIZATION "University of Strathclyde" ;  
HEADER Author "Jamie Thomson" ;  
HEADER DEVICE "Gyro-TWA" ;
```

```
! =====
```

```
ON = 1 ;  
OFF = 0 ;  
IDISPLAY = ON ;  
IFREQUENCY = ON ;  
IVECTOR = ON ;  
IVIEW = On ; ! Select view plots.  
IDUMP = On ;
```

```
GRAPHICS PAUSE ;  
GRAPHICS PAUSEOFF TSYSS$FIRST ;
```

```
SYSTEM CYL ;
```

```
! Parameters defining the chamber.
```

```
STARTOFSIM = -3_CM; ! Start point of simulation
```

```

CYL_RADIUS = 1.8_CM ; ! Cylinder inner radius
m= 3; ! Azimuthal component
d= 3.9_CM; ! Period
h= 2.PI/d;
a0= 0.014; ! Mean Radius
a1= 0.0022; ! Corrugation depth
TAPER_LENGTH = 1*d;
TAPER_START = 16*d+TAPER_LENGTH;
CYL_LENGTH = TAPER_LENGTH+TAPER_START; !
Cylinder length
FUNCTION helixpara(Z,R,PHI) = R - a0 - a1*SIN(h*Z-m*PHI); !
Helical shaped hole
FUNCTION helix taper(Z,R,PHI)= R - a0 - a1*Z/TAPER_LENGTH*SIN(h*Z-
m*PHI); ! Taper hole
FUNCTION helix taper2(Z,R,PHI)=R -a0 + (a1*(Z-CYL_LENGTH)*SIN(h*Z-
m*PHI)/TAPER_LENGTH);

! Mesh resolution parameters.
DELTA.Z = d/19.5 ; ! Axial resolution.
DELTA.R = a1/3.3 ! Radial resolution.
DELTA.PHI = 2.PI/24 ; ! Azimuthal Resolution
DRM = 2*DELTA.R;
DRMAX = 3*DELTA.R;

! Define the input waveguide section
POINT3 CIRSHELL.LO STARTOFSIM,a0,0PI ;
POINT3 CIRSHELL.HI 0.0,CYL_RADIUS,2.PI ;
VOLUME CIRSHELL CONFORMAL CIRSHELL.LO CIRSHELL.HI ;

! Define the confining shell.
POINT3 SHELL.LO 0.0,0.0,0.0PI ;
POINT3 SHELL.HI CYL_LENGTH,CYL_RADIUS,2.PI ;
VOLUME SHELL CONFORMAL SHELL.LO SHELL.HI ;

! Define Helix on inside of shell
POINT3 HSHELL.LO TAPER_LENGTH,0.0,0PI ;
POINT3 HSHELL.HI TAPER_START,CYL_RADIUS,2.PI ;
VOLUME helix FUNCTIONAL helixpara HSHELL.LO HSHELL.HI;

!Define the input taper
POINT3 TAPER.LO 0,0,0PI;
POINT3 TAPER.HI TAPER_LENGTH,cyl_radius,2PI;
VOLUME taper FUNCTIONAL helix taper TAPER.LO TAPER.HI;

!Define the output taper
POINT3 TAPER2.LO taper_start,0,0PI;
POINT3 TAPER2.HI cyl_length,cyl_radius,2PI;
VOLUME taper2 FUNCTIONAL helix taper2 TAPER2.LO TAPER2.HI;

```

```

!Define output horn
  OHORNEND=cyl_length+3*d;
  OHORNRAD=CYL_RADIUS+0.2cm;
  POINT OUTPUTHORN.LO cyl_length,a0,0PI;
  POINT OUTPUTHORN.HI ohornend,ohornrad,2.PI;
  VOLUME OUTPUTHORN CONFORMAL OUTPUTHORN.LO
OUTPUTHORN.HI;

!Define cut in output horn
  POINT OHORNCUT.LO CYL_LENGTH,a0,0;
  POINT OHORNCUT.HI ohornend,ohornrad,2.PI;
  FUNCTION otaperhorn(Z,R)=R-a0-0.25cm-0.25_CM*SIN((1.PI/(3*d))*(Z-
(cyl_length))-1.PI/2);
  VOLUME OHORNCUT FUNCTIONAL otaperhorn OHORNCUT.LO
OHORNCUT.HI;

  OUTWGEND=ohornend+1.5*d;
  POINT3 CIRSHELL2.LO ohornend,1.4_CM+0.5_CM,0PI ;
  POINT3 CIRSHELL2.HI outwend,ohornrad,2.PI ;
  VOLUME CIRSHELL2 CONFORMAL CIRSHELL2.LO CIRSHELL2.HI ;

! MARK the objects for AUTOGRID and create the grid.
  MARK SHELL X1 MIN SIZE Delta.Z ;
  MARK SHELL X1 MAX SIZE Delta.Z ;
  MARK SHELL X2 MIN SIZE DRM ;
  MARK SHELL X2 MAX SIZE DRMAX ;
  MARK SHELL X3 SIZE Delta.PHI ;

  MARK CIRSHELL X1 MIN SIZE Delta.Z ;
  MARK CIRSHELL X1 MAX SIZE Delta.Z ;
  MARK CIRSHELL X2 MIN SIZE DRM ;
  MARK CIRSHELL X2 MAX SIZE DRMAX ;
  MARK CIRSHELL X3 SIZE Delta.PHI ;

  MARK CIRSHELL2 X1 MIN SIZE Delta.Z ;
  MARK CIRSHELL2 X1 MAX SIZE Delta.Z ;
  MARK CIRSHELL2 X2 MIN SIZE DRM ;
  MARK CIRSHELL2 X2 MAX SIZE DRMAX ;
  MARK CIRSHELL2 X3 SIZE Delta.PHI ;

  MARK OUTPUTHORN X1 MIN SIZE Delta.Z ;
  MARK OUTPUTHORN X1 MAX SIZE Delta.Z ;
  MARK OUTPUTHORN X2 MIN SIZE DRM ;
  MARK OUTPUTHORN X2 MAX SIZE DRMAX ;
  MARK OUTPUTHORN X3 SIZE Delta.PHI ;

AUTOGRID ;

```



```

! Define Solenoid
CCURRENT = 845A;
CCENTZ = 0.23 ;10.23
CCENTR = 0.02 ;
TURNTHICKZ = 0.005 ;
TURNTHICKR = TURNTHICKZ ;
TURNSZ = 200 ;
LAYERS = 1 ;
COILS AXIS X1;

!=====
!Build Solenoid using the coil command
CLOWZ = CCENTZ - ((TURNSZ-1)*TURNTHICKZ/2);
CLOWR = CCENTR - ((LAYERS-1)*TURNTHICKR/2);

DO N = 1,LAYERS ;
  DO M = 1,TURNSZ ;
    ZPOS=(CLOWZ + (M-1)*TURNTHICKZ);
    RPOS=(CLOWR + (N-1)*TURNTHICKR);
    COILS DEFINITION ZPOS,0,0 RPOS CCURRENT;
  ENDDO;
ENDDO;

! Add uniform confining axial magnetic field.
! Confinement_B=0.2_TESLA;

! FUNCTION B_axial(z,r) = Confinement_B ;
! PRESET B1ST FUNCTION B_axial ;

!=====Define the injected electron beam

Beam_current = 20Amps;      ! Beam current
Beam_voltage = 185KiloVolts; ! Beam energy
Beam_alpha = 1.1 ;         ! Pitch Factor
electronchg = 1.6021e-19 ; ! Electronic Charge
electronmass = 9.10956e-31 ; ! Electronic Mass
clight = 3e8 ;             ! Speed of light
Gamma = 1 + (electronchg*Beam_voltage)/(electronmass*clight**2); ! LF
Factor
Velocity_all = clight*(SQRT(1-(1/(gamma**2)))); ! Total v
Velocity_axial = Velocity_all/(SQRT(1+Beam_alpha**2)); ! v//
Velocity_transverse = Velocity_axial * Beam_alpha; ! v_⊥
GuidingCenter_radius = 0.00cm ; ! Guiding center radius

!*****
! Assign material properties, boundary conditions, and drive applications.

```

```

CONDUCTOR SHELL MATERIAL COPPER SOLID TRANSPARENCY 50
CONDUCTOR CIRSELL MATERIAL COPPER SOLID TRANSPARENCY 50;
CONDUCTOR OUTPTHORN MATERIAL SILVER SOLID TRANSPARENCY
50;
  CONDUCTOR CIRSELL2 MATERIAL GOLD SOLID TRANSPARENCY 95;
  VOID HELIX;
  VOID TAPER;
  VOID TAPER2;
  VOID OHORNCUT;

! Define inlet port plane
POINT3 INLET.LO -3_CM,0.0,0.0 ;
POINT3 INLET.HI -3_CM,a0,2pi ;
  AREA3 INLET CONFORMAL INLET.LO INLET.HI ;

! Define outlet port plane
  PPOSTION=OUTWGEND-1_CM;
POINT3 OUTLET.LO PPOSTION,0.0,0.0 ;
POINT3 OUTLET.HI PPOSTION,ohornrad,2pi ;
  AREA3 OUTLET CONFORMAL OUTLET.LO OUTLET.HI ;

! Circularly polarised wave

POINT3 DRIVE.LO 0.0CM, 0.0, 0.PI ;
POINT3 DRIVE.HI 0.0CM, a0, 2.PI ;
POINT3 line.lo 0.0CM,0.0,0.5PI;
POINT3 line.hi 0.0CM,a0,0.5PI;
LINE normanline CONFORMAL line.lo line.hi;
AREA DRIVE_LOCATION CONFORMAL DRIVE.LO DRIVE.HI ;
Area DRIVE_LOCATION1 CONFORMAL DRIVE.LO DRIVE.HI ;
Parameter DrvFreq = 9.5GHZ ;
Parameter xKT = 1.841/a0;
Parameter xKT2 = 1.841/OHORNRAD;
Parameter CutFreq = xKT*CLIGHT/2.PI;
Parameter CutFreq2 = xKT2*CLIGHT/2.PI;
Parameter Vphase = 1/sqrt(1-(CutFreq/DrvFreq)**2) ;
Parameter Vphase2 = 1/sqrt(1-(CutFreq2/DrvFreq)**2) ;

!-----
! set maxwell algorithm, mode, and time step Adjust the timestep such that the drive
!frequency is an integral multiple of the timestep.

runfor = 10_nanoseconds;
duration runfor;

  maxwell high_q;
  Period = 1./DrvFreq ;
  KPERIOD = period/sys$time ;

```

```

    dtime =period/kperiod ;
    time_step dtime ;
    Drive_strength=0.1;
    FUNCTION f(t)= SIN(2.PI*t*DrvFreq);
    FUNCTION TE_Er(t,Z,R,PHI) =
    Drive_strength*SIN(PHI)/R*BESSELJ1(1.841*R/a0)*f(t);
    FUNCTION TE_Ep(t,Z,R,PHI) =
    Drive_strength*1.841/a0*COS(PHI)*BESSELJP(1,1.841*R/a0)*f(t);
    DRIVER J2 TE_Er DRIVE_LOCATION;
    DRIVER J3 TE_Ep DRIVE_LOCATION1;

IMPORT INLET POSITIVE FILE elecbeam2 binary ;
Port outlet Negative PHASE_VELOCITY Vphase2 ;

!PORT inlet Positive PHASE_VELOCITY Vphase;

! =====emission model for generating the electron beam.

    FUNCTION CURRENT(T) = BEAM_CURRENT ;
    P_axial = Gamma*Velocity_axial ;
    P_transverse = Gamma*Velocity_transverse ;
    delta_emit = dtime * 1.c * velocity_axial ;

OUTPWG.ZMAX = 73_CM;
POINT OUTPUTCENT.PT 73_cm,0,0;

! =====Diagnostics section
!Define lines and planes for diagnostics
LINE ZLINE CONFORMAL 0,0,0 OUTPUTCENT.PT;
ZBY3 = OUTPWG.ZMAX ;
Zstart = 0.1_cm;
Zmiddle = CYL_LENGTH/2;
Zend = 73_cm;
RBY3 = 0 ;
TBY3 = 0 ;
AREA ZPLANE CONFORMAL ZBY3,SY$$X2MN,SY$$X3MN,ZBY3
SY$$X2MX,SY$$X3MX ;
AREA ZPLANESTART CONFORMAL Zstart,SY$$X2MN,SY$$X3MN,Zstart
SY$$X2MX,SY$$X3MX ;
AREA ZPLANEmiddle CONFORMAL Zmiddle,SY$$X2MN,SY$$X3MN,Zmiddle
SY$$X2MX,SY$$X3MX ;
AREA ZPLANEend CONFORMAL Zend,SY$$X2MN,SY$$X3MN,Zend
SY$$X2MX,SY$$X3MX ;
AREA TPLANE CONFORMAL SY$$X1MN,SY$$X2MN,TBY3
SY$$X1MX,SY$$X2MX,TBY3 ;

!Define timers for diagnostics

```

```
TIMER BTIME DISCRETE 1;
tIMER eARLY DISCRETE 1;
tIMER eARLY1 DISCRETE 11;
Graphics PauseOff Early1 ;
Graphics PauseON Tsys$last ;
Timer ShowFrames1 periodic 20 300000 20 ;
Timer ShowFrames3 periodic 100 300000 100 ;
```

!Define required range and observe outputs

```
RANGE FIELD B1ST ZLINE BTIME;
  POINT3 INLET2.LO 1.0CM,1cm,0.0 ;
  POINT3 INLET2.HI 1.0CM,CYL_RADIUS,2pi ;
  AREA3 INLET2 CONFORMAL INLET2.LO INLET2.HI ;
```

```
observe field_power S.DA OUTLET;
observe field_power S.DA ZPLANESTART;
observe field_power S.DA ZPLANEMIDDLE;
observe field_power S.DA ZPLANEEND;
OBSERVE FIELD_POWER E.J_DRIVER.DV DRIVE_LOCATION;
OBSERVE FIELD_POWER E.J_DRIVER.DV DRIVE_LOCATION1;
```

!=====

!Use the times and observation planes previously defined to measure the  
!positions of the ptls in space and in energy, and plot the field patterns  
!at an instant in time. Save bitmap trails of some of these to produce  
!videos

```
PHASESPACE AXES X2 X3 eARLY ;
PHASESPACE AXES X1 X2 TSYSS$LAST dump ; !movie ;
```

```
VECTOR FIELD E2 E3 ZPLANE TSYSS$LAST dump ;
VECTOR FIELD B2 B3 ZPLANE TSYSS$LAST dump ;
VECTOR FIELD E1 E2 TPLANE TSYSS$LAST dump ;
VECTOR FIELD B1 B2 TPLANE TSYSS$LAST dump ;
```

```
CONTOUR FIELD E1 zplanestart showframes3 dump shade movie;
CONTOUR FIELD E2 zplanestart showframes3 dump shade movie;
CONTOUR FIELD E3 zplanestart showframes3 dump shade movie;
CONTOUR FIELD E1 zplanemiddle showframes3 dump shade movie;
CONTOUR FIELD E2 zplanemiddle showframes3 dump shade movie;
CONTOUR FIELD E3 zplanemiddle showframes3 dump shade movie;
CONTOUR FIELD E1 zplaneend showframes3 dump shade movie;
CONTOUR FIELD E2 zplaneend showframes3 dump shade movie;
CONTOUR FIELD E3 zplaneend showframes3 dump shade movie;
```

```
CONTOUR FIELD E3 zplane showframes3 dump shade movie;
```

```
CONTOUR FIELD E2 zplane showframes3 dump shade movie;
CONTOUR FIELD E1 zplane showframes3 dump shade movie;
CONTOUR FIELD E2 zplane TSYSS$LAST dump shade;
CONTOUR FIELD b3 zplane TSYSS$LAST dump shade;
CONTOUR FIELD b1 zplane TSYSS$LAST dump shade;
CONTOUR FIELD b2 zplane TSYSS$LAST dump shade;
```

```
CONTOUR FIELD E3 TPLANE TSYSS$LAST dump shade;
CONTOUR FIELD E1 TPLANE TSYSS$LAST dump shade;
CONTOUR FIELD E2 TPLANE TSYSS$LAST dump shade;
```

```
CONTOUR FIELD B3 TPLANE TSYSS$LAST dump shade;
CONTOUR FIELD B1 TPLANE TSYSS$LAST dump shade;
CONTOUR FIELD B2 TPLANE TSYSS$LAST dump shade;
```

```
PHASESPACE AXES X1 X2 ShowFrames1 Nodump ;
VIEWER ShowFrames3 movie ;
```

```
VIEWER TSYSS$LAST ; !movie;
```

```
PHASESPACE AXES X1 KE TSYSS$LAST AXIS X SYSS$X1MN SYSS$X1MX ;
PHASESPACE AXES X1 KE showframes3 AXIS X SYSS$X1MN SYSS$X1MX
movie;
PHASESPACE AXES X2 X3 eARLY ;
PHASESPACE AXES X1 X2 TSYSS$LAST dump ; !movie ;
```

```
!-----
! Define diagnostics.
```

```
FPOSITION=PPOSITION-1_CM;
POINT3 RECEND1 FPOSITION,0.0_CM,90deg;
POINT3 RECEND2 FPOSITION,1.0_CM,270deg;
POINT3 RECEND3 FPOSITION,0.0_CM,0.0;
POINT3 RECEND4 FPOSITION,1.0_CM,180deg;
LINE parallel oblique RECEND1 RECEND2;
LINE perpendicular oblique RECEND3 RECEND4;
POINT3 START 0.0,1.0cm,90deg;
```

```
OBSERVE FIELD E2 parallel FFT MAGNITUDE DB_SCALE 10 WINDOW
FREQUENCY 7.5GHz 12.5GHz DUMP;
```

```
OBSERVE FIELD E2 perpendicular FFT MAGNITUDE DB_SCALE 10
WINDOW FREQUENCY 7.5GHz 12.5GHz DUMP;
```

```
OBSERVE FIELD E2 START FFT MAGNITUDE WINDOW FREQUENCY
5.0GHz 14.0GHz DUMP;
```

```
runfor = 10_nanoseconds;
duration runfor;
DISPLAY ;
```

START ;  
STOP;

### MAGIC Simulation for prediction of dispersion characteristics of helically corrugated waveguide

HEADER ORGANIZATION "RELD" ;  
HEADER AUTHOR "G. Burt - Modified by J. Thomson" ;  
HEADER DEVICE "Helical Waveguide Dispersion" ;

graphics pause ;

!-----  
! Problem definition.  
!  
! Construct an oversized cylindrical waveguide with a helical corrugation on the  
! inner surface.  
!  
! Parameters defining the chamber.

    CYL\_RADIUS = 1.8\_CM ;    ! Cylinder inner radius  
    m=3;                    ! Azimuthal component  
    d=2.7\_CM;              ! Period  
    h=2.PI/d;  
    a0=1.36\_CM;            ! Mean Radius  
    a1=0.32\_CM;            ! Corrugation depth  
    TAPER\_LENGTH = 1\*d;  
    TAPER\_START = 12\*d+TAPER\_LENGTH;  
    CYL\_LENGTH = TAPER\_LENGTH+TAPER\_START;  
                            ! Cylinder length  
    FUNCTION helixpara(Z,R,PHI) = R- a0 - a1\*SIN(h\*Z-m\*PHI);  
                            ! Helical shaped hole  
    FUNCTION helix taper(Z,R,PHI)= R- a0 -  
a1\*Z/TAPER\_LENGTH\*SIN(h\*Z-m\*PHI);            ! Taper hole  
    FUNCTION helix taper2(Z,R,PHI)=R -a0 + (a1\*(Z-CYL\_LENGTH)\*SIN(h\*Z-  
m\*PHI)/TAPER\_LENGTH);

! Mesh resolution parameters.

    DELTA.Z = d/18;          ! Axial resolution        d/18  
    DELTA.R = a1/8;          ! Radial resolution        a1/4  
    DELTA.PHI = 2.PI/60;     ! Azimuthal Resolution        2.pi/60

! Parameters defining the electron beam.

    TIME\_OF\_RUN = 50.0NANOSECONDS ;

! Useful constants.

```
CLIGHT=1.c;  
PIRA = 1.pi;  
XMU0 = PIRA*4.E-7 ;  
TWOPI = 2.PI ;  
EPS0 = 8.8544E-12 ;
```

```
!-----  
! Command aliasing required for 3d/2d ;  
IF (ISYSCODE.EQ.2) THEN ;  
    VOLUME = "AREA2" ;      ! i.e. CONDUCTOR assignment  
    AREA3 = "LINE2" ; ! i.e. PORT,EXPORT,IMPORT assignment  
    POINT = "POINT3" ;      ! i.e. every point  
    DISPLAY_3D ="DISPLAY_2D" ;  
ENDIF ;
```

```
!  
!-----  
! Select the coordinate system and create the OBJECTS
```

```
    SYSTEM CYL ;
```

! Define the polariser

! Define the endcaps.

```
Point3 endcap2.lo CYL_LENGTH,0.0cm,0.0 ;  
Point3 endcap2.hi CYL_LENGTH,cyl_radius,2pi ;  
AREA ENDCAP2 CONFORMAL ENDCAP2.LO ENDCAP2.HI ;
```

! Define the confining shell.

```
POINT3 TAPER.HI TAPER_LENGTH,CYL_RADIUS,2.PI ;  
POINT3 HSHELL.LO TAPER_LENGTH,0.0,0PI ;  
POINT3 TAPER2.HI TAPER_START,CYL_RADIUS,2.PI ;  
POINT3 TAPER2.LO TAPER_START,0.0,0PI ;
```

```
POINT3 SHELL.LO 0.0,0.0,0.0PI ;  
POINT3 SHELL.HI CYL_LENGTH,CYL_RADIUS,2.PI ;  
VOLUME SHELL CONFORMAL SHELL.LO SHELL.HI ;
```

!Define the taper

```
VOLUME taper FUNCTIONAL helix taper SHELL.LO TAPER.HI ;  
VOLUME helix FUNCTIONAL helix para HSHELL.LO TAPER2.HI ;  
VOLUME taperend FUNCTIONAL helix taper2 TAPER2.LO SHELL.HI ;
```

! Define the rec-cir converter

```
CONVERTER_END= CYL_LENGTH+10.02483cm;
```

```

! POINT3 CONSHELL.LO CYL_LENGTH,a0,0PI ;
! POINT3 CONSHELL.HI CONVERTER_END,CYL_RADIUS,2.PI ;
! VOLUME CONSHELL CONFORMAL CONSHELL.LO CONSHELL.HI ;

```

```

! Define the input WG

```

```

POINT3 CIRSHELL.LO -3cm,a0,0PI ;
POINT3 CIRSHELL.HI 0.0,CYL_RADIUS,2.PI ;
VOLUME CIRSHELL CONFORMAL CIRSHELL.LO CIRSHELL.HI ;

```

```

!Define input horn

```

```

POINT3 INPUTHORN.LO -13.0_cm,2_CM,0PI ;
POINT3 INPUTHORN.HI -3.0cm,a0,2.PI ;
VOLUME INPUTHORN CONFORMAL INPUTHORN.LO
INPUTHORN.HI ;

```

```

!Define output horn

```

```

POINT OUTPUTHORN.LO cyl_length,a0,0PI;
POINT OUTPUTHORN.HI converter_end,2_CM,2.PI;
VOLUME OUTPUTHORN CONFORMAL OUTPUTHORN.LO
OUTPUTHORN.HI;

```

```

!Define void to shape inpuhorn

```

```

POINT VOIDINPUTHORN.LO -13.0_cm,1.95_CM,0PI ;
POINT VOIDINPUTHORN.HI -8.0cm,a0,2.PI ;
VOLUME VOIDINPUTHORN CONFORMAL VOIDINPUTHORN.LO
VOIDINPUTHORN.HI;

```

```

!Define void to shape outpuhorn

```

```

ENDVOID = cyl_length+5CM;
POINT VOIDOUTPUTHORN.LO ENDVOID,a0,0PI;
POINT VOIDOUTPUTHORN.HI converter_end,1.95_CM,2.PI;
VOLUME VOIDOUTPUTHORN CONFORMAL VOIDOUTPUTHORN.LO
VOIDOUTPUTHORN.HI;

```

```

!Define cut void to shape inpuhorn

```

```

! POINT L -8_CM,1.943_CM,2.PI;
! POINT A -8_CM,1.943_CM,0PI;
! POINT B -7_CM,1.83_CM,0PI;
! POINT C -6_CM,1.73_cm,0PI;
! POINT D -5_CM,1.6_CM,0PI;
! POINT E -4_CM,1.5_CM,0PI;
! POINT F -8_CM,1.5_CM,0PI;
! AREA shapecut POLYGONAL A B C D E F A;
! LINE path CONFORMAL A L;
! VOLUME CUTHORN EXTRUDE shapecut path;

```

```

!Define cut in input horn

```

```

POINT HORNCUT.LO -8_CM,a0,0;

```



```

POINT HORNCUT.HI -2.3_CM,1.95_cm,2.PI;
FUNCTION taperhorn(Z,R)=R-1.65cm-0.30cm*SIN((2.PI/12cm)*(Z-
0.6cm));
VOLUME HORNCUT FUNCTIONAL taperhorn HORNCUT.LO
HORNCUT.HI;

```

!Define cut in output horn

```

POINT OHORNCUT.LO 51.1_CM,a0,0;
POINT OHORNCUT.HI 56.8_CM,1.95_cm,2.PI;
FUNCTION otaperhorn(Z,R)=R-1.65cm-0.30cm*SIN((2.PI/12cm)*(Z-
5.8cm));
VOLUME OHORNCUT FUNCTIONAL otaperhorn OHORNCUT.LO
OHORNCUT.HI;

```

!-----  
! MARK the objects for AUTOGRID and create the grid.

```

MARK SHELL X1 SIZE Delta.Z ;
MARK SHELL X2 SIZE Delta.R ;
MARK SHELL X3 SIZE Delta.PHI ;

```

```

! MARK CONSHELL X1 SIZE Delta.Z ;
! MARK CONSHELL X2 SIZE Delta.R ;
! MARK CONSHELL X3 SIZE Delta.PHI;

```

```

MARK CIRSHELL X1 SIZE Delta.Z ;
MARK CIRSHELL X2 SIZE Delta.R ;
MARK CIRSHELL X3 SIZE Delta.PHI ;

```

```

MARK INPUTHORN X1 SIZE Delta.Z ;
MARK INPUTHORN X2 SIZE Delta.R ;
MARK INPUTHORN X3 SIZE Delta.PHI ;

```

```

MARK OUTPUTHORN X1 SIZE Delta.Z ;
MARK OUTPUTHORN X2 SIZE Delta.R ;
MARK OUTPUTHORN X3 SIZE Delta.PHI ;

```

```

AUTOGRID ;

```

!-----  
! Define outlet port plane.

```

POINT3 OUTLET.LO -13.0cm,0.0,0.0 ;
POINT3 OUTLET.HI -13.0cm,1.95_CM,2pi ;
AREA3 OUTLET CONFORMAL OUTLET.LO OUTLET.HI ;

```

```

!-----
! Set simulation duration.
      duration Time_OF_run ;
!-----
! Assign material properties, boundary conditions, and drive applications.

! CONDUCTOR CONSHELL MATERIAL COPPER SOLID TRANSPARENCY
50;
      CONDUCTOR SHELL MATERIAL COPPER SOLID TRANSPARENCY
50;
      CONDUCTOR CIRSELL MATERIAL COPPER SOLID TRANSPARENCY
50;
      CONDUCTOR INPUTHORN MATERIAL SILVER SOLID
TRANSPARENCY 50;
      CONDUCTOR OUTPUTHORN MATERIAL SILVER SOLID
TRANSPARENCY 50;

      VOID HELIX;
      VOID TAPER;
      VOID TAPEREND;
      VOID VOIDINPUTHORN;
      VOID VOIDOUTPUTHORN;
      VOID HORNCUT;
      VOID OHORNCUT;

! Electromagnetic Wave.
Parameter Transit_time = 2*(SYSS$X1MX)/1.c ;
Parameter TEND_SIGNAL =TIME_OF_RUN - 10.*TRANSIT_TIME ; ! this is
important
TPULSE = (NINT(.5*TEND_SIGNAL/SYSS$DTIME)+0.5)*SYSS$DTIME ; ! avoid
zero over zero form
      FREQLO=6.0GHz;
      FREQHI=12.5GHz;
      FREQmd=11.0GHz;
      OMEGALO = 2PI*FREQLO;
      OMEGAHI = 2PI*FREQHI;
      Parameter xKT = 1.841/a0;
      Parameter CutFreq = xKT*CLIGHT/2.PI;
      Parameter Vphase = 1/sqrt(1-(CutFreq/FREQmd)**2) ;
      FUNCTION TE_Er(Z,R,PHI) = SIN(PHI)/R*BESSELJ1(1.841*R/a0);
      FUNCTION TE_Ep(Z,R,PHI) =
1.841/a0*COS(PHI)*BESSELJP(1,1.841*R/a0);
      FUNCTION f(t)= (sin(OMEGALO*(t-Tpulse))-sin(OMEGAHI*(t-Tpulse)))/(t-
Tpulse)*sqrt(2.PI) ;
      Line NORMALIZATIONLINE Conformal -1.0cm,0.0,0.5PI -1.0cm,a0,0.5PI ;
      Port outlet Positive
      PHASE_VELOCITY Vphase Incoming f
      FUNCTION E2 TE_Er E3 TE_Ep

```

```

Normalization Voltage NORMALIZATIONLINE;
POINT3 rec.P0 converter_end,0.0,0.0 ;           !1st co-ord converter_end
POINT3 rec.P1 converter_end,1.95_CM,2.PI ;      !1st co-ord
converter_end
AREA3 OUTPUT CONFORMAL rec.P0 rec.P1;
Port OUTPUT Negative;

```

```

!-----
! Define diagnostics.

```

```

POINT3 RECEND1 63.8_CM,0.0_CM,90deg;
POINT3 RECEND2 63.8_CM,1.0_CM,270deg;
POINT3 RECEND3 63.8_CM,0.0_CM,0.0;
POINT3 RECEND4 63.8_CM,1.0_CM,180deg;
LINE parallel oblique RECEND1 RECEND2;
LINE perpendicular oblique RECEND3 RECEND4;
POINT3 START 0.0,1.0cm,90deg;

```

```

OBSERVE FIELD E2 parallel FFT MAGNITUDE DB_SCALE 10 WINDOW
FREQUENCY 7.5GHz 12.5GHz DUMP;

```

```

OBSERVE FIELD E2 perpendicular FFT MAGNITUDE DB_SCALE 10
WINDOW FREQUENCY 7.5GHz 12.5GHz DUMP;

```

```

OBSERVE FIELD E2 START FFT MAGNITUDE WINDOW FREQUENCY
5.0GHz 14.0GHz DUMP;

```

```

DISPLAY ;
START ; STOP ;
!

```

## **Appendix B. MAPLE Script**

## MAPLE Code for prediction of linear gain behaviour of gyro-TWA

Define here the parameters of the helix corrugated waveguide. Note this method uses the cubic approximation for the present, it should probably be modified to solve directly the full double hyperbolic. The parameters are  $d$ , the axial periodicity of the helix,  $a_0$ , the mean radius,  $\sigma$  (the coupling co-efficient, determined by the helix corrugation depth and the nature of the helix structure and the modes being coupled), and the cut-off wavevector of the modes being coupled. We derive the quantities  $\bar{h}$ ,  $h_0$ ,  $\Delta g$  and  $\Delta g/h_0$  from these definitions. They represent the axial wavevector of the corrugation, the propagation wavevector of the travelling mode at the cut-off of the non-propagating mode, the so called geometric mismatch between the axial geometry and this propagation wavevector and the normalised value of the mismatch

```
> restart;
d:=0.039;
hbar:=2*Pi/d;
a0:=0.0141;
sigma:=24.45;
ko:=3.054/a0;kob:=1.841/a0;
h0:=sqrt(ko^2-kob^2);
delg:=hbar-h0;
delgnorm:=(delg/ko);sigmanorm:=(sigma/ko);h0norm:=h0/ko;
      d := 0.039
      hbar := 51.28205128 p
      a0 := 0.0141
      s := 24.45
      ko := 216.5957447
      kob := 130.5673759
      h0 := 172.8174672
      delg := 51.28205128 p - 172.8174672
      delgnorm := 0.2367638910 p - 0.7978802513
      sigmanorm := 0.1128831041
      h0norm := 0.7978802512
```

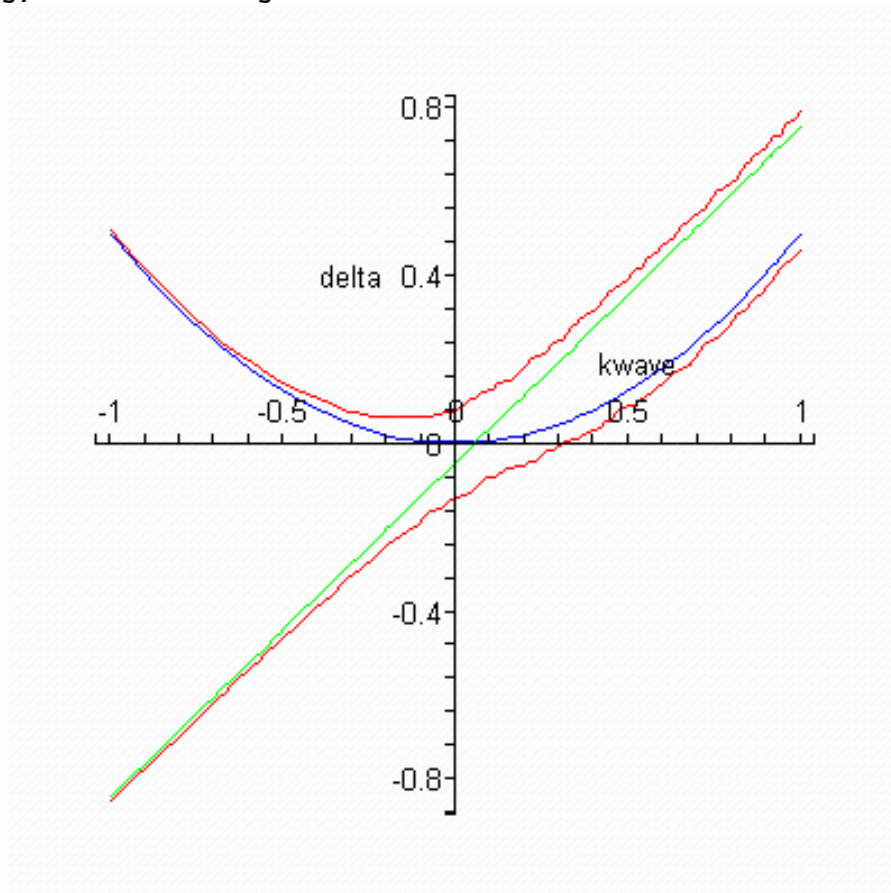
Define here a function describing the coupled waves, plot the result of an implicit solution of this set equal to an appropriate coupling term, all variables and parameters normalised to  $k_0$

```
> disp:=(((kwave)^2)-2*(delta))*(kwave)+(delgnorm)-(delta/h0norm));
>
```

```
disp := (kwave2 - 2 d) (kwave + 0.2367638910 p - 0.7978802513 - 1.253320907 d)
```

```
> with(plots):implicitplot([disp=2*(sigmanorm^2)/h0norm,
2*delta-kwave^2=0, delta-(kwave+(delgnorm))*(h0norm)=0],
kwave=-1..1, delta=-1..1, color=[red,blue,green]);
>
```

Warning, the name changecoords has been redefined



Define here some fundamental constants and some parameters of the electron beam, the speed of light, electronic charge and mass, the accelerating potential, current, axial static magnetic field, cyclotron harmonic, pitch angle, derive the Lorentz-Fitzgerald parameter, the angular and real cyclotron frequencies, the axial and orbital initial velocities in absolute terms and normalised to the speed of light

```
> c:=3*(10^8);
e:=1.602*10^(-19);
m0:=9.11*10^(-31);
Volts:=115000;
current:=18;
B:=0.2;
```

```

s:=2;
alpha:=1.2;
gamma_i:=1+e*Volts/(m0*c^2);
omega_ce:=e*B/(m0*gamma_i);
f_ce:=omega_ce/(2*Pi);evalf(f_ce);
beta:=sqrt(1-
1/gamma_i^2);beta_para:=sqrt(beta^2/(1+alpha^2));beta_perp:=sqrt(beta^2-
beta_para^2);v:=c*beta;v_para:=c*beta_para;v_perp:=c*beta_perp;

```

*c* := 300000000

*e* := 1.602000000 10<sup>-19</sup>

*m0* := 9.110000000 10<sup>-31</sup>

*Volts* := 150000

*current* := 10

*B* := 0.2

*s* := 2

*a* := 1.2

*gamma\_i* := 1.293084523

*omega\_ce* := 2.719864175 10<sup>10</sup>

*f\_ce* :=  $\frac{1.359932088 \cdot 10^{10}}{p}$

4.328798280 10<sup>9</sup>

*b* := 0.6339858435

*beta\_para* := 0.4058678466

*beta\_perp* := 0.4870414160

*v* := 1.901957530 10<sup>8</sup>

*v\_para* := 1.217603540 10<sup>8</sup>

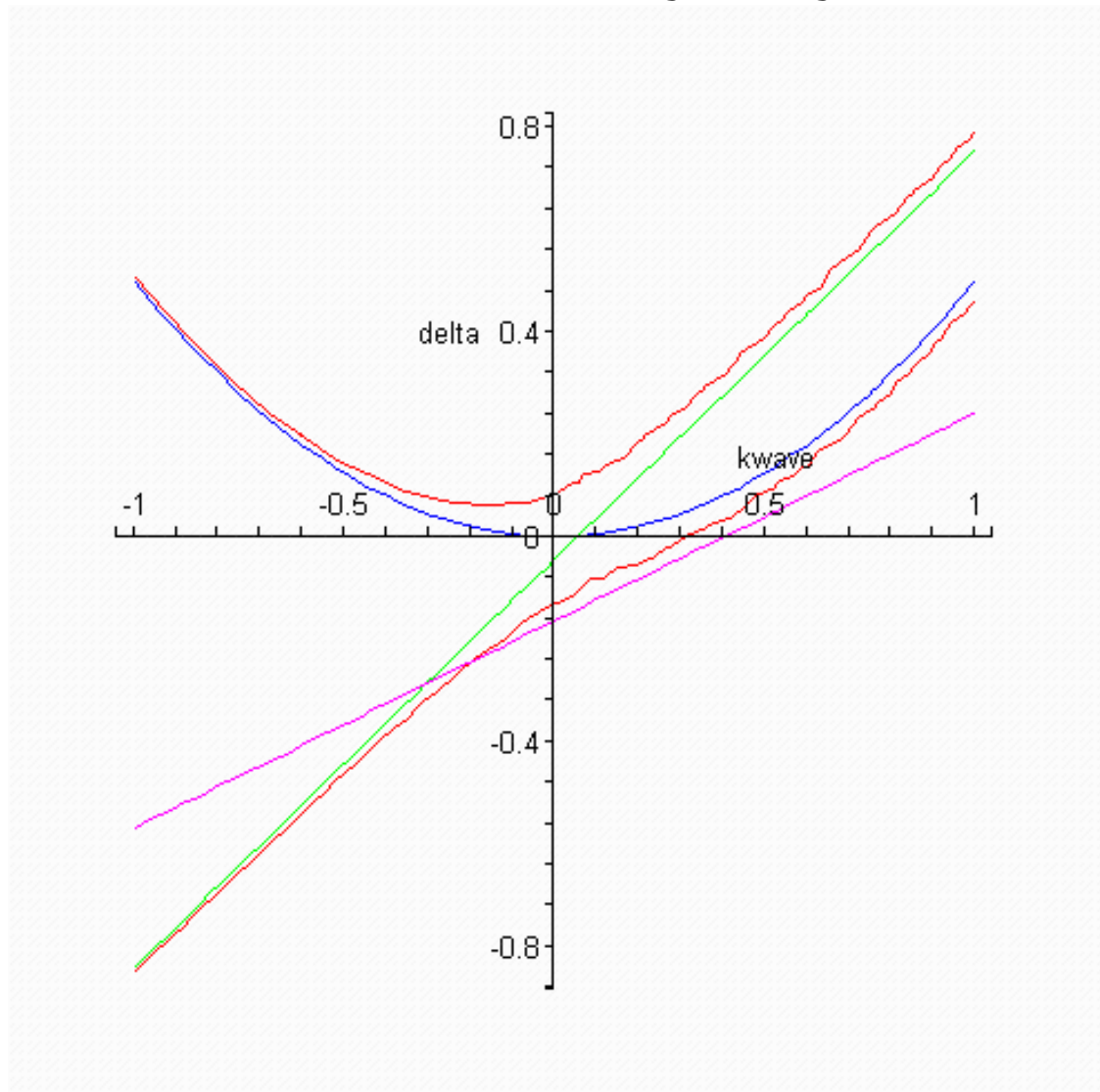
*v\_perp* := 1.461124248 10<sup>8</sup>

>  
>  
>

```

Next, the beam dispersion is included on the plot.
with(plots):implicitplot([disp=2*(sigmanorm^2)/h0norm,
2*delta-kwave^2=0, delta-(kwave+(delgnorm))*(h0norm)=0,
delta=(s*omega_ce/(c*ko))+beta_para*kwave-1], kwave=-
1..1, delta=-1..1, color=[red,blue,green,magenta]);

```



```

>
>
> Here we define the Bessel parameters Jma, and Jds which
are the Bessel solution required for the calculation of
the parameter Na (the dimensionless norm of the mode A.

```

```

Jma:=BesselJ(ma,(a0*ko));Jds:=diff(BesselJ(s, u),
u);u:=s*beta_perp;Jds;
mu:=ko*a0;
ma:=2;
Na:=(Jma^2)*((mu^2)-(ma^2));

```

```

Jma := BesselJ(ma, 3.054000000 )

```



$$Jds := \text{BesselJ}(1, u) - \frac{2 \text{BesselJ}(2, u)}{u}$$

$u := 0.9740828320$

$0.2066875889$

$m := 3.054000000$

$ma := 2$

$Na := 1.260779594$

> Here we define rho, which is the cyclotron resonance mismatch for the system. That is a parameter determined by the electron beam parameters and is calculated here also.

$\text{rho} := (\text{beta\_perp}/\text{beta\_para}) * \text{BesselJ}((ma-s), 0) * Jds;$

$r := 0.2480251067$

>  $I_{hat} := (\text{current}) / (17000);$

$$I_{hat} := \frac{1}{1700}$$

>

> Here, the Pierce parameter is calculated. Also, we find the value for delta H which is the magnetic field mismatch.

$\text{Pierceparameter} := ((4 * I_{hat} * \text{rho}^2) / (\text{gamma}_i * Na * \text{beta\_para}))^{1/3}; \text{evalf}(\text{Pierceparameter});$

$\#\text{Pierceparameter} := 0.11;$

$\text{Pierceparameter} := 0.03795746605 \cdot 4^{(1/3)}$

$0.06025372154$

>  $\text{delh} := (s * \text{omega\_ce} - ko * c) / (ko * c);$

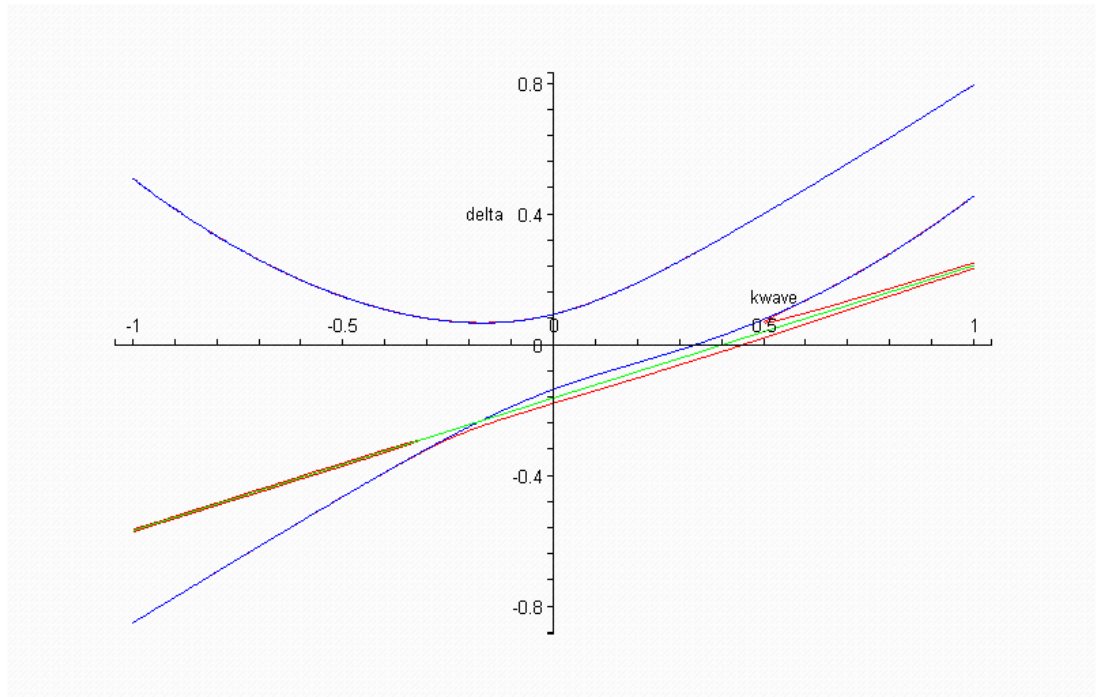
$\text{delh} := -0.1628446875$

>

> Here we plot the real solutions for Equation 16 (fifth order dispersion equation for the gyro-TWT)

$\text{with}(\text{plots}): \text{implicitplot}([(k\text{wave}^2 - 2 * \text{delta}) * (k\text{wave} + \text{delgnorm} - \text{delta}/h0\text{norm}) - 2 * \text{sigmanorm}^2/h0\text{norm}) * (k\text{wave} - (\text{delta} - \text{delh})/\text{beta\_para})^2 = (\text{Pierceparameter})^3 * (k\text{wave} + \text{delgnorm} - \text{delta}/h0\text{norm}) * (1 + ((2 * s * \text{beta\_para})/\text{beta\_perp}^2) * (k\text{wave} - (\text{delta} - \text{delh})/\text{beta\_para}))], \text{disp} = 2 * (\text{sigmanorm}^2)/h0\text{norm}, \text{delta} = (s * \text{om}$

```
ega_ce/(c*ko))+beta_para*kwave-1], kwave=-1..1, delta=-
1..1, color=[red,blue,green],numpoints=200000);
```



```
> delta:=-0.5;
fopen("c:/hgreal",WRITE,TEXT);
fopen("c:/hgimag",WRITE,TEXT);
for counter1 from 1 by 1 to 101 do
solset:=solve(((kwave^2-2*delta)*(kwave+delgnorm-
delta/h0norm)-2*sigmanorm^2/h0norm)*(kwave-(delta-
delh)/beta_para)^2=(Pierceparameter^3)*(kwave+delgnorm-
delta/h0norm)*(1+((2*s*beta_para)/beta_perp^2)*(kwave-
(delta-delh)/beta_para)),kwave);
k1:=Re(solset[1]);
l1:=Re(solset[2]);m1:=Re(solset[3]);n1:=Re(solset[4]);o1:
=Re(solset[5]);
k1;l1;m1;n1;o1;
k2;l2;m2;n2;o2;
k2:=Im(solset[1]);
l2:=Im(solset[2]);m2:=Im(solset[3]);n2:=Im(solset[4]);o2:
=Im(solset[5]);
fprintf("c:/hgreal","%e\t%e\t%e\t%e\t%e\t%e\t\n",delta,k
1,l1,m1,n1,o1);
fprintf("c:/hgimag","%e\t%e\t%e\t%e\t%e\t%e\t\n",delta,k
2,l2,m2,n2,o2);
delta:=delta+0.01;
od;
fclose("c:/hgreal");
fclose("c:/hgimag");
```

## References

1. "The Electron Cyclotron Maser – An Historical Survey", J. L. Hirshfield and V. L. Granatstein, IEEE Transactions on Microwave Theory and Techniques, Vol. MTT-25, No. 6, pp522-527, June 1977.
2. "The Gyrotron", V. A. Flyagin, A. V. Gaponov, M. I. Petelin, and V. K. Yulpatov, IEEE Transactions on Microwave Theory and Techniques, Vol. MTT-25, No. 6, pp514-521, June 1977.
3. "The induced radiation of excited classical oscillators and its use in highfrequency electronics", A. V. Gaponov, M. I. Petelin, and V. K. Yulpatov, Radiophys. *Quantum Electron*, vol. 10, no. 9–10, pp. 794–813, 1967.
4. "Radiation transfer and the possibility of negative absorption in radio astronomy", R. Q. Twiss, *Aust. J. Phys.*, vol. 11, pp 564-579, Dec. 1958; "Electromagnetic radiation from electrons rotating in an ionized medium under the action of a uniform magnetic field", R. Q. Twiss and J. A. Roberts, *Aust. J. Phys.*, vol. 11, pp. 424-446, Sept. 1958.
5. "Electron Beam Interaction with Fast-Waves", R. H. Pantell, Proc. Symp. on Millimetre Waves, Polytechnic Inst. of Brooklyn, N.Y., Vol. 9, pp301-312, April 1959.
6. "Stimulated emission of radiation by relativistic electrons in a magnetic field", J. Schneider, *Phys. Rev. Letters*, vol. 2, pp. 504-505, June 15, 1959.
7. "High Power Microwave Sources", Edited by Victor L. Granatstein and Igor Alexeff, Published by Artech House, 1987, ISBN 0-89006-241-2.
8. "Backward Wave Oscillations in an Unloaded Waveguide", Proc. IRE., Vol. 47, p.1146, 1959.

9. "The Cyclotron Resonance Backward-Wave Oscillator", K. K. Chow and R. H. Pantell, Proceedings of the IRE, Nov. 1960.
10. "Tunable Source of Millimetre and Submillimetre Electromagnetic radiation", I. B. Bott, Proceedings of the IEEE, March 1964.
11. "A Powerful Source of Millimetre Wavelength Electromagnetic Radiation", I. B. Bott, Physics Letters, 15 February 1965.
12. J. Feinstein, "Research on Electronic Interaction with the Fields of Mirror Resonators," *Proc. Int. Cong. Microwave Tubes 5<sup>th</sup>*.
13. "Electron Cyclotron Maser", J. L. Hirshfield and J. M. Watchel, Physical Review Letters, Vol. 12, No. 19, 11 May 1964.
14. N. I. Zaytsev, T. B. Pankratova, M. I. Petelin, and V. A. Flyagin, "Millimeter and submillimeter waveband gyrotrons," *Radiotekhnika I Electronica*, vol. 19, no. 5, pp. 1056–1060, 1974.
15. "The gyrotron: High-power source of millimeter and submillimeter waves," A. A. Andronov, V. A. Flyagin, A. V. Gaponov, A. L. Gol'denberg, M. I. Petelin, V. G. Usov, and V. K. Yulpatov, *Infrared Phys.*, vol. 18, no. 6, pp. 385–393, 1978.
16. "Large-signal characteristics of a wide-band dielectric-loaded gyro-TWT amplifier", K.C. Leou, D. B. McDermott, and N. C. Luhmann, IEEE Trans. Plasma Sci., Vol. 24, no. 3, pp. 718-726, 1996.
17. "Gyro-travelling wave tubes", K. R. Chu, Dig. 22nd Int. Conf. Infrared Millimeter Waves, p 41, July 1997.

18. "Linear Theory of a Wide-Band Gyro-TWT Amplifier Using Spiral Waveguide", Simon J. Cooke and Gregory G. Denisov, *IEEE Trans. Plasma Sci*, Vol. 26, No. 3, June 1998.
19. "Gyro-TWA with a Helical Operating Waveguide: New Possibilities to Enhance Efficiency and Frequency Bandwidth", Gregory G. Denisov, Vladimir L. Bratman, Alan D. R. Phelps, and Sergei V. Samsonov, *IEEE Trans. Plasma Science*, Vol. 26, No. 3, pp 508 , June 1998.
20. "Gyrotron Travelling Wave Amplifier with a Helical Interaction Waveguide", G. G. Denisov, V. L. Bratman, A. W. Cross, W. He, A. D. R. Phelps, K. Ronald, S.V. Samsonov, and C. G. Whyte, *Phys. Rev. Lett.*, Vol. 81, No. 25, December, 1998.
21. "High-Gain Wide-Band Gyrotron Travelling Wave Amplifier with a Helically Corrugated Waveguide", V. L. Bratman, A. W. Cross, W. He, A. D. R. Phelps, K. Ronald, S.V. Samsonov, C. G. Whyte, and A. R. Young, *Phys. Rev. Lett.*, Vol. 84, No. 12, 20 March 2000.
22. "Nonadiabatic Particle Motion in Axiallysymmetric Fields", G. Schmidt, *The Physics of Fluids*, Vol. 5, No. 8, August 1962.
23. "Experimental Trajectory Analysis of Charged Particles in a Cusped Geometry", J. Sinnis and G. Schmidt, *The Physics of Fluids*, Vol. 6, No. 6, June 1963.
24. "Passage of an Intense Relativistic Electron Beam Through a Cusped Magnetic Field", Moshe Friedman, *Physical Review Letters*, Vol. 21, No. 20, May 1970.
25. "Relativistic Electron Dynamics in a Cusped Magnetic Field", M. J. Rhee and W. W. Destler, *The Physics of Fluids*, Vol. 17, No. 8, August 1974.

26. "Study on Velocity Spread for Axis Encircling Electron Beams Generated by Single Magnetic Cusp", S. G. Jeon, C. W. Baik, D. H. Kim, G. S. Park, N. Sato, and K. Yokoo, *Applied Physics Letters*, Vol. 80, No. 20, May 2002.
27. "Design of Low Velocity-Spread Cusp Guns for Axis Encircling Beams", W. Lawson, *Applied Physics Letters* 50 (21), pp 1477-1479, May 1987.
28. "Dispersion of Helically Corrugated Waveguides: Analytical, numerical, and experimental study", G. Burt, S. V. Samsonov, K. Ronald, G. G. Denisov, A. R. Young, V. L. Bratman, A. D. R. Phelps, A. W. Cross, I. V. Konoplev, W. He, J. Thomson, and C.G. Whyte, *Physical Review*, Vol. 70, 2004.
29. "Experimental and Theoretical Study of a Helical Waveguide Structure", V. L. Bratman, G. Burt, A. W. Cross, G. G. Denisov, A. D. R. Phelps, K. Ronald, S. V. Samsonov, awaiting publication.
30. "Characteristics and Applications of Fast-Wave Gyrodevices", Kevin L. Felch, Bruce G. Danly, Howard R. Jory, Kenneth E. Kreischer, Wes Lawson, Baruch Levush and Richard J. Temkin, *Proceedings of the IEEE*, Vol. 87, No.5, pp 752-781, May 1999.
31. "The Linear and Self-Consistent Nonlinear Theory of the Electron Cyclotron Maser Instability", P. Sprangle and A. T. Drobot, *IEEE Trans. Microwave Theory Tech.*, Vol. MTT-25, No. 6, June 1977.
32. "Recent test results on broad-band gyro-TWT and gyro-BWO with helically grooved operating waveguides", G.G. Denisov, V.L. Bratman, M. Yu.

- Glyavin, V.K. Lygin, A.G. Luchinin, V.N. Manuilov, M.M. Ofitserov, M. Thumm and A.B. Volkov, IEEE IVEC 2003, Seoul, Korea, Proceedings, pp338-339.
33. "Gyrotron Oscillators, Their Principles and Practice", Edited by C. J. Edgecombe, Pub. Taylor and Francis Ltd, 1993, ISBN 0-7484-0019-2.
  34. "An experimental study of a gyrotron, operating at the second harmonic of the cyclotron frequency, with optimized distribution of the high frequency field," D. V. Kisel, G. S. Korablev, V. G. Navel'yev, M. I. Petelin, and S. Y. Tsimring, *Radio Eng. Electron. Phys.*, vol. 19, no. 4, pp. 95–100, 1974.
  35. "Multimegawatt Relativistic Harmonic Gyrotron Traveling-Wave Tube Amplifier Experiments", W.L. Menninger, B.G. Danly and R.J. Temkin, *IEEE Trans. Plasma Sci.*, Vol 24. No. 3, June 1996.
  36. "Gyro-TWT Operating Characteristics", P. E. Ferguson, G. Valier, and R. S. Symons, *IEEE Trans. Microwave Theory and Techniques*, Vol. MTT-29, No. 8, August 1981.
  37. "Operation of a Stable 200-kW Second-Harmonic Gyro-TWT Amplifier", Q.S. Wang, D. B. McDermott and N. C. Luhmann, Jr., *IEEE Trans. Plasma Sci.*, Vol 24, No. 3, June 1996.
  38. "Principles of Travelling Wave Tubes", A.S. Gilmour, Jr., Artech House, 1994.
  39. "Theory of Gyrotron Traveling-Wave Amplifiers", Q.F. Li, S. Y. Park and J. L. Hirshfield, *IEEE Trans. Microwave Theory and Techniques*, Vol. MTT-34, No. 10, October 1986.



40. "Characteristics and Optimum Operating Parameters of a Gyrotron Travelling Wave Amplifier", K.R. Chu, A. T. Drobot, V. L. Granatstein and J. L. Seftor, *IEEE Trans. Microwave Theory and Techniques*, Vol. MTT-27, No. 2, February 1979.
41. "Microwave Tubes", A.S. Gilmour Jr., Published by Artech House Inc., 1986.
42. "Theory of Travelling-Wave Amplifiers", Q. F. Li, S. Y. Park and J. L. Hirshfield, *IEEE Trans. Microwave Theory Tech.*, Vol. MTT-34, No. 10, October 1986.
43. "New Microwave System for Gyro-TWA", G. G. Denisov and S.J. Cooke, *Digest 21<sup>st</sup> Int. Conf. Infrared Millimetre Waves* Berlin, Germany, p.AT2, 1996.
44. "The Helically Wrapped Circular Waveguide", K. J. Bunch and R. W. Grow, *IEEE Trans. Electron Devices*, Vol. ED-34, No. 8, 1987.
45. "Study of the Ridge-Loaded Helical-Groove Slow-Wave Structure", W. Wang, Guofen Yu, and Y. Wei, *IEEE Trans. Microwave Theory and Techniques*, Vol. 45, No. 10, October 1997.
46. "An Approach to the Analysis of Arbitrarily Shaped Helical Groove Waveguides", Y. Wei, W. Wang, and J. Sun, *IEEE Trans. Microwave Theory and Guided Wave Letters*, Vol. 10, No. 1, January 2000.
47. "Electromagnetic Fields and Waves, 3<sup>rd</sup> Edition", Paul Lorrain, Dale P. Corson, Francois Lorrain, Published by W. H. Freeman and Company, 1988. ISBN 0-716-71823-5.
48. "Electromagnetic Waves", E.R. Dobbs, 1985.

49. "Microwave Tubes", A.S. Gilmour Jr., Published by Artech House Inc., 1986.
50. "Transmission and Propagation of Electromagnetic Waves (Second Edition)", K.F. Sander and G.A.L. Reed, Published by Cambridge University Press, 1986.
51. "Experimental Demonstration of High-Efficiency Cyclotron-Autoresonance-Maser Operation", V. L. Bratman, G. G. Denisov, B. D. Kol'chugin, S. V. Samsonov, and A. B. Volkov, *Phys. Rev. Lett.*, Vol. 75, pp 3102, 1995.
52. "Experimental Operation of a Cyclotron Autoresonance Maser Oscillator at the Second Harmonic", S. J. Cooke, A. W. Cross, W. He, and A. D. R. Phelps, *Phys. Rev. Lett.*, Vol. 77, pp 4836, 1996.
53. "User-configurable MAGIC for electromagnetic PIC calculations", Bruce Goplen, Larry Ludeking, David Smithe, Gary Warren, *Computer Physics Communications*, Vol. 87, pp 54-86, 1995.
54. "Introduction to MAGIC", T. Gray, D. N. Smithe, Larry D. Ludeking.
55. "Traveling-Wave Tubes", J.R. Pierce and L. M. Field, *Proc. I.R.E.*, February 1947.